

Scanning tunneling microscopy/scanning tunneling spectroscopy on growth, atomic and electronic structure of Co oxide and Mn oxide films on Ag(001)



Dissertation

zur Erlangung des akademischen Grades
doktor rerum naturalium (Dr. rer. nat.)

vorgelegt der

Mathematisch-Naturwissenschaftlich-Technischen Fakultät
(mathematisch-naturwissenschaftlicher Bereich)
der Martin-Luther-Universität Halle-Wittenberg

von Master of Science

Roman Shantyr

geb. am: 07.02.1978 in: Sumy, Ukraine

Gutachterin bzw. Gutachter:

1. Prof. Dr. Henning Neddermeyer
2. Prof. Dr. Horst Niehus
3. PD Dr. Wolfgang Kuch

Halle (Saale), (29.06.2004)

urn:nbn:de:gbv:3-000007013

[<http://nbn-resolving.de/urn/resolver.pl?urn=nbn%3Ade%3Agbv%3A3-000007013>]

Content

1	Introduction	5
2	Properties of Co oxides and Mn oxides	9
2.1	Geometric structure	9
2.1.1	Co oxides	9
2.1.2	Mn oxides	11
2.2	Electronic structure	12
2.2.1	Co oxides	12
2.2.2	Mn oxides	17
3	Fundamentals of STM and STS	19
3.1	Scanning tunneling microscopy (STM)	19
3.2	The tunneling effect	20
3.3	Scanning tunneling spectroscopy (STS)	22
3.3.1	$I(U)$ spectroscopy	22
3.3.2	$I(z)$ spectroscopy	24
3.3.3	$z(U)$ spectroscopy	25
4	Experimental	27
4.1	Low temperature (LT) STM	27
4.2	Sample preparation	28
4.3	Tip preparation	29
4.4	STM control and data evaluation	30
5	Characterization of the Ag(001) substrate	33
5.1	Clean Ag(001)	33
5.1.1	STM /LEED characterization	33
5.1.2	STS characterization	34
5.2	O ₂ and Ag(001)	44
5.2.1	Adsorption at 77 K	47
5.2.2	Annealing in O ₂	48
6	Growth of Co oxides on Ag(001)	51
6.1	A type precursor	51
6.2	B type precursor and transition to CoO(001)	53
6.3	(111) oriented Co oxide	55
6.4	Bias voltage dependent contrast	59
6.5	Scanning tunneling spectroscopy	63
6.5.1	$I(U)$ spectroscopy	63
6.5.2	$I(z)$ spectroscopy of CoO(001), (111) Co oxide and Ag(001)	72

6.5.3	$I(U)$ spectroscopy of A and B precursors	74
6.6	Interaction of CoO(001) with O ₂	76
6.7	Co clusters on CoO(001)	77
7	Growth of Mn and Mn oxides on Ag(001)	81
7.1	Initial stages of Mn film growth on Ag(001)	81
7.2	Initial stages of Mn oxide film growth on Ag(001)	84
7.2.1	O ₂ pressure of 10 ⁻⁷ mbar	84
7.2.2	O ₂ pressure of 10 ⁻⁶ mbar	86
7.2.3	Comparison of $I(U)$ and $z(U)$ STS data	88
8	Summary and outlook	91
	Literature	97

Transition metal oxides (TMO) are known for their extraordinary chemical and physical properties. The specific features are due to the progressive filling of the *d* orbital shell in the transition metal series. The optical, magnetic and electronic properties of TMOs are of particular interest. A large number of industrial applications are known which are accompanied by a multitude of scientific problems and have stimulated many interesting investigations. An introduction and an overview on recent studies of TMO surfaces is found in [1].

An important example of an industrial application is the use of TMOs in heterogeneous catalysis, where the surface properties of TMOs are particularly important. Therefore, molecular chemisorption and reactions at the oxide surface (such as NiO and CoO) has been the subject of numerous studies [2]. The catalytic action of the TMO surface is usually based on oxidation or reduction of the involved chemical components (usually gases) occurring at the oxide surface. A reactant can be oxidized by O₂ at the oxide surface allowing desorption afterwards. The surface is reduced in this way. Different physical and technical problems have to be considered for optimising these reactions. For example, to maintain the oxidation state of the surface, a continuous O₂ supply is necessary. Adsorbed O₂ species also play a crucial role in the chemisorption of other molecules. As it was shown by McKay et al. [3], molecular H₂O reacts with NiO surfaces only in the presence of chemisorbed O. For a deeper understanding of this phenomenon, the interaction of O₂ with the surfaces of rocksalt-like TMO as MnO [4], CoO [5] and NiO [3] was studied. It was shown that the O₂ chemisorption behaviour on NiO(001) and CoO(001) single crystals is quite similar. Cappus et al. [6] have investigated different catalytic systems by means of electron spectroscopic methods. In particular, the adsorption and reaction of H₂O and NO on clean and OH⁻ precovered NiO and CoO surfaces were investigated. The adsorption of CO and H₂O on a nearly perfect CoO(001) surface and on a CoO(001) surface containing defects has also been studied [7]. Schwarz et al. [8] have reported on oxygenation reactions of hydrocarbons (CH₄, C₂H₄, and C₆H₆) at the surfaces of transition metal monoxides (MnO, FeO, CoO, and NiO).

Sometimes, the oxides are supported by other oxides and the catalytic activity results from the interaction between the oxides. Helfensteyn et al. [9] have investigated the commercial oxide catalysts CoO-MoO₃(Al₂O₃) and NiO-MoO₃(Al₂O₃). They are used for the hydrotreatment of hydrocarbons as an initial step for the feed in cracking and reforming. The aim of this pretreatment is to lower the S content and the amount of aromates in the feed (gas oil, kerosene etc.).

The TMOs are used in catalysts also as a supporting material for metal clusters which actually induce the catalytic reaction. The metal clusters are not only interesting for industrial applications. Experiments and calculations have shown that metallic clusters on insulating surfaces possess many interesting features which are quite different from bulk, liquids or gaseous materials. Metal clusters are

nanostructures and display interesting quantum effects [12], [13]. Some fundamentals of cluster physics and adsorbate-interface interactions at clusters can be found in [15].

An other interesting application of TMOs is their use in magnetoelectronic systems. Especially, TMO films are needed for the realisation of a magnetic random access memory (MRAM). MRAM elements usually consist of two magnetic layers with different coercivity which are separated by an insulating spacer layer. The resistivity normal to the layers strongly depends on the spin orientation of the two magnetic layers. This effect is called tunneling magnetoresistance (TMR) [17], [18]. The advantages of MRAM elements over common semiconductor-based dynamic access memories (DRAMs) are low energy consumption and high storage density. Furthermore, MRAM elements are non-volatile storage devices, i.e., they keep the information when the computer is switched off [14]. The structural and electronic properties of the tunneling barriers (TMO films) used in such devices should be well defined.

Doudin et al. [17] have investigated the magnetoresistance of Ni/NiO/Co junctions. Besides Al_2O_3 [18], also CoO and NiO [19] can be used as a tunneling barrier in MRAM elements. The highest TMR ratio measured up to now was obtained by using electrodes of manganite $\text{La}_{2/3}\text{Sr}_{1/3}\text{MnO}_3$ [20], [21].

Due to the broad use of TMO films in the above mentioned applications, the knowledge of growth as well as the structural and electronic properties is of crucial importance. Specifically, oxide films prepared on metals are of great interest. In case of insulating oxide films, one can avoid charging effects and analytical tools using charged particles can be applied. Additionally, the investigation of surface properties becomes much easier if thin films (in the monolayer (ML) range) are prepared. For thin epitaxial NiO films on Ag(001), Müller et al. [23] have varied the film thickness in order to separate bulk and surface states. Of course, there exist valuable studies of surfaces of bulk crystals, too. Castell et al. [24], e.g., were able to perform scanning tunneling microscopy (STM) studies of (001) cleavage faces of CoO and NiO single crystals. In comparison to NiO, a cleavage of CoO was more difficult. This was evident from the cleavage structure of the surface, observed in STM. Most surface orientations, however, are difficult to prepare by using bulk crystals. In the case of MnO, e.g., the cleavage of a single crystal along the (001) plane does not lead to a smooth (001) surface, but to a surface which is covered by small pyramids with (111) facets [1]. Thin film epitaxy, therefore, can help to avoid such problems.

In the present work, Co oxide and Mn oxide films were prepared and their structural and electronic properties were analysed by means of STM and scanning tunneling spectroscopy (STS). In addition, growth and electronic properties of Co clusters on oxide surfaces were studied. The investigations are a continuation of previous studies performed by Sebastian [22] where nucleation and growth of CoO layers on Ag(001) and on Au(111) substrates were studied by STM.

The preparation of thin TMO films of high structural order turns back to the work of Marre and Neddermeyer [25]. They prepared NiO(001) and NiO(111) films on Ag(001) and on Au(111) substrates, respectively. In these experiments, it has been demonstrated that oxide films of high structural order can be obtained

by reactive deposition of a metal in an O₂ atmosphere. The quality of such films is much better than that of oxide films obtained by post oxidation of a deposited metal layer.

In the present study, an Ag(001) substrate was chosen to prepare the oxide films. The selection of an Ag(001) substrate was motivated by the observation that well ordered CoO films can be grown on the surface [26]. One reason of the high degree of film perfection is the relatively small lattice mismatch between bulk CoO and the substrate (around 4%). The oxide films were prepared by reactive deposition of Co (later also Mn) in an O₂ atmosphere (typically 10⁻⁶ mbar) onto Ag(001) similar as described in [26].

As has been shown in recent experiments, more stable analysing condition can be achieved at low temperatures (LT) around 80-100 K [27]. Therefore, STM and STS studies were mainly performed in the LT regime (100K) in a special LT STM equipment. Due to the cooling, atomic resolution was achieved for all oxide species observed and the stability of tunneling conditions was strongly increased. At room temperature (RT), i.e., in conventional STM imaging, it was quite difficult to achieve such defined conditions. Consequently, also STS could not be applied in previous investigations. At RT, the voltage ramps necessary in STS led to drastic tip changes making a continuous measurement impossible. This problem did not appear in the present investigations making STS studies of all oxide structures possible. This also allowed a deeper understanding of the imaging process and the contrast behaviour of oxide islands on a metal surface, which has been described before only qualitatively [31].

In the first part of the investigation, the Ag(001) substrate was characterized by STM. The influence of the used tip/sample combinations for STS was also investigated. While studying the electronic structure of Ag(001), the formation of electron standing waves in front of the surface was observed when the STM was used in the field emission regime. The so called field emission resonances (FER) or Gundlach oscillations [63] were studied in detail for the metallic Ag(001) surface and later for different oxide surfaces. Moreover, the interaction of O₂ with Ag(001) was studied as it plays a crucial role in the reactive oxide film formation.

In the next step, the growth of Co oxide on Ag(001) was investigated. These studies were mainly addressed to the initial stage of growth. A fascinating variety of different Co oxide islands (including precursor state islands) has been observed [28]. However, the different island types and their occurrence have not been elucidated completely up to now. During the growth experiments presented here, additional island types were discovered [29]. The electronic properties of all island types were characterized. In addition, the interaction of oxide island with O₂ from the gas phase was studied. Finally, the growth of Co clusters on CoO(001) surfaces was investigated.

Based on the knowledge of the formation of Co oxide films, first attempts have been made to prepare defined Mn oxide films on Ag(001). In the first step, the growth of metallic Mn on Ag(001) was studied. The formation of a Mn/Ag alloy surface layer at RT was observed and characterised by means of STM/STS and low energy electron diffraction (LEED). In the next step, Mn was deposited in an O₂ atmosphere onto Ag(001). Depending on the preparation conditions (such as

substrate temperature and residual O₂ pressure), a variety of Mn oxides was observed with STM. In addition, several successful attempts were made to characterize different Mn oxide islands by means of STS.

This work is organised as follow. After an introduction into the properties of Co oxides and Mn oxides (Chapter 2) the basics of STM/STS are presented (Chapter 3). In the experimental part, the most important components of the UHV equipment are described as well as the preparation of STM tips and oxide layers (Chapter 4.1- 4.3). Some details on the STM control system and data evaluation are also given (Chapter 4.4). Chapter 5 deals with the clean Ag(001) substrate (Chapter 5.1) and its interaction with O₂ (Chapter 5.2). In Chapter 6, results on growth, atomic, and electronic structures of different Co oxide islands on Ag(001) are presented. Additionally, the interaction of CoO(001) surfaces with O₂ from the gas phase is described (Chapter 6.6) as well as the deposition of Co clusters on CoO(001) (Chapter 6.7). Chapter 7 contains results on defined MnO films. Information on growth, atomic, and electronic structure of Mn and Mn oxide islands on Ag(001) are given. Finally, a summary and an outlook are presented in Chapter 8.

2

Properties of Co oxides and Mn oxides

2.1

Geometric structure

2.1.1 Co oxides

From the literature [32], it is known that Co oxide have at least two stable phases, i.e., CoO rocksalt (NaCl)-like structure and Co_3O_4 spinel-like structure.

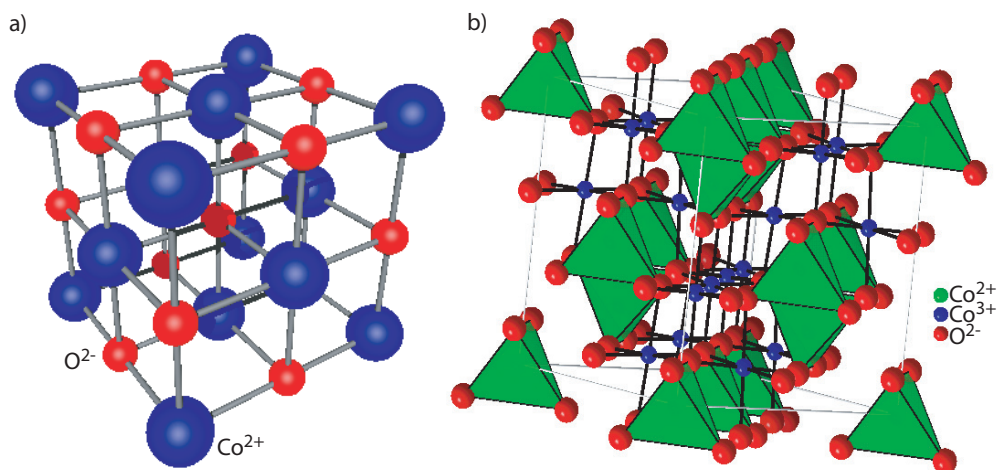
The CoO NaCl-like structure consists of two fcc sublattices of Co^{2+} and O^{2-} ions. Both lattices are displaced against each other along the volume diagonal of the cubic unit cell. Each Co^{2+} ion is located in an octahedral position surrounded by eight O^{2-} ions and vice versa (see Figure 2.1a). The lattice constant amounts to 0.425 nm [33]. The unit cell consists of four Co- and four O-ions.

The Co_3O_4 spinel-like structure is shown in the model of Figure 2.1b constructed according to [33]. The lattice constant of Co_3O_4 is 0.805 nm. Co^{2+} and Co^{3+} ions are arranged in a ratio of 1:2 which can be also written as $\text{Co}^{2+}\text{Co}_2^{3+}\text{O}_4^{2-}$. The spinel unit cell consist of 8 Co^{2+} -, 16 Co^{3+} - and 32 O^{2-} -ions. The Co^{2+} -ions occupy 1/8 of the available tetrahedral lattice sites whereas the Co^{3+} -ions are found on half of all available octahedral sites [34].

Figure 2.1 Atomic structure of:

a) CoO (rock salt),

b) Co_3O_4 (spinel).



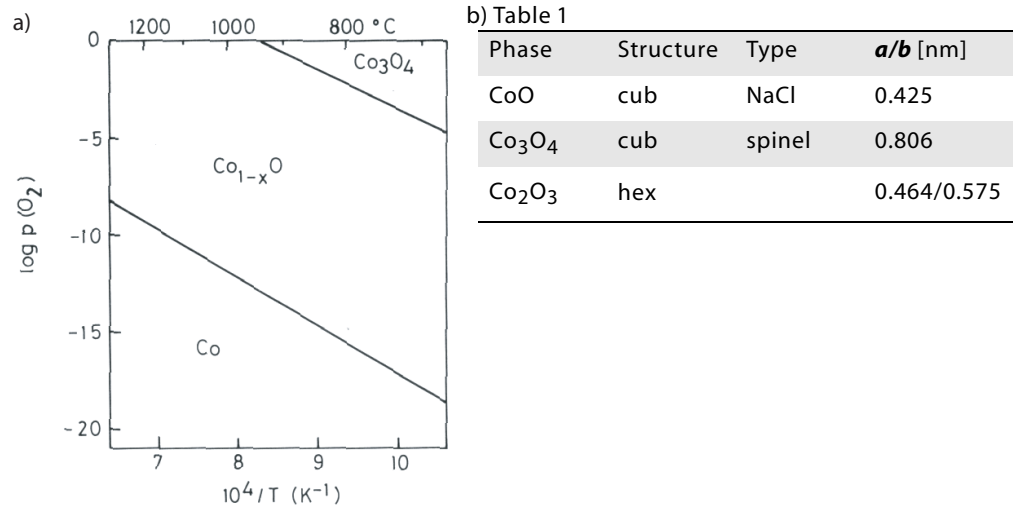
Information on the thermodynamic stability of Co oxides is conventionally displayed in form of phase diagram (Figure 2.2a) where the stability range of Co oxides is presented in dependence of O_2 partial pressure ($p(\text{O}_2)$) and the temperature (T).

The table of Figure 2.2b displays the main structural data of Co oxides. A third oxide phase (Co_2O_3) is listed in the table. It is, however, uncertain whether this compound exists in a form of a stable crystal. Brundle et al. [35] emphasized that they were not able to prepare a Co_2O_3 crystal in their studies.

Figure 2.2

a) Phase diagram of Co/O₂ system according to [1],

b) Table 1. Co-O crystal structure and lattice parameters (**a** and **b**) of Co oxides.

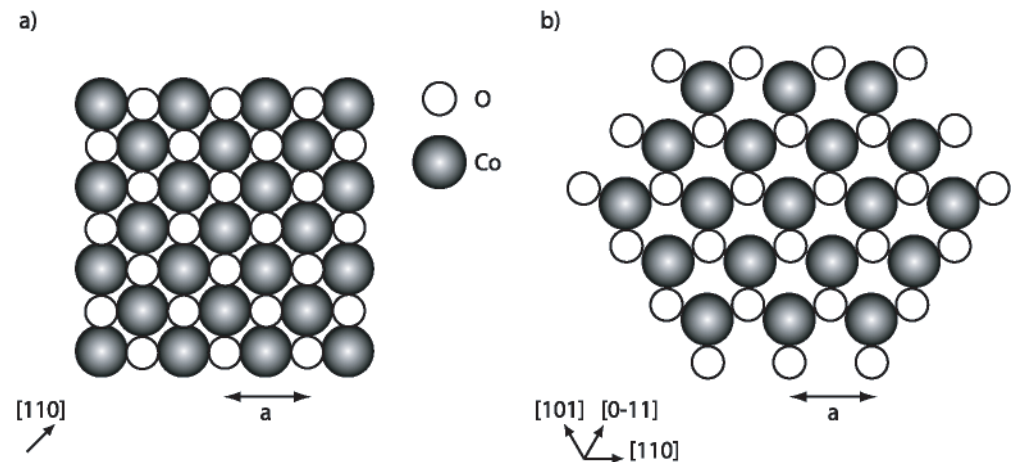


In Figure 2.3, the structure of CoO(001) and CoO(111) surfaces are depicted as derived from the bulk lattice. For the CoO(001) surface, the Co- and O-ions are equally distributed over the surface. This corresponds to a nonpolar surface (see also Figure 2.1a). The CoO(111) surface (Figure 2.3b) consists either of (111) planes of Co- or (111) planes of O-ions. This makes the surface polar since the alternation of positively and negatively charged planes leads to the formation of a dipole moment perpendicular to the surface.

Figure 2.3 Surface structures of CoO:

a) (001) surface,

b) (111) surface.



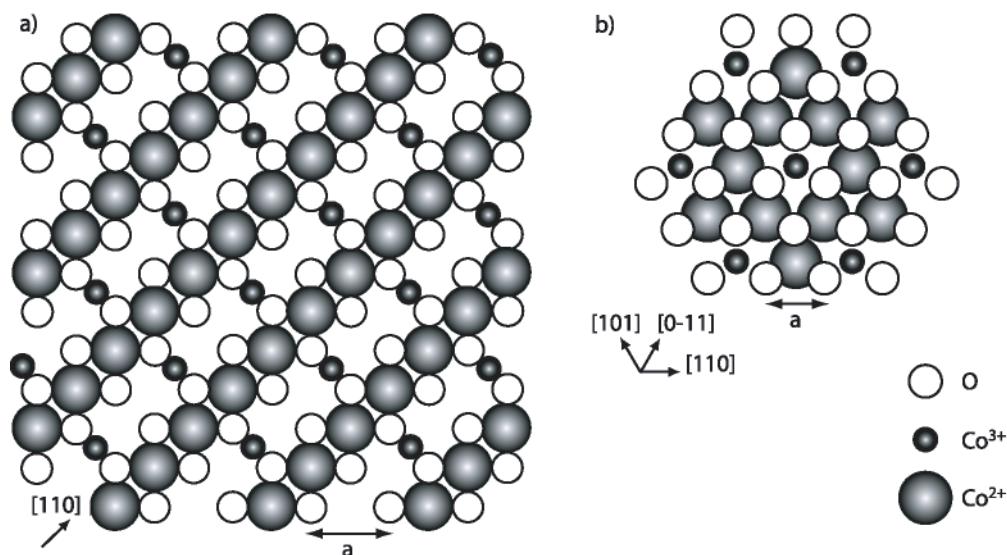
Experimentally, the CoO(001) surface can be obtained by cleaving a CoO crystal under UHV conditions. Surfaces obtained in this way usually display a (1×1) structure with alternating Co- and O-ions as shown in Figure 2.3a [24]. The unit cell consists of one Co- and one O-ion. The next nearest neighbour distance is 0.31 nm. In contrast to CoO(001), the preparation of CoO(111) surfaces as shown in Figure 2.3b is problematic. Because of their polar nature, those surfaces are unstable at least for the bulk sample. It was theoretically shown that the problem of the diverging Coulomb potential of polar surfaces for an infinitely thick crystal is avoided if a p(2×2) surface reconstruction is formed [36] which has been experimentally found, e.g., for NiO(111) [38],[39]. In the case of polished CoO(111), X-ray diffraction experiments revealed that the surface is stabilized by a thin layer having a Co₃O₄ spinel-like structure [37].

In Figure 2.4, models of the surface of the Co_3O_4 spinel-like structure are shown for (001) and (111) orientations. The model of Figure 2.4a indicates that the (001) surface is composed either by O-ions displaying a (1×1) structure or by Co-ions displaying a (1×2) or a (2×2) structure depending on surface termination (Figure 2.4a). In the case of the (111) orientation (see Figure 2.4b), the surface is terminated either by O-ions or by Co^{2+} -ions forming a (1×1) structure or by Co^{3+} ions forming a (2×2) structure.

Figure 2.4 Surfaces of Co_3O_4 spine-like crystals:

a) (001) surfaces,

b) (111) surfaces.



2.1.2 Mn oxides

The situation becomes more complex when the Mn-O system is inspected. In Figure 2.5, the phase diagram of this system is presented. The most important crystallographic data of the intermediate phases are listed in Table 2. From Figure 2.5, it is obvious that at the same temperature many different compounds can be formed depending on O_2 concentration. This makes the deliberate preparation of Mn oxides quite difficult since one has simultaneously to control both the substrate temperature and the O_2 content.

A detailed description of Mn oxide structures is omitted here since in the present work only first experiments were made to prepare a crystalline Mn oxide film.

Figure 2.5 Phase diagram of the Mn/O₂ system [40].

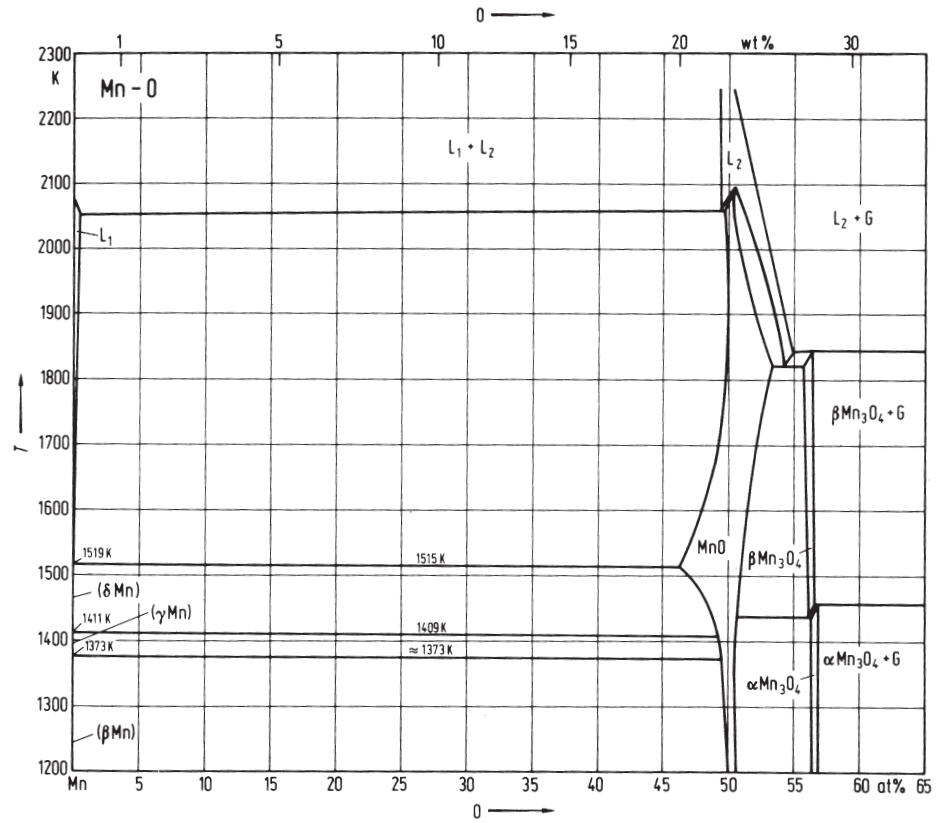


Table 2. Crystal structures and lattice parameters (*a, b, c*) of the Mn-O system [40].

Phase	Structure	Type	<i>a</i> [nm]	<i>b</i> [nm]	<i>c</i> [nm]
MnO	cub	NaCl	0.4443		
Mn ₃ O ₄	cub	spinel	0.868		
Mn ₂ O ₃	cub	Mn ₂ O ₃	0.9414		
MnO ₂	orth	MnO ₂	0.927	0.2866	0.4533

2.2

Electronic structure

2.2.1 Co oxides

The electronic configuration of CoO can be written as $\text{Co}3d^7\text{O}2p^6$. In the ground state, the O 2p band is completely occupied whereas the Co 3d band is only partly occupied. According to the band theory, one expects metallic properties of CoO since the valence band is only partly occupied. A metallic nature of CoO is also predicted by the density functional theory (DFT) which is the most successful tool for describing the electronic properties of solids [41]. However, experiments have revealed that CoO is an insulator with a band gap of 2.5 eV [1],[42]. This discrepancy has been attributed to the strong electron-electron

interaction in the 3d-band which strongly affects the electronic structure of CoO. Therefore, the one electron approach of the band model as well as the DFT approach fails since the electrons strongly interact during its motion.

In contrast, the appearance of the band gap in CoO is well explained by the Mott-Hubbard model [1]. According to this model, the 3d-band is splitted into a lower sub-band (below the Fermi level) which is completely occupied and an upper sub-band (above the Fermi level). The sub-bands are formed due to the strong Coulomb interaction between the electrons of the d-band (known also as the electron correlation energy or the Hubbard energy (U)) as shown in Figure 2.6. Thus, transitions from the valence band into the conduction band should have a d-d character. However, Shen et al. [43] have experimentally shown that this transition has a p-d character. Therefore, the O 2p-band seems to play an important role and has to be taken into account when the structure of the valence band is analysed.

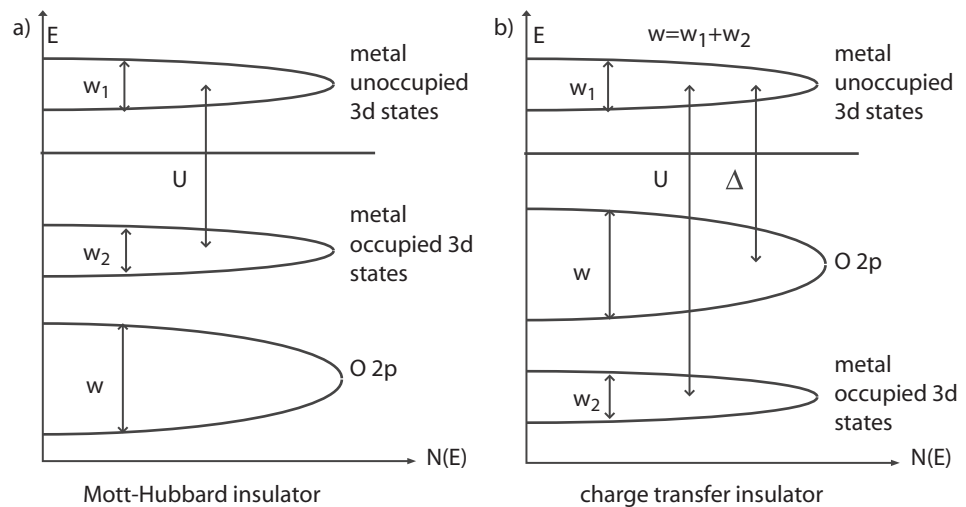
Zaanen et al. [44] have shown that a good explanation of the experimental data can be achieved by a slight modification of the Mott-Hubbard model. Differing from the Mott-Hubbard model where only the interaction between the cations (metal ions) is taken into account, also an interaction between cations and anions was included. For CoO, the Hubbard energy U can be very large and, therefore, the O 2p-band is placed between the Co sub-bands as shown in Figure 2.6a. A complete mathematical description of this charge transfer effect can be found in [1] and [44].

Figure 2.6 Schematic representation of the electronic structure of

a) Mott-Hubbard insulator

b) charge transfer insulator [1].

w assigns the band width, $N(E)$ the density of states



Following the Mott-Hubbard model, one has assumed that any charge fluctuation between two cations A and B $d_A^n d_B^n \rightarrow d_A^{n-1} d_B^{n+1}$ is prevented by the electron correlation energy U , leading to a splitting of the d-levels:

$$E(d^n) + E(d^n) \rightarrow E(d^{n-1}) + E(d^{n+1}) - U \quad (2.1)$$

For CoO, U equals 10 eV [43]. Thus, the lower sub-band lies far below the O 2p-band (Figure 2.6b). As an extension, the second charge fluctuation have to be analysed, i.e., the charge transfer from the anion (ligand) to the cation. During this process, a charge will be transferred from the ligand (L) to the transition metal ion: $d^n L \rightarrow d^{n+1} L^{-1}$ (here, the index -1 for the ligand indicates the charge transfer). To obtain conductivity, the energy of the

charge transfer Δ has to be applied. For CoO, this energy is about 6 eV [43] which is too large to obtain conductivity in the ground state. Therefore, CoO should have insulating properties which is in agreement with experiments. The energy Δ can be defined as

$$E(d^n) + E(L) \rightarrow E(d^{n+1}L^{-1}) - \Delta. \quad (2.2)$$

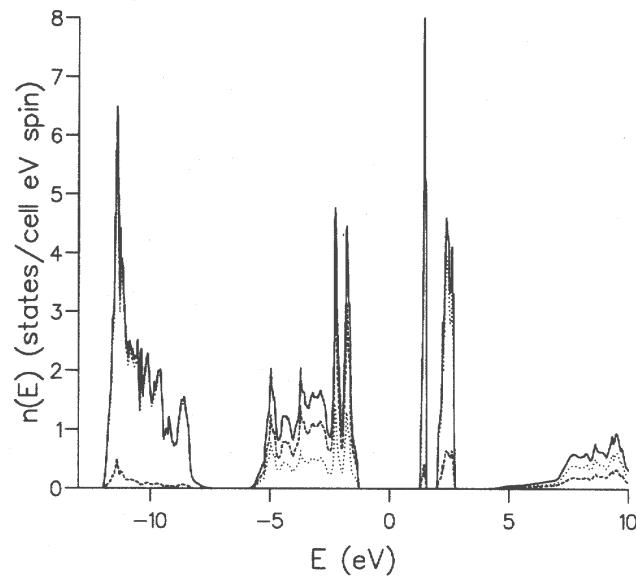
Since Δ is smaller than U , it represents the smallest ionisation energy of the system. Therefore, Δ defines the value of the band gap. Due to this, CoO belongs to charge transfer insulators.

The local-spin-density approximation with self interaction correlation (LSDA-SIC) and LSDA with charge transfer consideration (LSDA+U) are two further successful approaches which allow the description of strongly correlated systems by means of DFT-LSDA [45]. Both approaches lead to a better understanding of the band structure of transition metal oxides.

In the SIC formalism, each unphysical interaction of an electron with itself is explicitly subtracted. This theory is well suited for describing wide-gap insulators where LSDA usually fails. In [46], the LSDA-SIC theory was applied for transition metal oxides like CoO. A result is presented in Figure 2.7 where the calculated density of states (DOS) is shown. The solid curve indicates the total DOS, the dashed line corresponds to the partial DOS of O, and the dotted line represents the partial DOS of Co. The lower Co sub-band occupied with 7 electrons is found at an energy around -10 eV and the unoccupied sub-band at 2 eV. The valence band preferentially consists of an O state which is in line with the experimentally found p-d like transition. The calculated width of the band gap is 2.51 eV which agrees with the experimentally measured value of 2.5 eV [42].

In general, the LSDA-SIC approach explains the splitting of the Co 3d-band and allows to deduce a width of the band gap with is in a good agreement with the experiments. Usually, the valence band has an O 2p character making CoO a charge transfer insulator. However, the problem to calculate the exact position of the lower Co sub-band remains.

Figure 2.7 DOS of CoO calculated according to LSDA-SIC formalism [46].

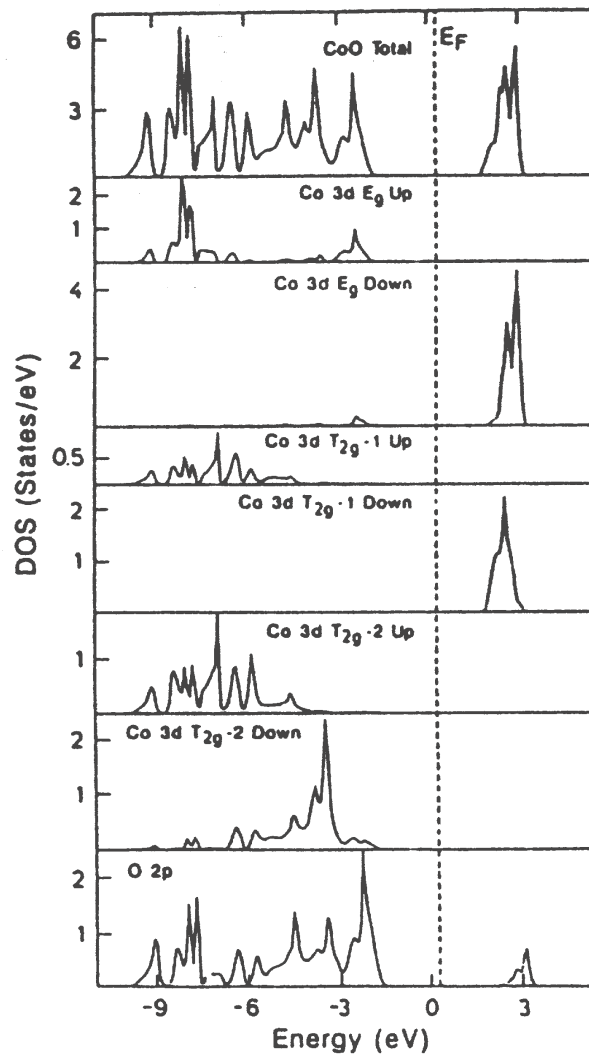


The LSDA+U approach takes into account the mutual interaction of d-electrons. The splitting of the d-band is explained according to the Mott-Hubbard model where occupied d-orbitals and unoccupied d-orbitals are correspondingly shifted by $-U/2$ and $+U/2$. A detailed description of this theory is found in [47]. Figure 2.8 shows the DOS of CoO calculated by means of LSDA+U. The uppermost graph represents the total density of states. It is obvious that the valence band and the conduction band are separated which more precisely describes CoO as an insulator. The valence band mostly consists of O 2p states, thus a p-d type band gap is obtained. The calculated width of the band gap, however, amounts 3.2 eV which is still to large in comparison to the experimental value.

Figure 2.8 DOS of CoO calculated according to the LSDA+U model (upper part).

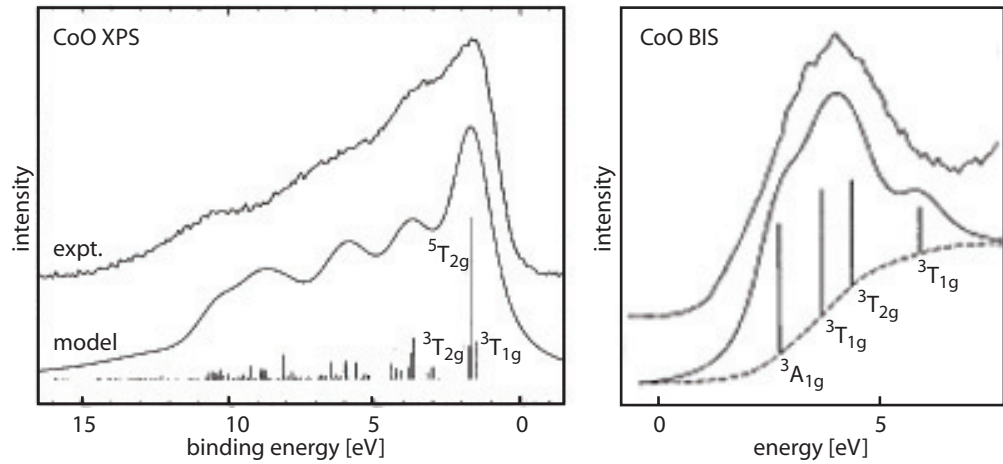
Partial DOS of Co-3d sub-bands (middle part). Up and down indicate spin orientation.

Partial DOS of O-2p states (lower part). Taken from [47].



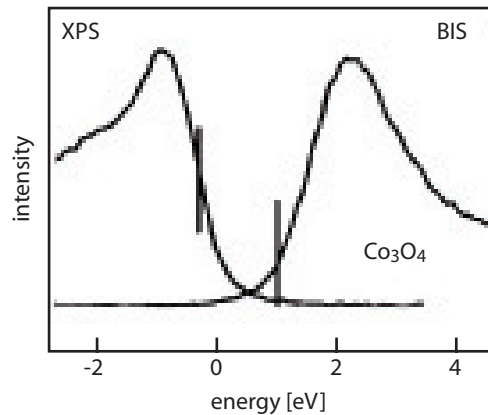
The measurements of the electronic structure of CoO have been performed by means of X-ray photoemission spectroscopy (XPS) and bremsstrahlung isochromat spectroscopy (BIS) [42]. The results are presented in Figure 2.9. The width of the band gap of CoO deduced from this measurements is 2.5 ± 0.3 eV.

Figure 2.9 XPS and BIS experiments on CoO taken from [52].



The same authors have also reported on XPS and BIS investigations of Co_3O_4 . The electronic structure of Co_3O_4 is well understood by assuming that Co^{2+} resides on tetrahedral sites and the low-spin Co^{3+} on octahedral lattice sites. A gap width of 1.6 ± 0.3 eV was deduced [42]. Therefore, Co_3O_4 has been considered as a charge transfer insulator.

Figure 2.10 XPS and BIS of Co_3O_4 taken from [52].

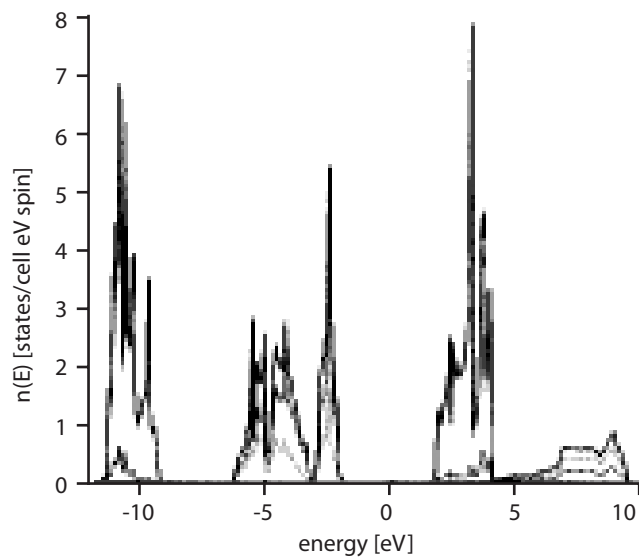


CoO was also characterized by other techniques such as ultraviolet photoemission spectroscopy (UPS) [7], angle-resolved UPS (ARUPS) [48], and electron energy loss spectroscopy (EELS)[49]. The results are in agreement with the already mentioned properties.

2.2.2 Mn oxides

The electronic structure of MnO has been theoretically [46],[50],[51] as well as experimentally [52],[53] investigated. MnO belongs to the charge-transfer insulators with $Mn3d^5O2p^6$ configuration and has a band gap of 3.6 eV [1]. The DOS of MnO calculated according to the LSDA-SIC formalism [42] is represented in Figure 2.11. The solid curve indicates the total DOS, the dashed line corresponds to the partial DOS of O, and the dotted line represents the partial DOS of Mn. A band gap of 3.57 eV was obtained which is in good agreement with the experiment.

Figure 2.11 DOS of MnO calculated according to the LSDA-SIC formalism [46].



3

Fundamentals of STM and STS

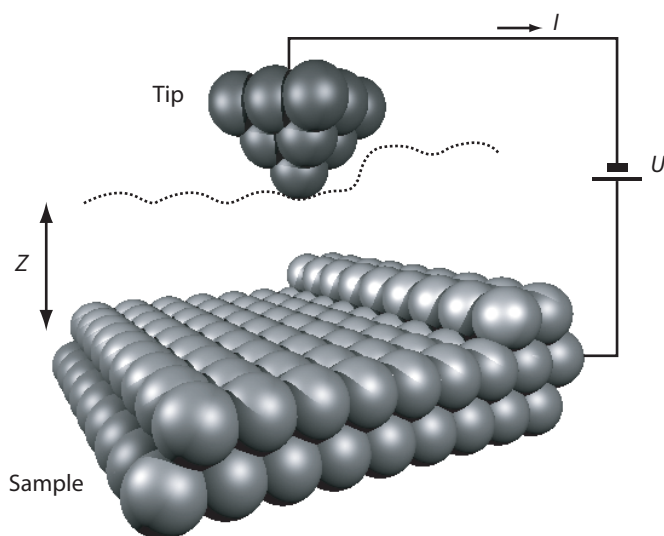
3.1

Scanning tunneling microscopy (STM)

The scanning tunneling microscope was developed by Binnig, Rohrer, Gerber and Weibel [54]. Since STM allows imaging on an atomic scale, it belongs to the most powerful experimental techniques of surface science.

In STM, a small probe (usually an atomically sharp metallic tip) is placed very close to the surface (0.3-2 nm) and a small bias voltage U is applied between the tip and the sample (see Figure 3.1). As result, a current of electrons I flows between the electrodes through the vacuum gap. This process is a quantum mechanical phenomenon and has been called the “tunneling” effect. The tunneling current is usually the main value measured in the STM experiment and the basic of its theoretical description is given in the next chapter. In the imaging process, the tip scans over the surface and a regulation system attempts to keep the current constant by varying the tip/sample distance (z). This mode of imaging is mostly used and is called “constant current topography” mode (CCT). The z -regulation signal is recorded during sample scanning. Usually, it is represented in form of a grey level image. Here, the darker tone corresponds to the scanner stretch and the lighter one to its retraction. Thus, information on the surface is obtained in real space.

Figure 3.1 Main principle of STM.



The tunneling current strongly depends not only on the topography but also on the electronic structure of the surface. Therefore, surfaces with different chemical composition (as for example islands of oxide films on metals) may provide different contrasts in STM. This may complicate the interpretation of the STM images. On the other hand this “chemical” contrast may yield valuable information on the local sample composition. An exact interpretation of the chemical contrast, however, presupposes that additional information on the electronic structure is available.

Information on the electronic structure can be obtained by applying STS. Varying one of the tunneling parameters (U , I or z), information on the tunneling barrier can be extracted from the STS data. The corresponding spectroscopic techniques are described in more detail in Chapter 3.3.

3.2

The tunneling effect

A theory which describes the tunneling process is generally restricted to elastic tunneling processes. This means that tip/sample interactions which create phonons, plasmons and other losses are ignored. Also some simplification are usually made. For example, the wave functions of the tip is reduced to s-state wave functions.

In general, there are two approaches to derive an equation for the tunneling current in STM. One is based on the scattering theory and is able to yield exact solutions for certain tunneling conditions [55]. The main advantage of this approach consists in the acceptance of different tunneling distances and correspondingly different tip/sample interactions. Usually, a modified Bardeen approach [56] is used which is based on perturbation theory.

The first theoretical description of the tunneling process in STM was presented in 1985 by Tersoff and Hamann [57] which has been applied by many authors in numerous publications. In this theory, the wave functions of the tip and the sample are considered as separated, undisturbed systems and described by means of the Schrödinger equation

$$(T + U)\Psi_\mu = E_\mu \Psi_\mu. \quad (3.1)$$

Here, T corresponds to the kinetic energy, U to the potential energy, Ψ_μ to the wave function, and E_μ corresponds to the energy of the state μ . The wave function of the complete system is determined by means of time dependent perturbation theory. For this, the potential of the tip is described as a perturbation $U_T(t)$ and inserted into a time dependent Schrödinger equation which yields

$$i\hbar \frac{\partial \Psi_\mu}{\partial t} = [T + U_S + U_T(t)]\Psi_\mu. \quad (3.2)$$

Here, U_S is the potential of the sample and \hbar the Plank constant.

Using

$$\Psi(x, t) = \Psi(x) \exp\left(\frac{-iEt}{\hbar}\right) \quad (3.3)$$

as an approach for the wave function, the transition probability $w_{\mu\nu}$ of an electron tunneling from the state μ with the wave function ψ_μ into the state ν with the wave function ψ_ν can be written as:

$$w_{\mu\nu} = \frac{2\pi}{\hbar} |M_{\mu\nu}|^2 \delta(E_\nu - E_\mu). \quad (3.4)$$

Here, $M_{\mu\nu}$ corresponds to the matrix element of the transition probability. Bardeen [56] has shown that the matrix element can be represented by a surface integral

$$M_{\mu\nu} = -\frac{\hbar^2}{2m} \int d\vec{S} (\psi_\nu^* \nabla \psi_\mu - \psi_\mu \nabla \psi_\nu^*). \quad (3.5)$$

Here, m is the mass of the electron and dS the surface element. The tunneling current is calculated by summing up over all possible states. Using the density of states ρ of the sample and of the tip, one finally obtains for the tunneling current

$$I = \frac{4\pi e^2}{\hbar} U_b \rho_S(E_F) \rho_T(E_F) |M|^2 \quad (3.6)$$

which is valid for small bias voltages U_b . Here, e is the electron charge and E_F the corresponding Fermi level.

Assuming that only s -like wave functions contribute to the tunneling from a tip of radius R , the DOS of the sample can be written as

$$\rho_S(r, E_F) \sim |\Psi_\mu(r)|^2 \sim e^{-2k(R+dz)}, \quad (3.7)$$

where

$$k = \frac{\sqrt{2m\phi}}{\hbar} \quad (3.8)$$

is the decay coefficient of the wave function into the vacuum and ϕ the height of the energy barrier. Assuming a point-like tip and summing up equations (3.6) and (3.7) finally yields

$$I \sim U_b \rho_S(E_F) e^{\frac{\sqrt{2m\phi}}{\hbar} z}. \quad (3.9)$$

According to (3.9), the tunneling current I near E_F is proportional to the bias voltage U_b and the density of states ρ_S of the sample. More important, however, is the exponential dependence on the distance z between the tip and the sample which is the main reason for the high sensitivity of the STM perpendicular to the surface.

3.3

Scanning tunneling spectroscopy (STS)

STS provides valuable information which is complementary to the information obtained in the conventional STM. STS can be accomplished in different ways. The main idea of all STS experiments is to measure one of the tunneling parameters I or z whereas one of the others (usually U or z) is changed (e.g., $I(U)$, $I(z)$, $z(U)$). The STS implementation can vary depending on the energy range accessed, the amount of spectroscopic detail required, and which degree of spatial resolution is simultaneously needed.

3.3.1 $I(U)$ spectroscopy

Most of the STS investigations are performed under the condition of a constant tip/sample separation, which is accomplished by shortly interrupting the feedback controller. Then, the bias voltage is ramped over the desired interval and the tunneling current $I(U)$ is measured during the voltage ramp. For correlating the tunneling spectra to the local topography (and thus to take full advantage of the high spatial resolution of STM), the $I(U)$ measurement must be performed pixel for pixel during the topography measurement. $I(U)$ STS is the most used technique to measure the surface electronic structure. However, the interpretation of the STS data is complicated by two main facts. First, the DOS of the tip is usually unknown. Second, the voltage dependence of the tunneling probability $T(E, U_b)$ is usually also unknown. The first problem is typically investigated by comparing measurements taken at identical surface locations and by ensuring that all results are reproducible using different tips. Although the electronic structure of the tip is unknown, it is at least constant, for stable STS conditions. Thus, in the tunneling spectra obtained at different locations, the tip electronic structure will only contribute a constant background to the measurement. Consequently, the spatially dependent variations in the electronic structure will not be influenced by the tip states. The second problem, i.e., the unknown $T(E, U_b)$ dependence, is managed in different ways depending on the details of the situation. In some cases, the $T(E, U_b)$ dependence on the tunneling probability can be minimized by a special data representation, i.e., by plotting $(dI/dU)/(I/U)$ vs. U (or equally $d(\ln I)/d(\ln U)$ vs. U). This becomes more obvious if an approximate expression of the tunneling current is used [58].

$$I \propto \int_0^{eU} \rho(E) T(E, eU_b) dE \quad (3.10)$$

Here, $T(E, U_b) = \exp(-2kz)$ is the tunneling probability of the electron (see also equations (3.7) and (3.8)). After differentiation, one obtains

$$\frac{dI}{dU} \propto e \rho(eU_b) T(eU, eU) + e \int_0^{eU} \rho(E) \frac{d}{d(eU)} [T(E, eU)] dE. \quad (3.11)$$

From equation (3.11) one finally finds

$$\frac{(dI)/(dU)}{I/U} = \frac{\rho(eU) + \int_0^{eU} \frac{\rho(E)}{T(eU, eU)} \frac{d}{d(eU)} [T(E, eU)] dE}{\frac{1}{eU} \int_0^{eU} \left(\rho(E) \frac{T(E, eU)}{T(eU, eU)} \right) dE}. \quad (3.12)$$

Since $T(E, eU)$ and $T(eU, eU)$ appear as ratios in this equation, their exponential dependencies on z and U cancel out approximately. The first term in the numerator of equation (3.12) is the surface DOS of the sample. The denominator of the equation can be considered as a “normalization” function of the surface DOS. The second term in the numerator is a “background” term arising from the fact that the tails of the wave-functions are affected by the value of the electric field in the tip/vacuum/sample junction. Thus, a change of the voltage changes also the electric field [58]. The relative magnitude of the various terms depend on the polarity of the voltage. For a positively biased sample ($U > 0$), $T(E, eU) \leq T(eU, eU)$ and the maximum transmission occurs at $E = eU$. In this case, each term in equation (3.12) is of the same order of magnitude, and one obtains a “normalized” measure of DOS together with a slowly varying background. If the sample is negative ($U < 0$), $T(E, eU) \geq T(eU, eU)$ the maximum transmission occurs at $E = 0$. Then, the background term has the same order of magnitude as the denominator. However, they are both larger than the DOS term by a factor of $(T(0, eU))/T(eU, eU)$. The measure of DOS is, therefore, reduced by this factor, which can be quite large for large z and U . The reason for this reduction is simply that the transmission probability is strongly increased for states near the Fermi level of the negatively biased electrode. Thus, it should be difficult to observe low-lying occupied surface states with STS.

A normalization of the differential conductance (dI/dU) to the total conductance (I/U) provides a very conventional measure of the surface DOS for the case of metallic or small-band-gap surfaces [58],[59]. However, for large-band-gap surfaces, the measure of $(dI/dU)/(I/U)$ diverges at the band edges, since the current approaches zero faster than the conductance [58]. Inside the gap, $(dI/dU)/(I/U)$ is undetermined because $I = 0$. In the case of thin insulating films, however, the substrate states exponentially decay through the film, and a finite density of states remains at the insulator surface [60]. Thus, the tunneling current inside the band gap remains finite and the normalization problems of the bulk insulators are avoided.

A model of tunneling through a thin-film insulator (based on established approaches for planar tunneling) was developed by Viernow et al. [60]. In this model the tunneling current is expressed as in equation (3.10) with the assumption that the DOS of tip and sample are unaffected by each other. This reduced the problem to the calculation of the transmission probability $T(E, U)$, which consists of the $T_{vac}(E, U)$ term for the vacuum barrier and the $T_{ins}(E, U)$ term for the insulator film

$$T(E, U) = T_{vac}(E, U)T_{ins}(E, U), \quad (3.13)$$

where

$$T_{vac}(E, U) = \exp\left[-2\frac{\sqrt{2m(\Phi - (1/2)eU - E)}}{\hbar}z\right], \quad (3.14)$$

$$T_{ins}(E, U) = \begin{cases} \exp\left[-2\frac{\sqrt{2m(E_{CBM} - eU - E)}}{\hbar}d_{ins}\right] & \text{for } eU + E < E_{CBM} \\ 1 & \text{for } eU + E > E_{CBM} \end{cases}. \quad (3.15)$$

Here, Φ represents the average work function between tip and insulator, and $(\Phi - (1/2)eU)$ is the average barrier across the vacuum gap, E_{CBM} is the energy of the conduction band minimum of the insulator relative to its Fermi level, z is the distance of the tunneling tip from the insulator surface, and d_{ins} the thickness of the insulator film. Any voltage drop across the insulator is neglected.

Using this model, Viernow et al. [60] were able to calculate the $(dI/dU)/(I/U)$ spectra and fit them to the experimental data adjusting only the E_{CBM} term. The authors have also shown that the calculated spectra are insensitive to the tip distance, but they depend on the film thickness.

This model was also used in the present work and will be applied when the STS data analysis will be presented.

3.3.2 $I(z)$ spectroscopy

For the simple one-dimensional model, a tunneling current can be written as in (3.9). Within this model, CCT images can be interpreted as contour maps of the constant DOS. The quantity ρ_s depends on the local chemical nature of the surface. Therefore, its measurement allows to distinguish between different surface elements, which can be difficult to perform in a CCT mode.

From equation (3.9), one can evaluate an apparent barrier height ϕ_{ap} from

$$\phi_{ap} = \left[\frac{1}{1,025} \cdot \frac{d \ln(I/U_b)}{dz} \right]^2. \quad (3.16)$$

This quantity has been generally accepted as an experimental measure characterizing the chemical nature of the sample surface.

There are several possibilities to use $I(z)$ STS to determine the apparent barrier height. Most known is the measurement of the tunneling current during the tip movement towards the surface. For such a measurement, the tip has to be stabilised. This happens in a constant current mode. Hence, the zero point will correspond to the original tunneling settings. After that, the feedback is deactivate and the tip is moved towards the surface by Δz (tip displacement, usually in the nm range). Simultaneously, the current signal is recorded. After that, the obtained spectra can be evaluated according to formula (3.16). In addition, a lock-in technique can be used to measure dI/dz which yields tunneling barrier images [61]. An alternative method for obtaining tunneling barrier images is the measurement of the tunneling conductance vs. the applied bias voltage as has been demonstrated by Olesen et al. [62].

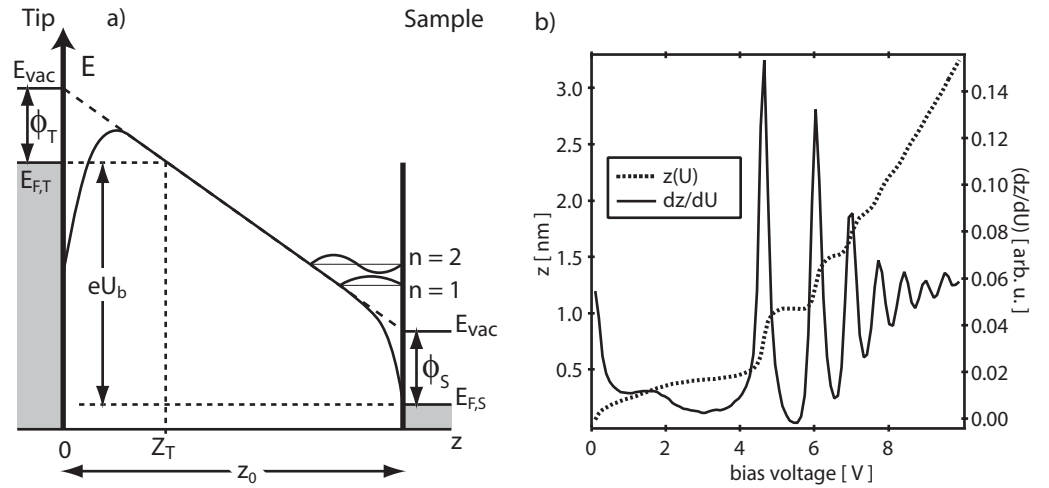
3.3.3 $z(U)$ spectroscopy

Using STM in the field emission regime (in which the applied bias voltage exceeds the averaged work function) makes the energy region above the vacuum level accessible. For this region, Gundlach [63] has calculated both the transmission coefficient and the tunneling current as a function of the applied bias voltage. For metal/insulator/metal systems, it was found that the calculated tunneling current can have superimposed oscillations. This oscillations can be explained by considering the large electron mean free path in the dielectric layer and the specular reflection at the barrier boundaries. Nowadays it is known that the electrons at the Fermi level (which dominantly contribute to the tunneling current) will be partly reflected at the surface and than reflected again at the rising potential within the tunneling barrier. Thus, the electron standing waves can be excited in the vacuum gap in front of the sample surface (see Figure 3.2a). The condition for standing wave formation depend on the electronic potential in the gap, the energy of the field-emitted electrons, and the electron reflectance at the surface. Different surfaces with their own electronic structures will have different reflectances. Hence, the analysis of the distance/voltage characteristics allows a characterization of different surfaces and an estimation of tunneling barriers, respectively.

Figure 3.2 Near-field emission regime.

a) energy diagram for field emission [64],

b) typical $z(U)$ and dz/dU spectra for Ag(001) taken with a Pt-Ir tip.



An approximate description of the experimentally observed high-order resonance states was presented by Coombs and Gimzewski [64]. The resonance condition is fulfilled if an integer number of half wavelengths of the electron wave function will fit between the sample and the rising potential up to the classical turning point Z_T (see Figure 3.2a) if tunneling from the tip to the sample is regarded. The magnitude of the electron wave vector $K(z)$ at a point z between tip and sample is given by

$$K(z) = \frac{2\pi(2me)^{1/2}}{\hbar} \cdot \left(\frac{U}{z_0} \cdot z - \phi \right)^{1/2}. \quad (3.17)$$

Here, z_0 is the tip/surface separation and ϕ the work function. Integration between the classical turning point $z=Z_T$ and the sample surface $z=z_0$ gives a total phase change of πn , where n is the order of the resonance:

$$\pi n = \int_{z_T}^s \left(\frac{(2me)^{1/2}}{\hbar} \cdot \left(\frac{U}{z_0} \cdot z - \phi \right)^{1/2} \right) dz, \quad (3.18)$$

$$\pi n = 2\pi \frac{(2me)^{1/2}}{\hbar} \cdot \frac{2z_0}{3U} \cdot (U - \phi)^{3/2} \quad (3.19)$$

or

$$U_n = \phi + \alpha n^{2/3} F^{2/3}. \quad (3.20)$$

Here, U_n is the voltage of the n^{th} state, F is the field strength in volts per Ångström (Å) and $\alpha = 4.39 \text{ V}^{1/3} \text{ Å}^{2/3}$ is a constant. This equation is almost the same as that obtained by Gundlach [63] except that due to his exact inclusion of the boundary conditions, a factor of $(n-1/4)^{2/3}$ is obtained instead of $n^{2/3}$. Image forces are neglected here. They will distort the barrier mainly in the regions near to the boundaries and will affect only oscillations with a small state number (n).

Measurements of the separation/voltage characteristics $z(U)$ permit to study the oscillatory behaviour of the tunneling current in the near-field regime. The oscillations itself can be directly observed in dI/dU spectra measured by means of a lock-in technique simultaneously with $z(U)$ curves as shown in [64]. But one has to consider that in the CCT mode

$$\left(\frac{\partial I}{\partial s z} \right)_U \frac{\partial z}{\partial U} + \left(\frac{dI}{\partial U} \right)_z = 0, \quad (3.21)$$

and since $((\partial I)/(\partial s))_U$ is a slowly varying function, $((\partial I)/(\partial U))_z = -dz/dU$. Therefore, $((\partial I)/(\partial U))_z$ will be mirrored by dz/dU and steps in $z(U)$ will be transformed into peaks in dz/dU (see Figure 3.2b) and $((\partial I)/(\partial U))_z = dI/dU$ [65].

In contrast to the above described $I(z)$ method, the feedback should be kept active during the $z(U)$ spectra acquisition for keeping the tunneling current constant. If the applied bias voltage increases, the tip will be withdrawn from the sample by the feedback loop to maintain a constant current. The execution of this condition is very important if the STM is used in the near-field emission regime. This is not only necessary for suppressing the electric field strength in vacuum and for preventing a tip crash at the sample surface. It is also necessary for supplying a nearly constant electric field over the sample surface in a vacuum gap, which guarantees defined measurement conditions.

4

Experimental

The investigations were performed in an UHV chamber in the 10^{-11} mbar range (see scheme of Figure 4.1). The details of the equipment can be found in [68].

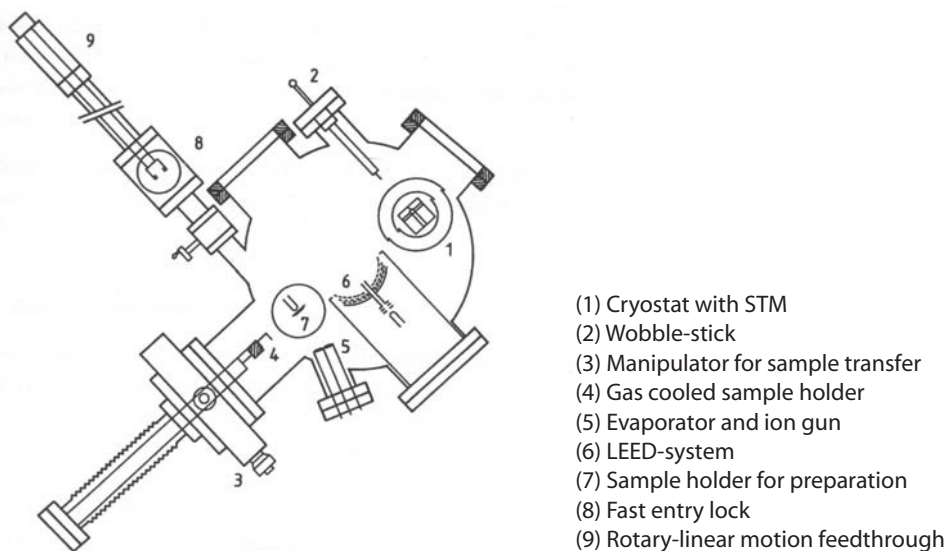
The chamber houses a LT STM unit, a three grid LEED system for surface structure analysis, and a quadruple mass spectrometer for residual gas analysis. For sample preparation, an ion gun for Ar^+ sputtering, an evaporation cell for metal (Co, Mn) deposition, and leak valves for defined gas dosing. There are also facilities for transfer, in-situ exchange, and preparation of the sample and the STM tips.

4.1

Low temperature (LT) STM

The STM unit is located in a cryostat (1) made by CRYOVAC. The flow-through cryostat allows the use of liquid He as refrigerating medium. Thus, temperatures down to 10 K can be reached. In this work, only liquid N_2 was applied for cooling the system down. The temperature was measured by thermocouples and controlled by a regulation system. The lowest temperature attained was 77 K. Working in this temperature region, however, was not possible since oscillations caused by evaporating N_2 inside the cryostat made the STM signal very noisy. At 100 K, the oscillations disappeared. Hence, most experiments were performed at temperatures around 100 K.

Figure 4.1 UHV-system



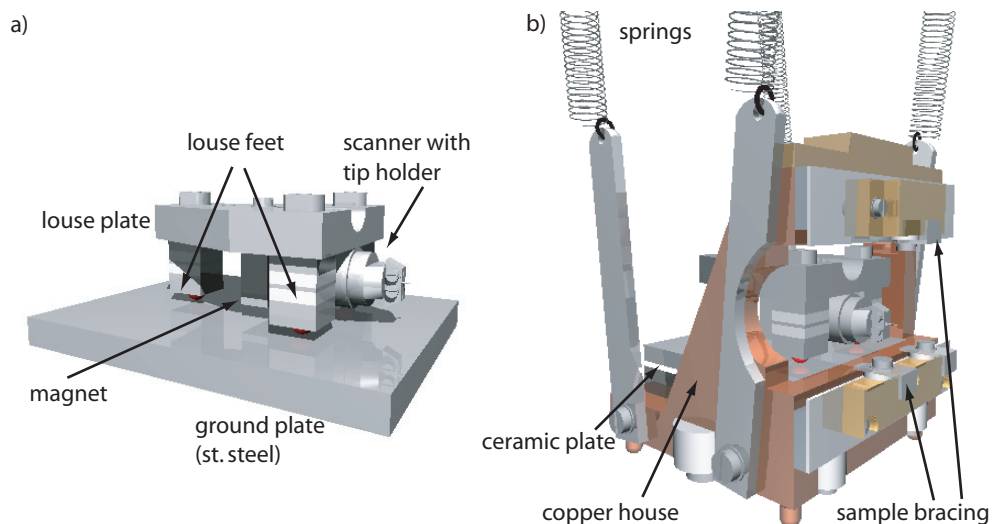
The main part of the STM consists of the scanning system (see Figure 4.2) which keeps the tunneling tip at a certain distance in front of the sample. At the same time, the tip is scanned over the sample surface. The scanner is fixed on a carrying system (“louse”) which allows a coarse approach of the tip towards the sample necessary after the sample transfer. The tube scanner was made from piezo ceramic material Pz27 produced by FEROPERM and was divided into four 90° sectors. At one side, a removable tip holder was attached. This holder was fixed at the scanner by means of a magnet which allows a tip exchange under UHV conditions. The louse was build very light in order to shift its own mechanical resonance towards higher frequencies. Therefore, a magnet was needed to increase

the stability of the louse against the ground plate. The louse together with the ground plate (Figure 4.2a) are placed into a half closed Cu block (“Cu house” in Figure 4.2b) to speed up the cooling down process. A thin ceramic plate (1.5 mm) electrically isolated the louse from the house. The STM unit was placed into the cryostat and suspended by springs to damp the mechanical oscillations of the chamber. The sample was fixed in the sample bracing system by means of three radial arms. After the preparation, about 20 min were needed for cooling the sample in the STM down to 100 K.

Figure 4.2 LT STM:

a) louse with scanner,

b) STM copper house together with louse.



Generally, no essential changes were made to the STM unit. However, it was necessary to reconstruct the sample holder system and adapting it to the standard OMICRON sample holders now used in the group. Due to the new sample holder, a reconstruction of the preparation stage and the transfer system was also necessary.

4.2

Sample preparation

For the oxide film preparation, a Ag(001) substrate crystal of high quality was used. The crystal was cleaned at room temperature (RT) by cycles of sputtering and subsequent heating up to 600-700 K. The Ar partial pressure was 2×10^{-6} mbar and the energy of the Ar⁺-ions was 600 eV. The sample was heated by means of a W filament at the distance of ~ 2 mm from the sample back side. The temperature of the heating system was measured by means of thermocouples.

The oxide films were grown by means of reactive deposition, i.e., by metal deposition in an O₂ atmosphere. In this work, Co (later Mn) were evaporated from an Al₂O₃ crucible onto the Ag(001) substrate. During evaporation, the UHV chamber was filled with high purity (99,998 vol.-%) O₂. The pressure range was set between 10^{-7} mbar and 10^{-5} mbar in order to study the dependence of grown oxide structures on the partial O₂ pressure. No additional calibration of the gauge was needed. O₂ was pumped during inlet which allows to keep the pressure constant during preparation. For studying the temperature dependence of the growth, the substrate was heated at temperatures between 300 K and 500 K during preparation.

The Co and Mn evaporation sources were calibrated by depositing Co and Mn in UHV onto the Ag(001) substrate and by measuring the coverage of the grown

Co (Mn) islands, respectively, by means of STM. The evaporation rate was ~ 0.2 ML per minute. The calibration of Mn source was complicated by the RT Mn/Ag alloying effect. After oxide film preparation and characterization, the films were removed by sputtering and the Ag(001) was cleaned again for further deposition experiments.

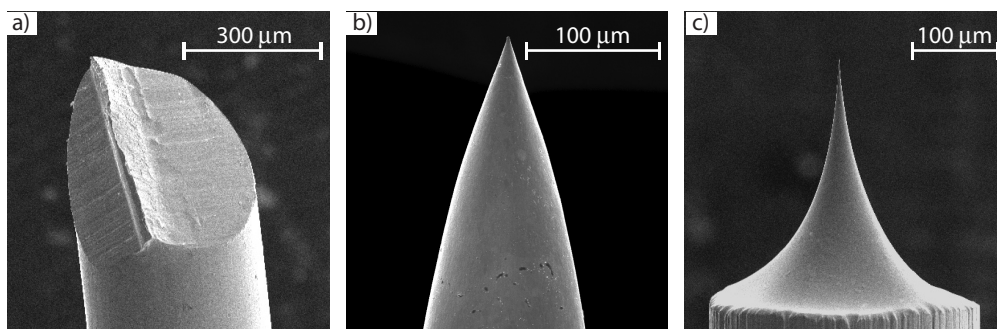
4.3

Tip preparation

The most widely used materials for tunneling tip manufacturing are W and Pt-Ir. Both materials were used in the present work. Several methods were used to prepare sharp tips from the wires. The most simple way is to cut the wire. A Pt-Ir wire (diameter 0.3-0.4 mm) was used for this purpose. In Figure 4.3a, a tip obtained by cutting is imaged by means of scanning electron microscopy (SEM). In spite of its rough surface, a good resolution was achieved with cutted tips. Moreover, since the cutting was performed shortly before introducing into UHV those tips needed no additional cleaning procedures (as will be described below). The next preparation method was electrochemical etching which was used for both W and Pt-Ir tips. The Pt-Ir tips were etched in a melt of NaOH and NaNO₃ by applying an alternating current. After etching, the tips were rinsed with isopropanol and subsequently annealed in an ethanol flame. Figure 4.3b shows a typical SEM image of a Pt-Ir tip obtained by etching. For preparing the W tips, pieces of a W wire (diameter 0.3-0.4 mm) were etched in NaOH solution and subsequently rinsed in isopropanol. Very sharp tips could be obtained in this way (see Figure 4.3c).

Figure 4.3 SEM images of STM tips:

- a) Pt-Ir cutted,
- b) Pt-Ir etched,
- c) W etched.



After introducing the etched tips in the UHV, no resolution could be obtained at the beginning. Several cleaning procedures were necessary. As a first cleaning step, STS was used at RT. Applying a voltage ramp from -6V to 6 V, significant changes were provoked leading to a first cleaning of the tip apex. After that, the cleaning was continued by scanning in the image mode a large sample area. Hereby, the bias voltages was alternated in forward and backward directions (for example forward -8 V and backward 8 V). This procedure led to massive losses of tip impurities dropping on the sample which made a further imaging impossible. The process was repeated on neighbouring clean areas for several times. The cleaning procedure took a long time (typically 4-12 hours) for getting stable tip conditions. When the most coarse contaminants were removed, small particles continued to fall on the surface. This process is illustrated by Figure 4.4. It shows a part of the surface which was continuously imaged. After 30 min the initially relatively clean surface (Figure 4.4a) was strongly contaminated (see image b).

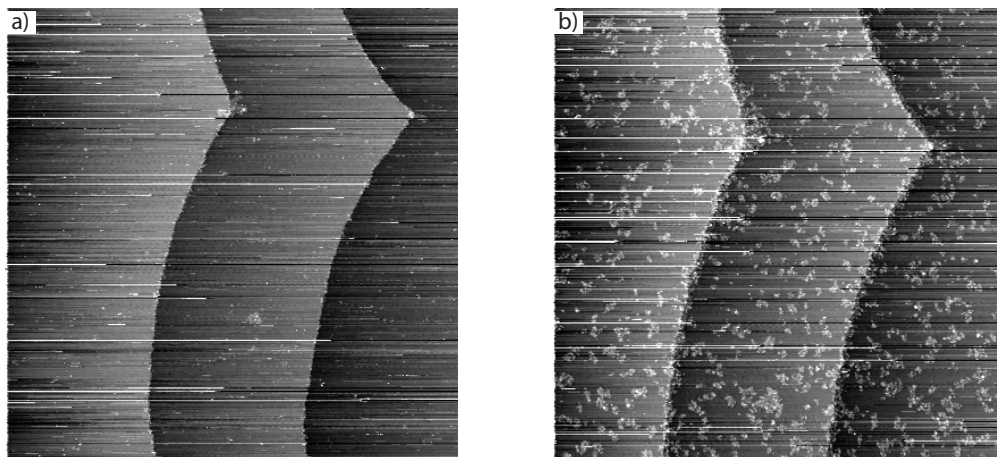
Figure 4.4 STM imaging during tip cleaning procedure on Ag(001):

a) initial image

STM (130×130) nm²,
 $U = -8$ V, $I = 0.3$ nA,

b) 30 min later

STM (130×130) nm²,
 $U = -8$ V, $I = 0.3$ nA.



Another cleaning method used was to apply short voltage pulses during scanning. Within this cleaning procedure, one started scanning at -2 V, then the bias was set to -6 V and subsequently the polarity was alternatingly changed (i.e., between -6 V and 6 V).

All these methods were very time consuming. For reducing tip cleaning time, a special adaptor was later constructed making heating of the tip under UHV conditions possible. It was built in such a way that the tip together with the removable tip holder (see Figure 4.2a) could be placed into the sample preparation stage with the tip towards the W filament usually used for sample annealing. Heating the tip up to 400 K was quite enough to remove the main part of the impurities. This essentially speeded up the tip preparation procedure to 0.5 - 4 hours.

4.4

STM control and data evaluation

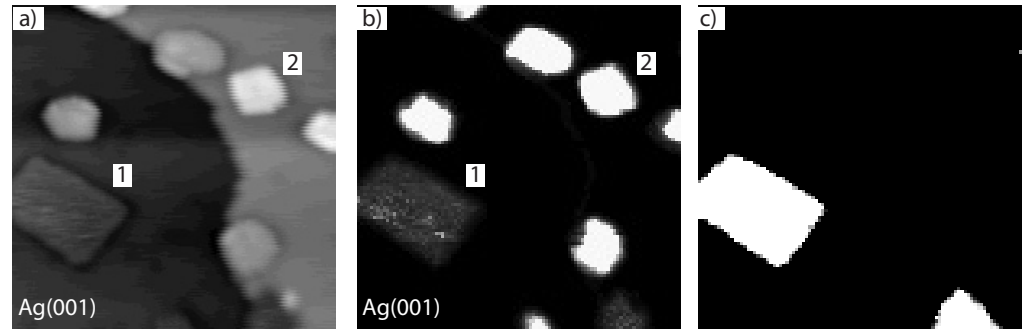
To control the STM electronics as well as all measurement processes, the “Scala 4.1” software from OMICRON was used. Some spectroscopic studies were done with the help of the macro language usually used for nanostructuring. The “Scala” software was also used for acquiring and evaluation of the STS data. However, most of the STS data were evaluated with the help of “IgorPro” from WAVEMETRICS. Since STS is the focal point of the present investigations, one should review this procedure in more detail. In a first step, the spectra ($I(U)$ or $I(z)$) have been recorded. Usually, the “mapping” mode was used for that. The resolution of the STM image was set to 200 points \times 200 points and the spectra were acquired in every second point of the image. The tip was stabilized at certain selected U_0 and I_0 . Then U or z ramps (depending on spectroscopic mode) were applied with an open feed back. The forward channel was used for this application. Simultaneously, the topography was recorded for a correct interpretation of the current maps. At the end, a three-dimensional spectroscopic data set was obtained with 100 points \times 100 points laterally and 100 points vertically for the measured spectroscopic values. This allowed the inspection of the spatial current distribution in each point of an applied ramp (U or z). Figure 4.5 gives an example of a combined STM/STS measurement, applied on CoO islands on Ag(001). In the STM image (Figure 4.5a) two types of islands can be recognised - a rectangular island type (1)

Figure 4.5 STS data evaluation process:

a) STM (130×130) nm²,
 $U = -8$ V, $I = 0.3$ nA,

b) $I(U)$ map at 3.6 V,

c) mask for island type (1).



and one with a more rounded shape (2). In Figure 4.5b, the current map of the islands taken at 3.6 V is shown. A stronger contrast is obtained allowing a better distinction between the island types. Islands of type (2) appear now brighter than the other ones. In the next step, the acquired $I(U)$ spectra were extracted. In order to separate the observed three surface types (islands (1), islands (2), and uncovered Ag(001) areas) a masking technique using “IgorPro” developed by Hagen-dorf [69] was used. In this technique, the areas of interest were marked by using their grey tone level in the current map. According to this mask, the $I(U)$ spectra are separately extracted from the STS data set. Figure 4.5c shows the mask used for extracting the $I(U)$ curves of the type (1) islands.

For the inspection of the STM images as well as for their analysis and processing, the “STML” program written on base of Borland C++ by Kraus was used [70]. Here, the grey scale of the CCTs is adjusted to the relative height of the tip above the surface. Thus, bright areas in the topography correspond to the tip withdrawn from the sample.

5

Characterization of the Ag(001) substrate

For characterizing the growth of the oxide films, the knowledge of the topography of the Ag(001) substrate is necessary. In addition to that, the substrate surface has to be characterized also electronically since it will be used as a reference in the STS measurements. A detailed STM analysis of the behaviour of Ag(001) during sputtering and annealing was already done by I. Sebastian [22]. Here, the main attention was paid to detailed spectroscopic studies of the clean Ag(001) surface and its interaction with O₂.

5.1

Clean Ag(001)

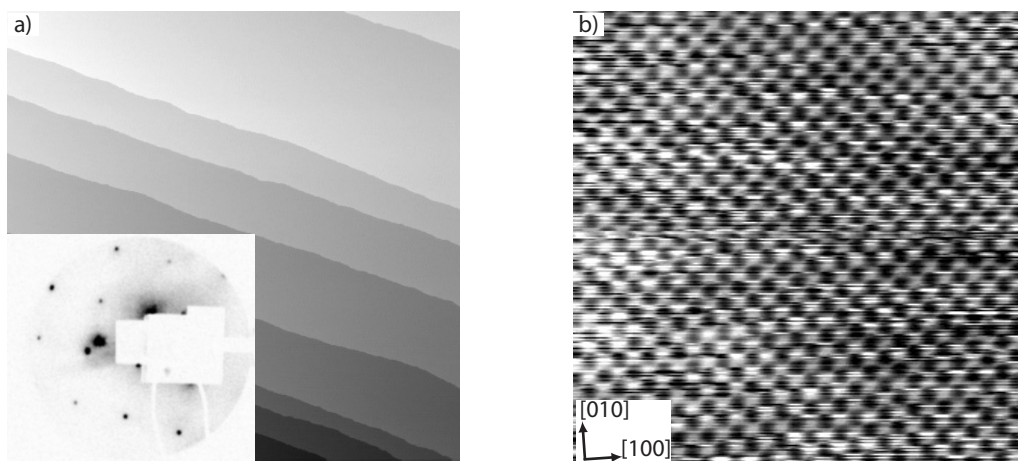
5.1.1 STM /LEED characterization

The well oriented Ag single crystal (miscut less than 0.5°) exhibited already after several cleaning cycles a sharp and brilliant (1×1) LEED-pattern (Figure 5.1a) inset). RT STM images (see e.g., Figure 5.1a) show wide (20-150 nm) terraces and confirm the high quality and cleanliness of the single crystal. Figure 5.1b represents a high resolution CCT image of the Ag(001) surface. Atomic corrugation with (1×1) square symmetry and interatomic distance of 0.3 nm in [110] direction are identified. The atomic resolution was attained if the bias voltage was reduced to values <0.3 V and the tunneling current set between 0.5-5nA. At such settings, the tunneling tip comes closer to the surface. This was necessary to measure the relatively low atomic corrugation amplitude of the Ag(001) surface (typically 0.01 - 0.05 nm). Atomic resolution was obtained with both W and Pr-Ir tips at 300K as well as at 100 K. However, at low temperature, a more stable tunneling junction was attained which essentially ameliorated the image quality.

Figure 5.1 Ag(001) surface:

a) overview image,
STM (350 × 350) nm²,
 $U = -3$ V, $I = 0.1$ nA,
inset: LEED, $E_{\text{kin}} = 156$ eV,

b) high resolution image,
STM (6 × 6) nm²,
 $U = -0.15$ V, $I = 1.5$ nA.



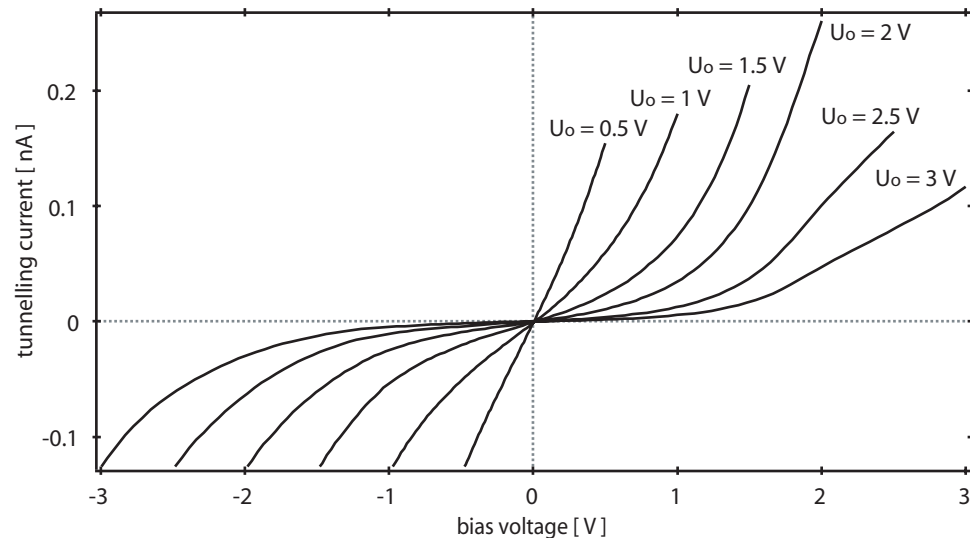
5.1.2 STS characterization

I(U) STS

In Figure 5.2, $I(U)$ characteristics are presented taken with different stabilization distances. The stabilization distance z_0 is determined by the stabilization voltage U_0 . The $I(U)$ curves may drastically depend on the magnitude and, of course, the polarity of U_0 . In general, an ohmic behaviour of metallic parts of the surface is only visible in the $I(U)$ curves, if the absolute value of U_0 is small (< 1 V) [67]. At higher voltages, the width of the tunneling barrier becomes also large and the $I(U)$ characteristics will no longer obey Ohm's law.

Figure 5.2 $I(U)$ characteristics of clean Ag(001) taken at different stabilization voltages with Pt-Ir tip.

Stabilization at $I_0 = -0.13$ nA.

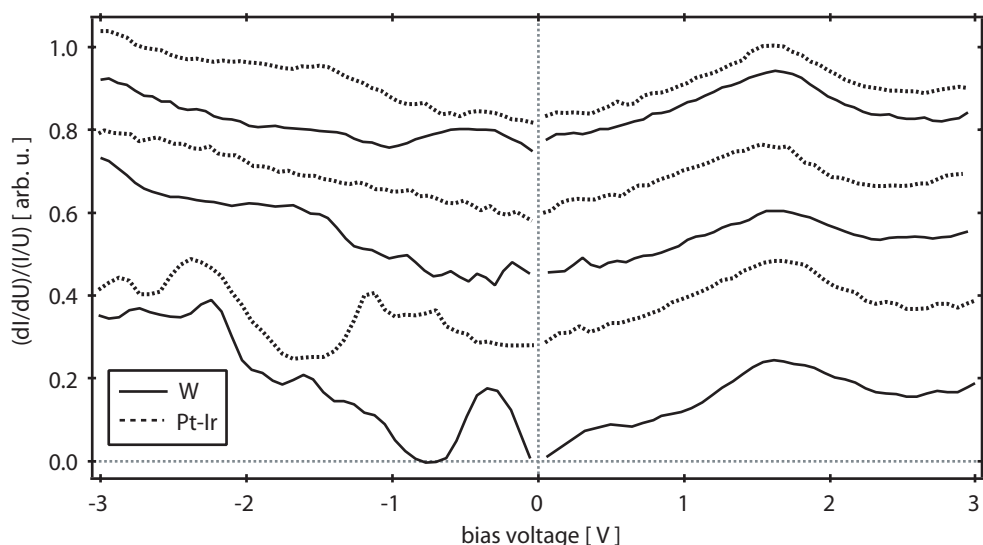


In general, this behaviour was reproduced with several different W and Pt-Ir tips. Only if the tip was not metallic, a drastic deviation was visible in the $I(U)$ curves.

It was, however, important to go deeper into details and find out how the tip material influences the spectroscopic data. In Figure 5.3, several normalized tunneling conductance spectra are shown. The corresponding $I(U)$ characteristics were taken with W and Pt-Ir tip. Several conclusions can be made from the characteristics of these spectra. First of all, the energetic position of the broad peak around 1.6 V was found to be independent on the tip material. This peak was measured in all spectra. Obviously, it is characteristic for the Ag(001) surface and can be used as a spectroscopic fingerprint for Ag in more complex film/substrate situations. It is related to the surface DOS and agrees well with one-dimensional DOS caused by bulk transitions along the ΓX line of the Brillouin zone. This was experimentally confirmed by means of inverse photoemission (IPE) experiments [71], [72]. At a negative bias voltage, several peaks could be observed. They are not directly related to the Ag(001) DOS which is fairly constant in this energy range [73]. Moreover, their position on the voltage axis strongly depends on the tip material and the experimental situation. In the individual experiments the spectra could be reproduced with a high accuracy only at stable tunneling conditions. Since the sample preparation remained constant, the most possible reason for the differences in the normalised

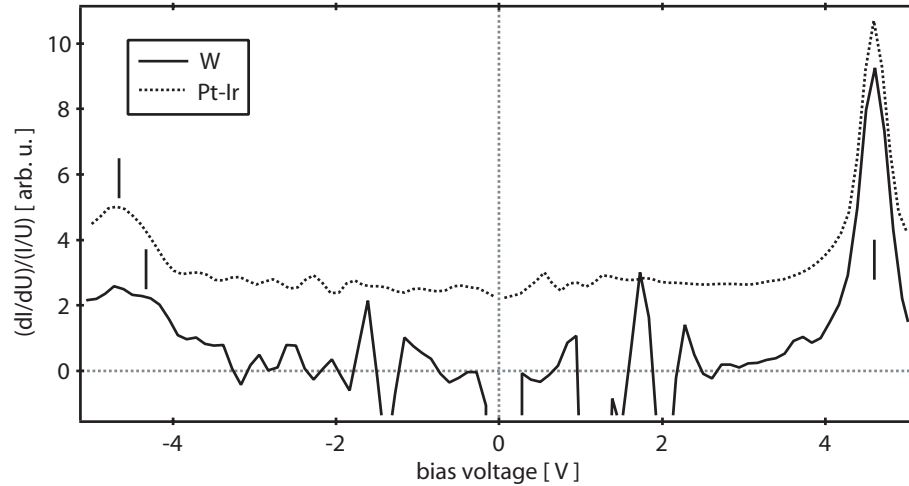
conductivity is the tip. The tip state may be different for the individual experiments and every approach to the surface may influence it. Hence, the spectra also reflect the actual tip state.

Figure 5.3 $(dI/dU)/(I/U)$ spectra taken with W and Pt-Ir tips. All spectra belong to different experiments. Stabilization at $I = 0.1$ nA and $U = -3$ V.



Another situation appears after an enlargement of the bias voltage ramp. Then the influence of the actual tip state is no longer pronounced. In Figure 5.4, normalized curves of tunneling conductance are presented which have been evaluated from $I(U)$ spectra taken from - 5 V to + 5 V. At such relatively high energies, the Fowler-Nordheim tunneling regime is included. This is indicated by an oscillatory behaviour of the tunneling current at $eU > \phi$ which appears already in simple $I(U)$ characteristics (not shown here). The peak at 4.6 V is seen for both tips and one at - 4.3 V only for W and at - 4.6 V only for Pt-Ir. A measurement of the rapidly increasing tunneling current at a fixed tip/sample distance was limited by the restricted dynamic range of the measuring equipment. Only the first peak (sometimes together with the second one) were observed in constant separation mode. The peak at 4.6 V corresponds to the first state of the field emission resonance (FER) predicted by Gundlach [63]. The reason of the resonances is the formation of electron standing waves within the tunneling barrier as described in Chapter 3.3.3 and in detail for Ag(001) in the next section. The position of this peak does not depend on the tip material as far as the tunneling conditions are constant. The peak itself is related to the surface and characterizes Ag(001). The peaks at the negative side are also specific and characterize the actual tip state. They can be reproduced until the tip apex is not influenced by the field in the tunneling junction. It is also important to mention that W tips are less stable. Therefore, the STS measurements were mainly performed by using Pt-Ir tips.

Figure 5.4 $(dI/dU)/(I/U)$ spectra taken with W and Pt-Ir tips with extended voltage ramp. Stabilization at $I = 0.1$ nA and $U = -5$ V.



$z(U)$ STS

This technique is very powerful for studying the surface and the tunneling barrier in the energy region above the work function of the sample and the tip which is not accessible in the normal tunneling regime used for imaging. In this energy range, the formation of electron standing waves can be observed. The electrons are confined in a potential well formed by the surface potential and the potential slope within the vacuum gap. Depending on the polarity of the bias voltage, the standing waves are formed either in front of the sample or in front of the tip (see schemes of Figure 5.5a and b). The formation of the electron standing waves depend on the reflectance of the electrons at the surface. Therefore, the characteristics of $z(U)$ and dz/dU may yield additional information on the electronic structure of the sample surface [74],[75] and can be used as a reliable tool for characterizing local defects [76]-[80]. In addition to this, the surface of the tip can also be studied [64].

There are, however, several important experimental aspects which should be taken into account. In Figure 5.5c, measured $z(U)$ and dz/dU characteristics of the clean Ag(001) surface and of the Pt-Ir tip are shown. The tip/sample separation strongly depends on the bias voltage polarity. For negative voltages, the separation z is by almost a factor of two smaller than for corresponding positive voltages. This means, that for keeping the tunneling current constant, the tip should be moved further away from the surface in the latter case. The oscillatory behaviour became more evident after a numerical differentiation of the $z(U)$ curves. The peak shapes together with their positions on the energy scale show also clear differences depending on the polarity. The DOS and the normal transmission factor are the main reasons for the observed differences. Both factors determine the width of the barrier and hence the geometry for the standing waves. Moreover, the tip DOS is usually unknown and may spontaneously change during the tip approach and during STS. This problem is related to the fact that our method of tip fabrication does not always yield tips with a controlled shape. It could be solved by applying an in situ tip refinement performed by sputtering and subsequent thermal-field treatment [81].

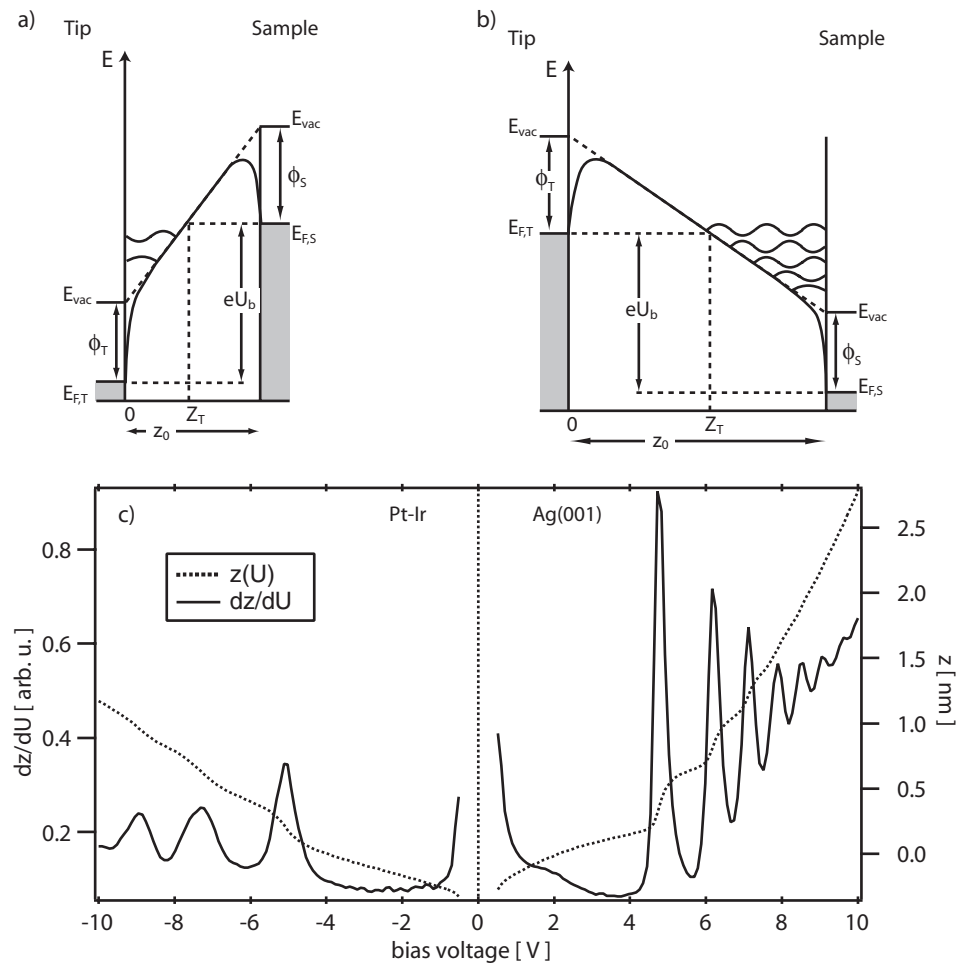
Figure 5.5 Scheme of electron standing wave formation in front of:

a) sample surface,

b) tip surfaces.

c) $z(U)$ and dz/dU plots deduced from experiments.

$I_0 = 0.1$ nA.



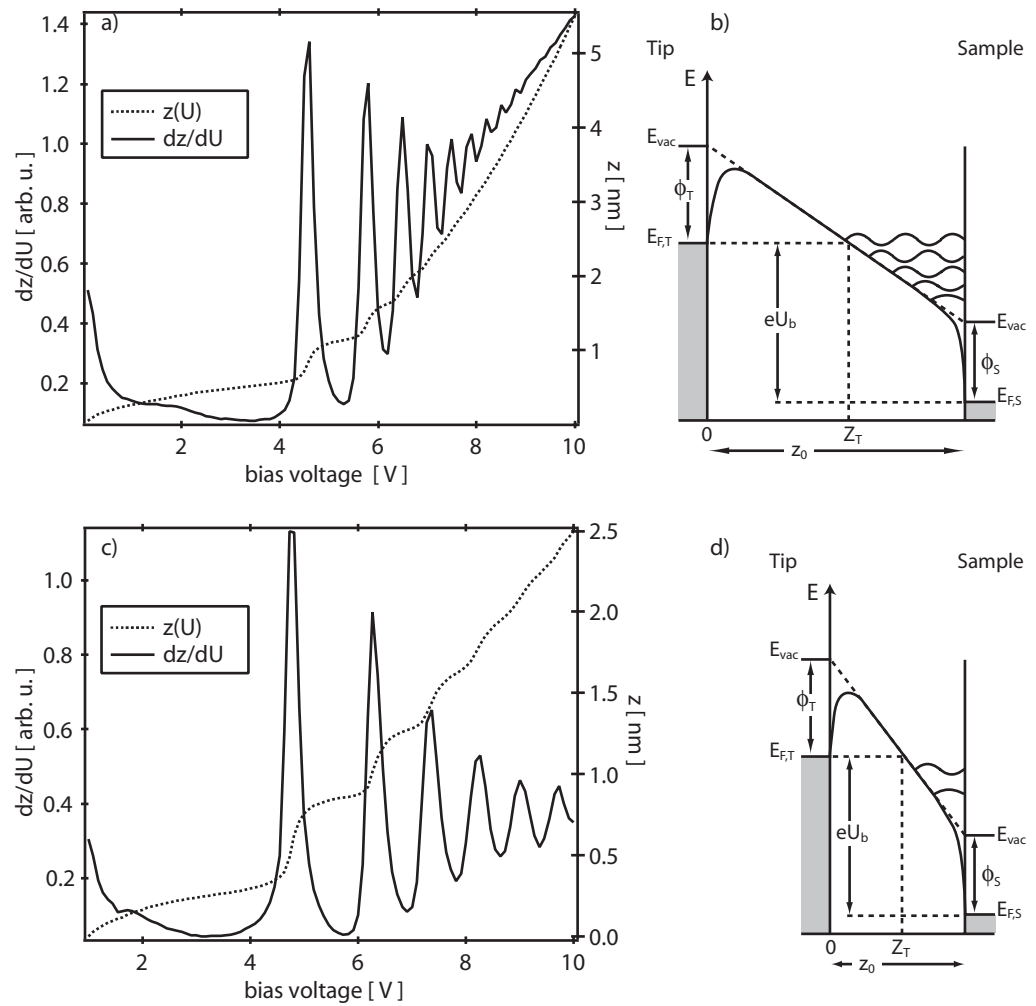
Annealing the tips in high electric fields removes the contaminants and allows a manipulation of the tip shape. In some experiments, stable tunneling and spectroscopic conditions could be achieved and reproducible spectra could be acquired in that cases.

In Figure 5.6, results of two experiments with different tip shapes are shown. The information on tip shape was deduced from the resolution of the CCT images which have been simultaneously acquired with the STS data. It was observed that a sharp tip led to a wider vacuum separation (see Figure 5.6 a) in comparison to a blunt one (see Figure 5.6c). Correspondingly, a larger number of oscillations was observed in the dz/dU curves for a sharp tip (14 peaks in Figure 5.6a) in comparison to the blunt one (6 peaks in Figure 5.6c). The energy diagrams presented in Figure 5.6b and d should help to understand the observed differences. The differences in the peak intervals and also in the number of the peaks can be attributed to the electron confinement effect in a declined electric potential near the sample surface. The main point is that a sharp tip under $I = \text{const}$ is moved farther away from the surface at U_{max} . As a consequence, a large number of wave packets fits into the potential well. Note that the wavelength of the wave packet is inversely proportional to the square root of the wave vector K . This means that the wave length is not much changing with U . This fact can directly be seen in Figure 5.6b and d. The shape of the potential plays a minor role. This is in a good agreement with the experimental data of

Figure 5.6 Distance/voltage dependence for (a) sharp and (c) blunt Pt-Ir tips.

$I_0=0.1$ nA

Energy diagrams for sharp (b) and blunt (d) tips.



Suganuma [75] measured for peaks in the differential tunneling conductance spectra of Au(111). The influence of the tip curvature and of the interface potential on the oscillations in the tunneling conductance observed with STM has been theoretically studied by Pitarke et al. [82].

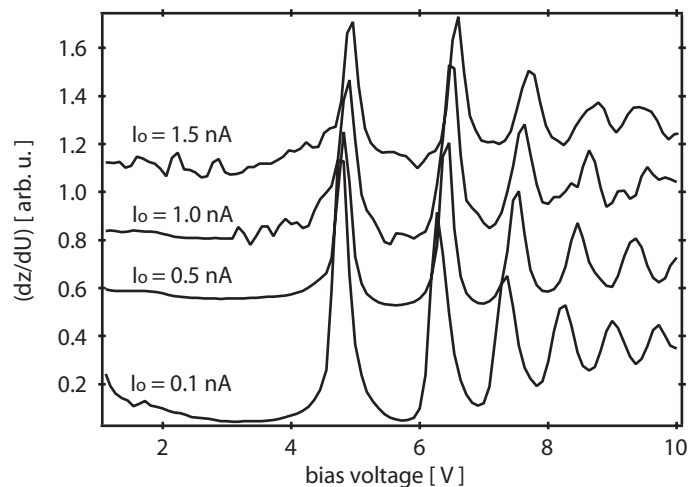
The situation becomes more complicated if a semiconductor surface is considered. A band bending effect on the dI/dU spectra has to be assumed to explain a parallel shift of the peaks in the spectra [83]. For *n*-type Si(001), it was experimentally demonstrated that light irradiation of the sample stimulates an upward band bending. This affects the energy position of the resonance states, whereas the intervals between the states remain uninfluenced. Kubby et al. [84] have observed a stacking-fault contrast in conductance and topographic images of the Si(111)-(7×7) surface as a function of the bias voltage. The strongest contrast was found at those energies where the standing waves are formed between the surface and the buried interface. This was also predicted by one-dimensional resonant tunneling theory. Probably, a similar situation appears if insulating layers are epitaxially grown on a metal surface.

Scandella et al. [80] assumed that the sample work function can be estimated from the position of the first FER peak. This assumption is only partly correct. Nevertheless, independent on the tip material, in all experiments the first resonance was observed at energies around 4.6 eV if $I_0=0.1$ nA was used. This is

in agreement with the experimentally measured work function of Ag(001) (4.6 eV, see [71]). It is, however, well known that the conditions for exciting electron standing waves can be influenced by stabilization parameters (U_0, I_0). As a result, an energetical peak shift occurs.

Figure 5.7 shows dz/dU spectra taken in the same experiment, but at different tunneling currents. After a spectrum was recorded, I_0 was increased by a value of 0.5 nA and the same bias voltage ramp was applied. It is obvious that the higher the stabilization current, the higher the energies of the resonance states. The energy diagram of Figure 5.6b can be used to explain this situation. For stabilization at a higher current, the tip comes closer to the surface. This leads to a contraction of the potential well in the vacuum and, therefore, to a shift of the resonance states to higher energies.

Figure 5.7 dz/dU curves obtained from $z(U)$ spectra. Stabilization current I_0 was increased in steps of 0.5 nA. Note, that higher stabilization currents shift all resonant states towards higher energies.



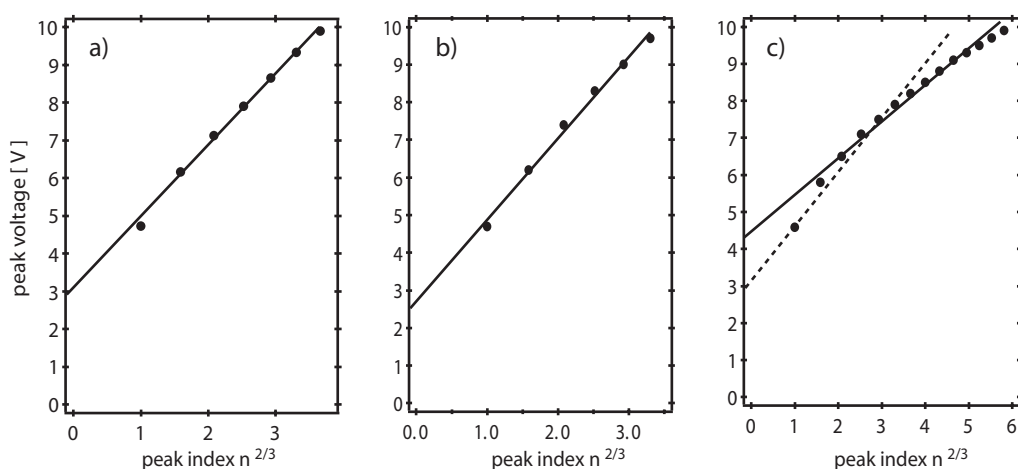
In this measurement, a shift of 0.2 V between the first peaks of the spectra taken at 0.1 nA and at 1.5 nA was obtained. Unfortunately, it was not possible to perform experiments at higher currents. As it is visible from Figure 5.7, already at 1 nA some instabilities appear in the tunneling junction. A further increase of the current caused irreversible tip changes. Hansmann [85] has performed an experiment with Cu(001) where the tunneling current was changed from 1 nA up to 100 nA and the corresponding spectroscopic changes were studied. The observed shift of the first state was 0.5 V.

Despite the observed peak shift an important information can be extracted from the measurements by means of two methods. Both methods were developed by Coombs and Gimzewski [64] and were experimentally checked for different systems by Kolesnychenko et al. [86]. One method deals with the energetic peak positions depending on the peak number. Assuming that the field strength (F) remains constant and $(n + 1/4)^{2/3} \approx n^{2/3}$ for $n \gg 1$, one finds from equation 3.20 that the resonance peak positions have an energy which is proportional to the power of two-thirds of their number $V_n \sim n^{2/3}$. Therefore, the plot of the voltages of the peaks in the dz/dU curves versus the order of the resonance in the power of two-thirds should be linear and the intersection of the linear fit with the voltage scale should correspond to the work function of the sample [86]. The reliability of this method strongly depends on the resonance state number and also on the correct numbering of the peaks, which requires that only one emitting and one reflecting surface contribute to the spectra which is not the case for rough tips.

Such plots of spectra including seven (Figure 5.5), six (Figure 5.6c) and fourteen (Figure 5.6a) peaks found at Ag(001) using Pt-Ir tips with different tip shapes are presented in Figure 5.8. The work functions of 2.9 eV and 2.6 eV obtained from the plots (a) and (b) are still too small to agree with the true work function of 4.6 eV measured for the Ag(001) surface [71]. However, the 4.4 eV value deduced from plot (c) seems to be a more plausible result. These strong deviations of the deduced work functions are due to the high resonance state number approximation used in the model. More reliable results can be achieved if more than fourteen resonance peaks are available in the measurement. This is only possible with an extended bias voltage ramp. In [64] 36 peaks and in [86] 27 peaks have been measured by voltage ramps of 30 V and 25 V, respectively. This exceeds the capability of the used equipment. In the present work only ramp of ± 10 V could be performed.

Figure 5.8 Plot of the voltage position of dz/dU peaks vs. $n^{2/3}$:

- a) spectrum of Figure 5.5 (7 peaks),
- b) spectrum of Figure 5.6c (6 peaks),
- c) spectrum of Figure 5.6a (14 peaks).



Nevertheless, the reliability of this method can be demonstrated by considering the result shown in Figure 5.8c. The dotted line in Figure 5.8c represents a linear fit over only the first seven peaks. A work function value of 2.9 eV can be deduced. This is in good agreement with the value deduced from the plot of Figure 5.8a where only seven peaks were present due to the blunt tip. Hence, this evaluation method does not depend on the tip shape.

However, the problem of the wrong peak numbering can rise. A correct peak numbering is problematic if more than one emitting (or reflecting) surfaces are involved into the tunneling process. Therefore, a method is required that does not depend on a correct indexing. Coombs et al. [64] have proposed to use the voltage separations of the adjacent peaks instead of their actual value for avoiding the indexing problem. This procedure requires a higher number of resonances and, therefore, was not used in the present work.

I(z) spectroscopy

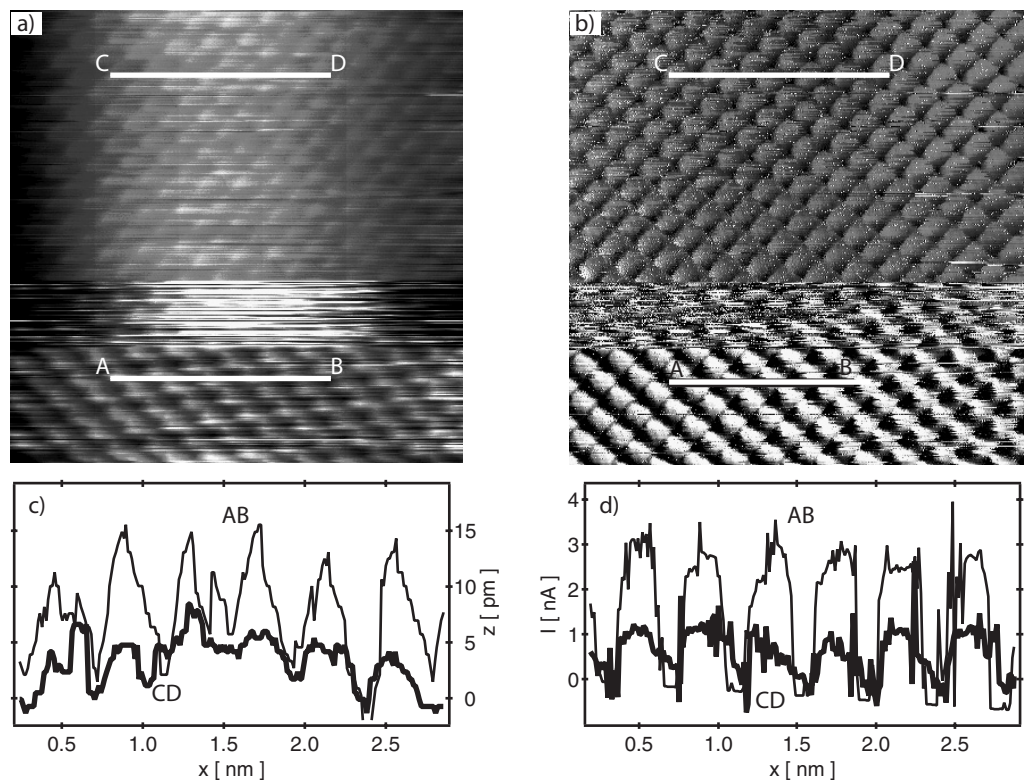
Since the beginning of STM work, a detailed information on the tunneling barrier and in particular on the barrier height has always been of great interest. First investigations of this problem were done by Binnig et al. [87].

There are several different ways to extract informations on the tunneling barrier. One of these is the analysis of the $I(z)$ characteristics as described in the theoretical part (Chapter 3.3). This method turned out to be very sensitive to the chemical specificity of the surface and can be used to distinguish between different oxides on Ag(001). Therefore, the experimental details will be presented later in this work, where specific metal/oxide/vacuum/metal tunneling junctions will be analysed (Chapter 6.5.2).

In Figure 5.9a, a high resolution CCT image of the clean Ag(001) surface is shown together with the corresponding current image (Figure 5.9b). The experiment was performed in such a manner, that the signal was acquired in forward and backward channels. In the forward channel, the z -displacement was gathered whereas in the backward channel the tunneling current variation along the scan line was registered. As a result, the relative z -displacement (i.e., the corrugation shown in Figure 5.9c) and the changes in the tunneling current (shown in Figure 5.9d) are obtained.

Figure 5.9 RT measurement.

- a) Ag(001)
STM (5×5) nm²,
 $U = -0.1$ V, $I = 3$ nA,
- b) current image (constant height mode),
- c) z variation along the scan line AB and DC in (a),
- d) I variation along the scan line AB and DC in (b).



After recording of about 30% of the image, the tip state suddenly changed. This induced pronounced changes in the imaging contrast seen in both topography and current representations of the sample. The tip change induced a modification of the tunneling barrier. The intensities of the line profiles taken from topography and current images (compare AB and CD scans in Figure 5.9c and are reduced at least by a factor of two after the tip change. The dependence of the atomic corrugation on the tunneling barrier width was studied by Seine et al.

[89] and Olesen et al. [90]. Shuster et al. [61] recorded the dI/dz signal using the lock-in technique. The tunneling barrier images can be obtained in this way simultaneously with the topography images.

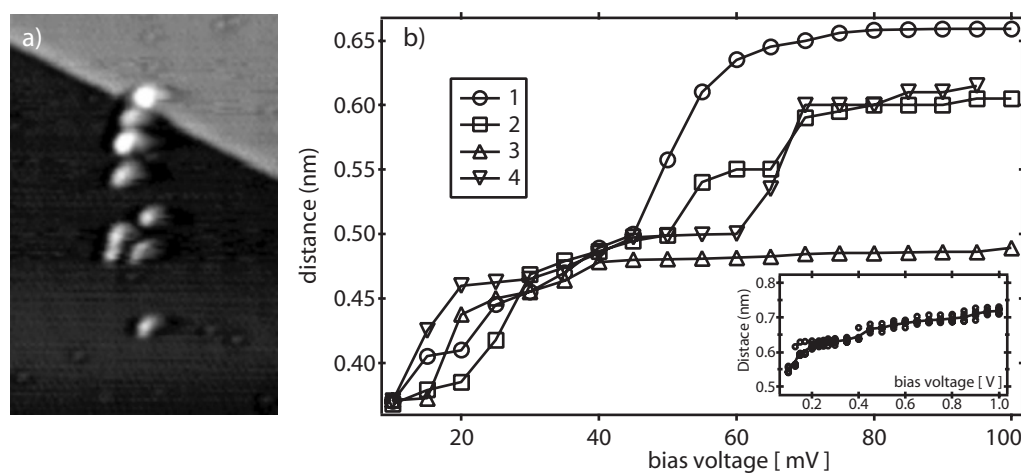
For Ag(001), a better surface resolution is obtained if the tunneling current is recorded instead of z -displacement (compare Figure 5.9a and b). This resolution can be increased if one reduces the regulation speed of the regulation system and increases the scan speed. In this case, however, the information in the topography channel will be completely lost. Nevertheless, this method is more reliable if the atomic structure of a weakly corrugated system has to be investigated [24].

The tip/sample separation is very important for the theoretical calculations and simulations of the barrier. Therefore, several experimental attempts were made in this study to estimate the tunneling distance between the Pt-Ir tip and the Ag(001) surface. For this purpose, the $I(z)$ spectroscopy mode with an open feed back circuit was used (see Chapter 3.3.2). The bias voltage was decreased down to the mV region to reduce effects of a high electric field similar as in [91]. All experiments were performed at 100 K. At 10 mV, the tip approach towards the surface was performed in a step wise manner (usually 0.01 nm) until a small bump was created on the surface (see Figure 5.10a) [92]. Then, the bias voltage was increased by 10 mV and the same procedure was repeated. A tunneling current of 0.1 nA was used in all experiments. Four experiments were performed and their results are presented in Figure 5.10b where the distance changes, at which bumps were created are plotted vs. the bias voltage. Numbers from 1 to 4 correspond to different experiments. In Figure 5.10b, the inset corresponds to another serie of experiments where the bias voltage ranged from 0.1 V to 1 V.

Figure 5.10 Measurement of vacuum separation at 100 K.

a) bumps on Ag(001),
STM (10×15) nm²,
 $U = -3$ V, $I = 0.1$ nA,

b) z approach vs. bias voltage from 10 mV to 100 mV
inset: from 100 mV to 1 V.



In spite of the same stabilization parameters (I_0 , U_0), different distances for the bump creation were observed. Only at voltages below 40 mV all curves look quite similar. At voltages above 60 mV, curves 2 and 4 run nearly the same way whereas curves 1 and 3 have a difference of almost 0.2 nm above 60 mV. A tendency of a linear dependency was observed for all curves above 70 mV. This is also visible in inset of Figure 5.10b. Several plausible assumptions were made to understand the process of bump creation and to explain the differences observed in Figure 5.6b.

The main problem was to decide whether the bumps are formed by direct tip/sample interaction or by the field. Since the used bias voltages and the tunneling current were relatively low and no voltage pulses were applied, phenomena like high-temperature field evaporation, field-gradient-induced surface diffusion, and field-emission-assisted liquid cone formation [93] can be excluded. For such processes, much larger (<0.6 nm) vacuum gap widths are necessary. Tsong [91] has shown that only for distances <0.4 nm a transfer of atoms by the tip/sample interaction is possible. Nevertheless, the influence of the field can not be completely neglected since it can still determine the direction of the atom transfer. Experimentally, all bumps were observed on the Ag(001) surface. Additionally, the size of the generated bumps was fairly the same for all four curves depicted in Figure 5.10b. Since the local field and the bump size could be controlled and were found to be independent on the tip approach, different stabilization positions in the initial spectroscopic stage may explain the differences of the curves in Figure 5.10b.

A qualitative analysis of the field between tip and surface was made by using “Mathematica” [94]. The potential distribution between tip and sample was calculated for two tip shapes under the assumption that their z -position in front of the sample are equal. For both calculations, the same bias voltage was used. The only difference was in the tip radius R . More complicated calculations of the potential energy for metal/vacuum/metal tip systems were done by Ciraci [95].

Considering the case where $R \gg z$ (dotted lines in Figure 5.11a), the equipotential lines run almost parallel to the surface. Here, the tunneling junction equals a plate capacitor where no field gradients arise. A somewhat different situation takes place if $R \geq z$ (solid curves in Figure 5.11a). For such geometry, the potential displays a field gradient in r direction and causes the highest field strength directly under the tip. In present experiments, the tip is moved towards the surface by a fixed value. However, the stabilization point z_0 depends on the tip shape. In contrast to the field emission regime, at low bias voltages the tip with smaller radius will be stabilised closer to the surface in comparison to bigger ones (see Figure 5.11b). In the case of the blunt tip, electrons from larger areas will contribute to the tunneling current allowing stabilization further from the surface (larger z_0). This dependence at least qualitatively describes the differences observed for the curves in Figure 5.10b.

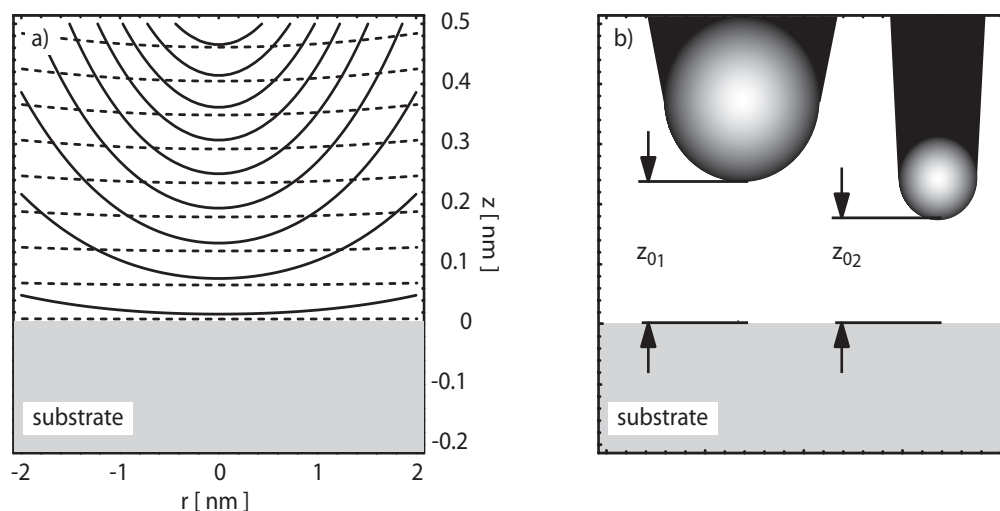
Finally, it has to be mentioned that the bump creation in $I(z)$ STS can be used for a deliberate fabrication of nanometer structures. It was, however, not studied how stable such structures will be at elevated temperatures. The technique of bump creation can be also used to resharpen the tunneling tip, since significant improvements in resolution was observed immediately after the bump creation.

Figure 5.11 Tip/sample

problem

a) equipotential lines for tips with different radii R :
 solid line - $R \geq z$,
 dotted line - $R \gg z$,

b) sketch explaining the differences of the curves shown in Figure 5.10b.



5.2

O₂ and Ag(001)

When the experiments on clean Ag(001) surface were completed, Co oxide films were deposited, annealed, and studied. Afterwards, the films were removed in order to prepare the crystal for the next growth experiments. After several deposition and removing cycles, an unexpected change of the substrate surface was found. In the STM images (see, e.g., Figure 5.12a), the Ag(001) surface was covered with small defects (i). Their density was always below $10^{18}/\text{m}^2$ corresponding to a coverage of 0.05 monolayer (ML).

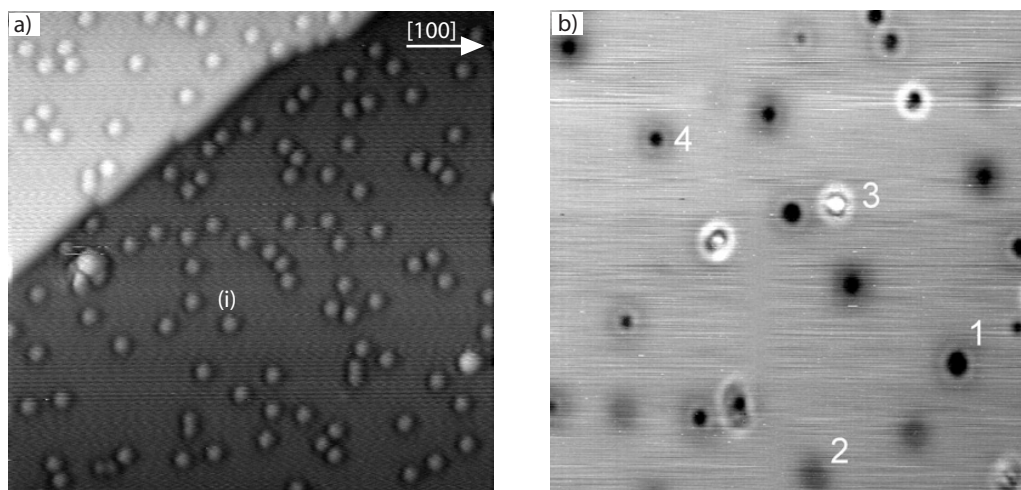
At this point several questions arise. What is the nature of the defects? In which way did they come onto the surface?

Since the defect density was independent of time, they could not be explained by adsorption from the gas phase. Therefore, one has to assume that they are resulting from the bulk by surface segregation. As the defects were not observed on the native Ag substrate, they are introduced by the preparation of the Co oxide films. Consequently, Co and O atoms are the only candidates for explaining the defects. For Co atoms, it is known that they can diffuse at temperatures >420 K into the Ag crystal and form a kind of surface alloy [96]. Thus, one can speculate that the observed defects are Co atoms, just segregated from the bulk at elevated temperatures. However, individual Co atoms on Ag(001) surface look quite different [22]. This is demonstrated in Figure 5.12b showing an STM image of Ag(001) where 0.05 ML of Co was deposited at 470 K [22]. Numbers from 1-4 denote four different defect types as classified in [22]. Some defects are vacancies in the substrate surface layer (1), some are located beneath the surface layer (2). Other defects display a “sombbrero”-like contrast and have filled (3) or unfilled (4) centres. In any case, the defects induced by Co have quite a different appearance than those imaged in Figure 5.12a. Thus, the nature of the latter can not be explained by the adsorption of or interaction with Co atoms.

Figure 5.12 Defects on Ag(001).

a) STM (12×12) nm² at 100 K, $U = -0.25$ V, $I = 1$ nA.

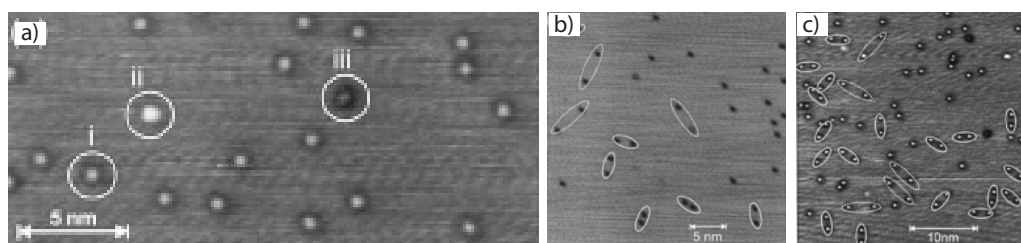
b) 0.05 ML Co on Ag(001) depos. at 470 K [22], STM (30×30) nm² at RT, $U = -1.4$ V, $I = 0.2$ nA.



There remains the other candidate, i.e., the O atoms. In Figure 5.13, STM images of O atoms on Ag(001) are shown which were taken from the literature [97]. The O atoms were dissociatively adsorbed at 140 K on the Ag(001) surface. The O atoms as revealed in Figure 5.13a display striking similarities with the defects shown in Figure 5.12a. Some additional hints for explaining the surface structure shown in Figure 5.12a can be taken from [97]. At negative bias voltages, three different adsorbate contrasts were observed at 50 K (see Figure 5.13a). They were attributed to O atoms residing in different positions on Ag(001), i.e., in four fold hollow sites (i), in on-top sites (ii), and in bridge sites (iii). The atoms in the hollow sites (i) were interpreted to reside in the energetically favoured position, while the two other ones (ii, iii) reside in the metastable positions. Only one of the contrasts (i) is observed in Figure 5.12a which probably results from the different adsorption path of the O atoms from the bulk and the slightly different measurement temperature (100 K). Therefore, it is quite reasonable to assume that the defects in Figure 5.12a are related to O atoms. As an additional specificity of O atoms on Ag(001), a characteristic voltage dependent contrast behaviour has been found [97]. At positive voltage, the atoms appear as dark depressions (see Figure 5.13b) whereas at negative bias they appear as bright protrusions (see Figure 5.13c).

Figure 5.13 O atoms ads. on Ag(001) surface at 140 K [97]

a) STM (30×10) nm², $U = -1.44$ V, $I = 0.3$ nA 50 K,
 b) STM (32×32) nm², $U = 0.66$ V, $I = 0.5$ nA 55 K,
 c) STM (36×36) nm², $U = -0.78$ V, $I = 54$ nA 55 K.



The same contrast behaviour was observed in the present study as shown in Figure 5.14a,b. From -0.1 V to -2.5 V, the defects appeared as bright protrusions (see Figure 5.14a) and from 0.1 V to 2.5 V as dark depressions (see Figure 5.14b). In order to explain a contrast behaviour, $I(U)$ STS measurements were performed. The tunneling spectra (Figure 5.14c) and the normalised tunneling

conductance curves (Figure 5.14d) were taken for both the defect and the Ag(001) surface. The differences of the $I(U)$ curves (Figure 5.14c) provide the reason of the contrast dependence. At negative voltage, one obtains almost the same tunneling current for Ag(001) and for the small defects (i). However, for positive voltage, the current on the defects is lower than on Ag(001). In the CCT mode, therefore, the tip has to approach to the surface more closely in order to reach the stabilization current. Surprisingly, in the normalised tunneling conductivity spectra (Figure 5.14d), no pronounced differences are detected. This is the consequence of the observation that at positive voltage the $I(U)$ characteristics on the defect sites and on Ag(001) look similar and differ only in magnitude. Moreover, the tunneling area during spectra acquisition is probably larger than the defect itself and a larger part of the signal comes from the surrounding Ag(001) surface. In addition, the peak between 0 V and -1 V in the $(dI/dU)/(I/U)$ spectra (Figure 5.14d) is caused by the local electronic structure of the tip (in the current experiment W-tip was used).

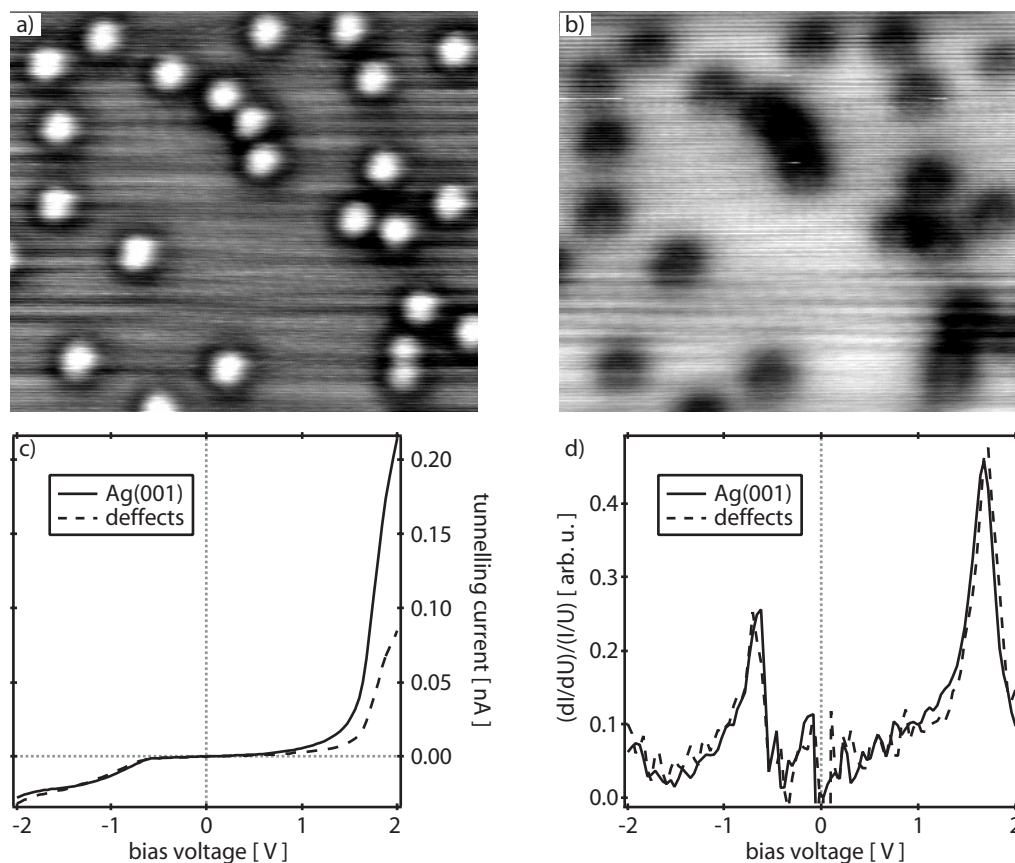
Figure 5.14 Bias voltage depending contrast reversal of the defects.

a) STM (5.5×5.5) nm²,
 $U = -0.25$ V, $I = 2$ nA,

b) STM (5.5×5.5) nm²,
 $U = 2$ V, $I = 1$ nA,

c) $I(U)$ characteristics,
stabilization at -2 V, 0.05 nA,

d) normalised tunneling
conductance derived from
spectra in c).



There are also other studies of O₂ on Ag(001). Rocca et al. [98] investigated the O₂ adsorption on Ag(001) during an exposure of 3000 Langmuir (L) at 150 K. They found adatoms on a missing row reconstructed surface (stable for crystal temperatures < 300 K). After annealing the surface O adatoms were observed in four fold hollow sites. Moreover, a surface oxide phase was detected after CO oxidation by O atoms in hollow sites. In addition, subsurface O has been identified. Two models have been proposed for the subsurface O. In one model, the O atoms reside in octahedral positions of the second Ag plane. In the other model, the O atoms are situated in tetrahedral sites between the first and the second Ag plane. According to DFT studies by Crombette et al. [99], the

favoured O position is the octahedral interstitial site. Rocca et al. [100] studied also the annealing behaviour of the subsurface O₂ up to 415 K. They found an enrichment of O in the subsurface region induced by segregation from the bulk. It was also shown that this segregation effect was not present if Ag(001) was exposed to 86 000 L of O₂ at 470 K [100]. This was explained by O diffusion into the bulk. O diffusion into the Ag bulk was also observed for Ag(110) at temperatures > 470 K [101]. In [98], irreproducibility of results was explained by the sample history due to differences in the O bulk concentration. Hence, O diffusion into the bulk and O segregation are certainly involved in the present study of Co oxide film growth which are performed at similar temperatures. It is quite reasonable to assume that the effects imaged in Figure 5.12a are segregated O atoms. In order to get more insight into the O/Ag(001) interaction, several adsorption experiments were additionally performed.

5.2.1 Adsorption at 77 K

All adsorption experiments were done at 77 K. The sample was cooled with liquid N₂ and then the chamber was filled with O₂ at a 10⁻⁶ mbar partial pressure. Afterwards, the sample was transferred into the STM cryostat and analysed at 100 K.

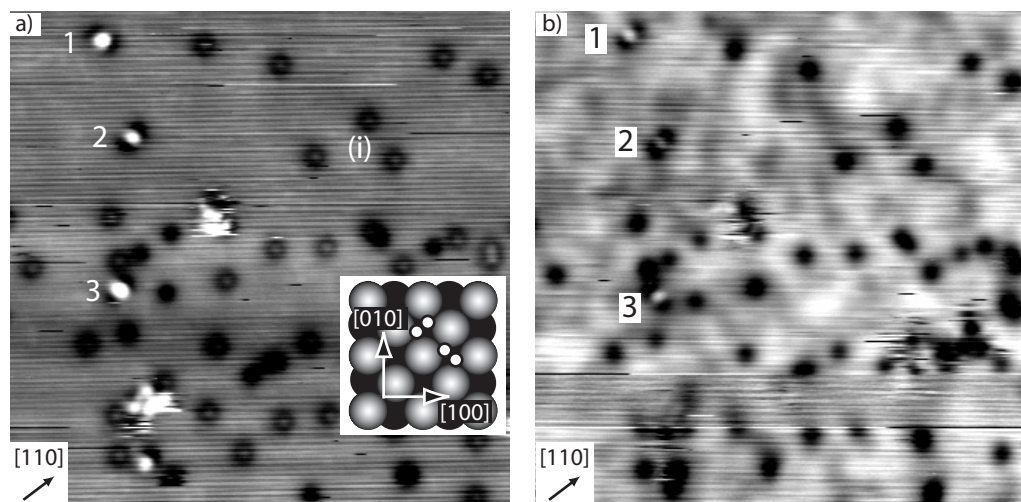
Figure 5.15a shows STM images of the Ag(001) surface which was exposed to 9×10⁻⁶ mbar of O₂ for 90 minutes (~37000 L). Several defect types are observed. One (i) is obviously the same as described above and may be explained by segregated or adsorbed O atoms. The other defects are marked by (1), (2), and (3). The centre of these defects appear as bright protrusion with two symmetrically distributed dark wings. This is the typical contrast of O₂ molecules adsorbed on Ag(001) [102]. According to Messerli et al. [102], the molecular binding site is the four fold hollow site with the O atoms pointing to the bridge sites (see model in the inset of Figure 5.15a). Thus, within the rectangular unit cell, two orientations of the O₂ molecule are possible. It is known that O₂ remains molecularly chemisorbed on Ag(001) at temperatures of 130 - 120 K [103]. No dissociation was observed at 100 K even at higher O₂ exposure [104]. Correspondingly, at 77 K no atomic O adsorption occurs. This is in line with the performed experiment (Figure 5.15a). In Figure 5.15b, the same area is imaged with a bias voltage of 0.5 V. Comparing both images, it becomes obvious that molecules marked as (1) and (3) are rotated by 90° whereas molecule (2) did not change its orientation. This rotation is probably caused by the local electric field of the tunneling tip during scanning.

Most strikingly, however, is the blurred appearance of the Ag(001) surface below the O adsorbates particularly visible in Figure 5.15b. After comparing series of images taken on the same area, it was concluded that the blurring effect in Figure 5.15b is not induced by surface, but rather by subsurface defects, i.e., by subsurface O. Therefore, it was investigated whether it is possible to deliberately induce subsurface O formation by annealing Ag(001) in O₂ atmosphere. In these experiments, a temperature of ~480 K was applied similar as for preparation of the Co oxide films.

Figure 5.15 Adsorption at 77 K, $p(\text{O}_2) = 9.6 \times 10^{-6}$ mbar, $t = 90$ min (37000 L)

a) STM (21×21) nm², $U = 2$ V, $I = 0.1$ nA
insets: hard sphere model of O₂ molecule (small white circles) from [102],

b) STM (21×21) nm², $U = 0.5$ V, $I = 0.1$ nA.



5.2.2 Annealing in O₂

For the annealing experiments, the freshly prepared Ag(001) surface was exposed to O₂ at a pressure of 6×10^{-6} mbar for 20 minutes (~ 5400 L). Afterwards, the sample was cooled down to 100 K and the STM/STS studies were performed. Typical images of the surface are shown in Figure 5.16. It is obvious that the Ag surface was drastically changed during annealing in O₂. A large number of “black dots” are formed. They are marked as (1) and are different from the O atoms (i) described above (see Figure 5.12a).

In Figure 5.16b the surface is imaged in high resolution. The contrast of the black dots appears slightly changed due to the image processing which was performed for resolving the atomic rows of the Ag(001) substrate. As a guide for the eye, the rows are marked by lines. It becomes obvious, that the “black dots” are placed in four fold hollow sites (see circle in Figure 5.16b).

The “black dots” were already observed in previous investigations on the Ag(110) surface. Zambelli et al. [105] irradiated adsorbed O₂ molecules with UV light and observed a light-induced formation of “black dots”. The latter could also be induced by subsequent sample annealing. They concluded, therefore, that the “black dots” contain O in some form, although its nature remained unclear. Considering the fact that the “black dots” did not react with CO and considering the possible O diffusion into the Ag bulk, one could tentatively assign the dots to subsurface O.

The surface shown in Figure 5.16a was very stable at low temperature and allowed STS studies. The $I(U)$ STS data are shown in Figure 5.16c. The spectra were obtained after stabilising the tip at -2 V, 0.1 nA, and ramping the bias voltage from -2 V to 2 V. The current characteristics show a clear difference on Ag(001) and the “black dots”. It is interesting that the “black dots” remain dark after a change of the bias voltage polarity.

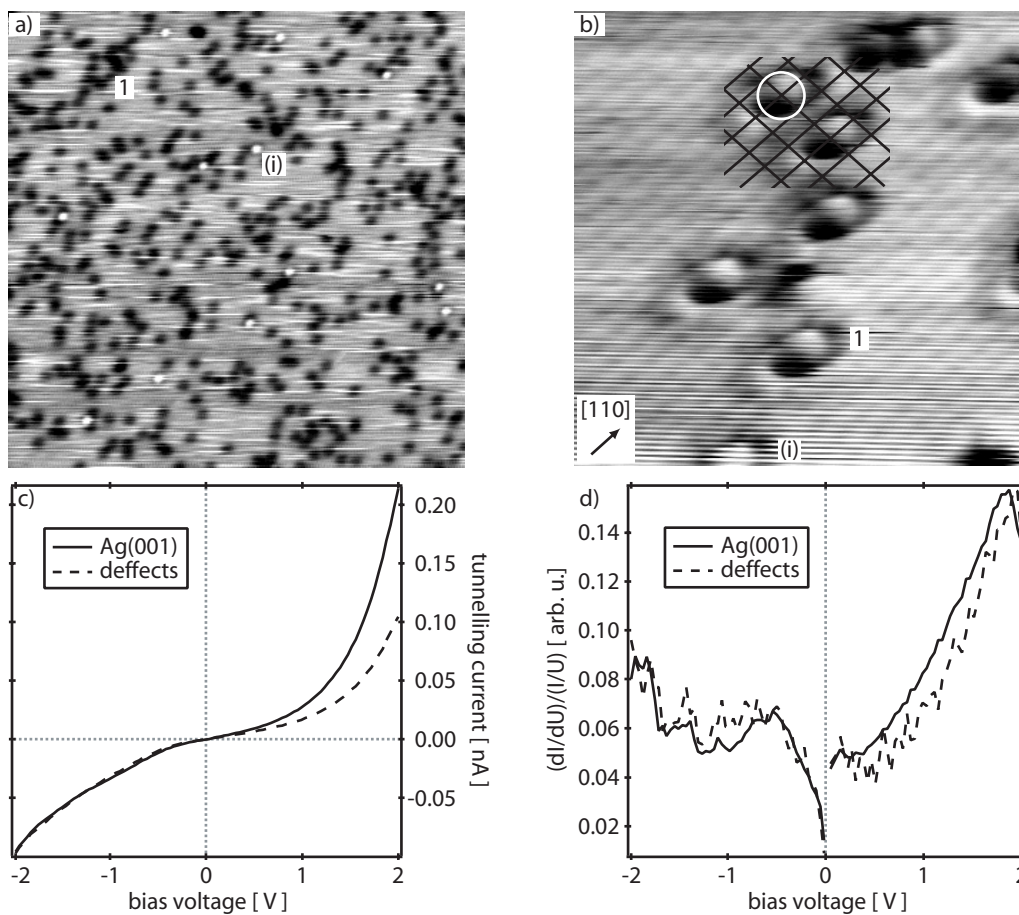
Figure 5.16 Annealing
Ag(001) at 480 K in $p(\text{O}_2) = 6 \times 10^{-6}$ mbar,
 $t = 20$ min (~ 5400 L)

a) STM (30×30) nm²,
 $U = -3$ V, $I = 0.1$ nA,

b) STM (4.5×4.5) nm²,
 $U = -0.5$ V, $I = 0.3$ nA,

c) I/U characteristics
stabilization at -2 V 0.1 nA,

d) normalised tunneling
conductance derived from
spectra in c)



The $(dI/dU)/(I/U)$ spectra shown in Figure 5.16d should be more sensitive to the local chemical differences. However, no pronounced differences were detected between the “black dots” and the Ag(001) substrate. At negative bias voltages, the spectra are influenced by the local electronic structure of the tip. At positive bias voltages, a strong peak is observed for the “black dots”. It is similar to the pronounced peak in Figure 5.14d on the defect site (i), i.e., on the segregated O atoms. However, it is shifted towards higher energy (1.8 V). This shift was reproducibly measured with different tips. Therefore, the influence of the tip state can be ruled out and the shift is characteristic for defect. According to Savio et al. [108], the presence of O on the Ag(001) surface might affect s and d bands which may shift states towards higher energies.

In summary, an interaction of O_2 from the gas phase with Ag(001) was observed and studied at different substrate temperatures and different exposures. It was found that at 77 K O_2 is mainly molecularly adsorbed. At temperatures above 450 K, the formation of “black dots” related to O was observed. In addition, a shift of the Ag surface state peak in $(dI/dU)/(I/U)$ spectra was found. The presence of defects as in Figure 5.12a was assumed to be due to the O accumulation in the bulk and later segregation towards the surface.

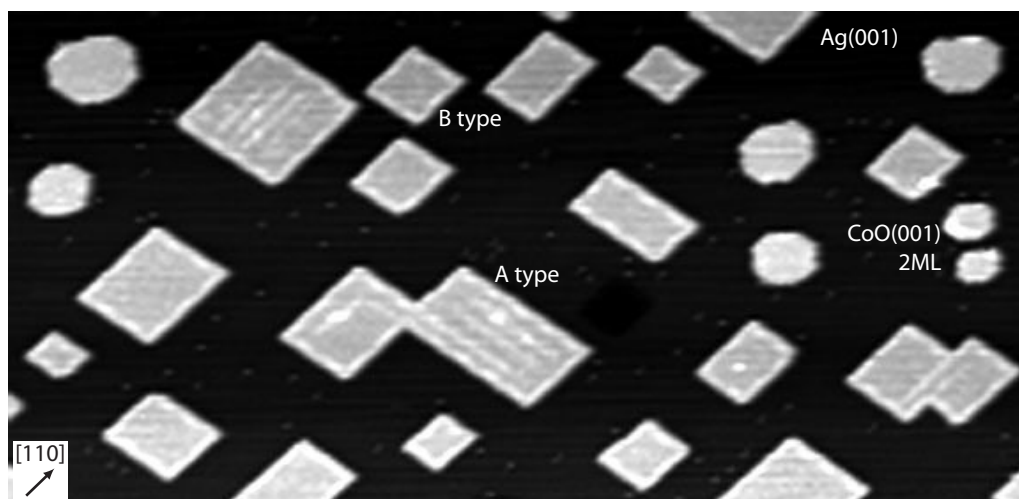
6

Growth of Co oxides on Ag(001)

In the initial stage of Co oxide growth on Ag(001), a large variety of island types have been observed [26]-[29], i.e., precursor islands, double layer CoO(001) islands and Co oxide islands of (111) orientation depending on the preparation conditions. All island types can be partly found embedded into the Ag(001) surface.

In this work, LT STM and STS are applied for characterizing the formation of Co oxide islands in more detail. Figure 6.1 gives an impression of the complexity usually found in the growth experiments. About 0.3 ML of Co was deposited in 2×10^{-6} mbar of O₂ at 390 K and subsequently annealed at 420 K. Rectangular islands and islands with a more rounded shape are simultaneously formed. The rectangular islands are oxide precursor islands. One type (denoted in the following as A type) has been already described by Sebastian [22]. This kind of islands reveal a row-like superstructure of bright features. There is another precursor (B type) which was not observed before. This precursor does not display a superstructure. In addition to that, there exist round islands of smaller size which correspond to 2 ML thick CoO(001) islands [27]. In order to classify all observed island types (not all of them are visible in Figure 6.1) in more detail, the precursor states are considered first.

Figure 6.1 Overview image. 0.3 ML of Co deposited at 390 K and annealed in UHV at 420 K. STM (115×64) nm², $U = -3$ V, $I = 0.1$ nA.

**6.1****A type precursor**

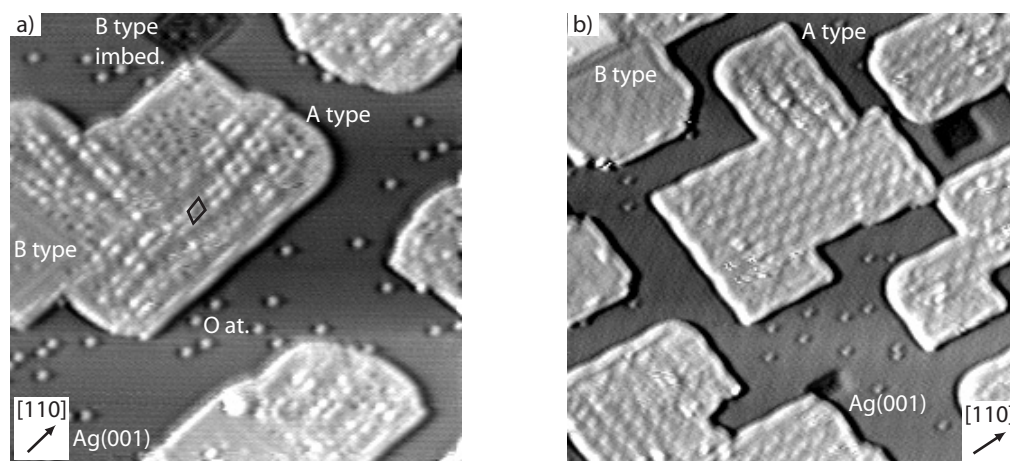
Up to now, the structure of the precursors has not been clarified. Due to the instability of the tunneling junction at RT it was difficult to obtain atomic resolution on their surfaces in previous experiments. In contrast, the LT STM allowed a more stable imaging and delivered reproducible results. Two examples are given in Figure 6.2. Here, 0.2 ML Co has been evaporated in an O₂ atmosphere (5×10^{-6} mbar) onto Ag(001) kept at ~ 380 K (a) and ~ 410 K (b), respectively. In the images, islands of A type and B type can be identified. Part of the B type precursor islands are partly into Ag(001) (dark rectangular areas in Figure 6.2). In addition, the O induced defects described in Chapter 5.2 are present. The stripe-like superstructure of the A type precursor is clearly revealed in the CCT

images. The ordering of the stripes improves with rising temperature. The distances between the stripes are 1.5 - 1.8 nm. The stripes are quite regularly distributed in the precursor islands. Usually they run parallel to the step edges of the precursor islands, i.e., along [110]-like directions. Along the superstructure rows, rhomb-like bright protrusions are revealed (as marked in Figure 6.2a). In Figure 6.2b, the island marked as A type precursor displays areas of different degree of order. The upper part of the island appears similar to the islands in Figure 6.2a which can be judged from the rounded island corners and the less ordered superstructure. The rest of the island in Figure 6.2b, however, looks different. The island corners are rectangular and the superstructure stripes are parallel to the island step edges.

Figure 6.2 High resolution images of A type CoO precursor (0.2 ML of Co evaporated)

a) STM (40×40) nm²,
 $U = -3$ V, $I = 0.1$ nA,

b) STM (54×54) nm²,
 $U = -2$ V, $I = 0.1$ nA.

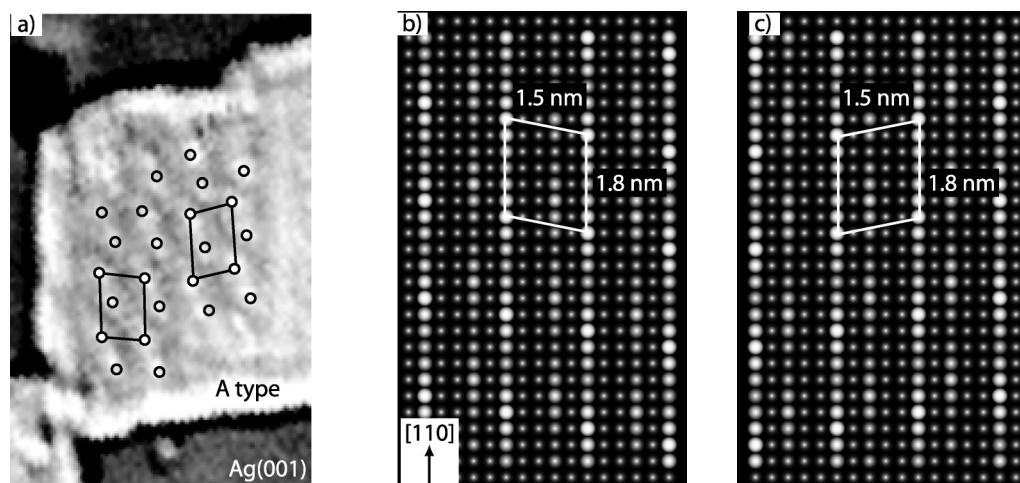


In Figure 6.3a, an area of the well ordered superstructure is shown with higher resolution. A scheme of the STM contrast is displayed in Figure 6.3b. The contrast along the superstructure stripes changes in a wave-like manner with a periodicity of 1.7-2.0 nm along [110]-like directions. The brightest sites in two neighbouring lines are always shifted by one or two atomic distances along [110]-like directions. As it can be seen from Figure 6.3a, a rhomb-like unit mesh of 6×7 atoms can be drawn. This structure was also observed in a mirrored arrangement (see Figure 6.3c) due to the two fold substrate symmetry. Such rhomb-like units can be also identified in less ordered areas of the superstructure (see Figure 6.2a).

Figure 6.3 A type precursor:

a) STM (12×7) nm²,
 $U = -3$ V, $I = 0.1$ nA,

b), c) image scheme of 7×6 precursor unit mesh according to STM image in (a).

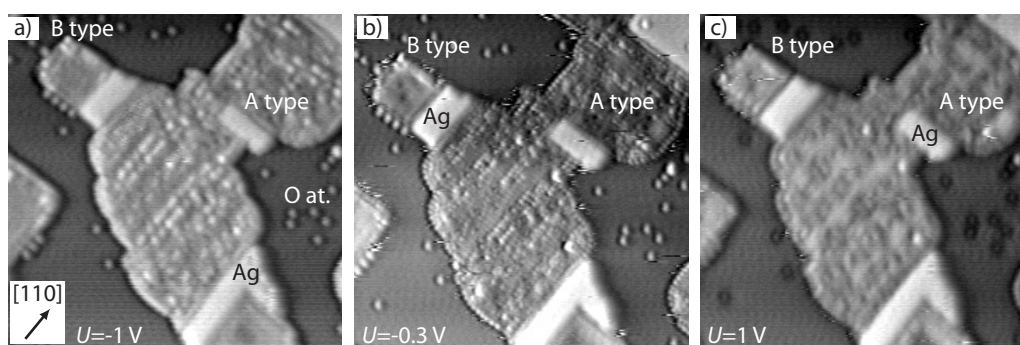


Searching for better imaging parameters, a series of images with different tunneling conditions were acquired. The main results are shown in Figure 6.4. A sample area was imaged which displays a large A type precursor island. In addition, small B type islands and some Ag islands are visible which are characteristically enclosed by the precursor. The latter are formed due to Ag rearrangement during the oxide film growth [27]. For the A type islands, it was observed that the bright sites of the superstructure stripes (which correspond to the corners of the unit cell) appeared as bright protrusions only at negative bias voltage (Figure 6.4a, b). For positive bias voltages, they appear as depression in comparison to their surrounding (see Figure 6.4c). This contrast reversal is very characteristic for O atoms (Chapter 5.2). Therefore, it is reasonable to assume that the corners of the A type precursor unit mesh are formed by O atoms.

Figure 6.4 Contrast reversal of A type precursor (0.2 ML of Co evaporated).

$I = 0.1$ nA for all images,

STM (54×54) nm² for all images.



6.2

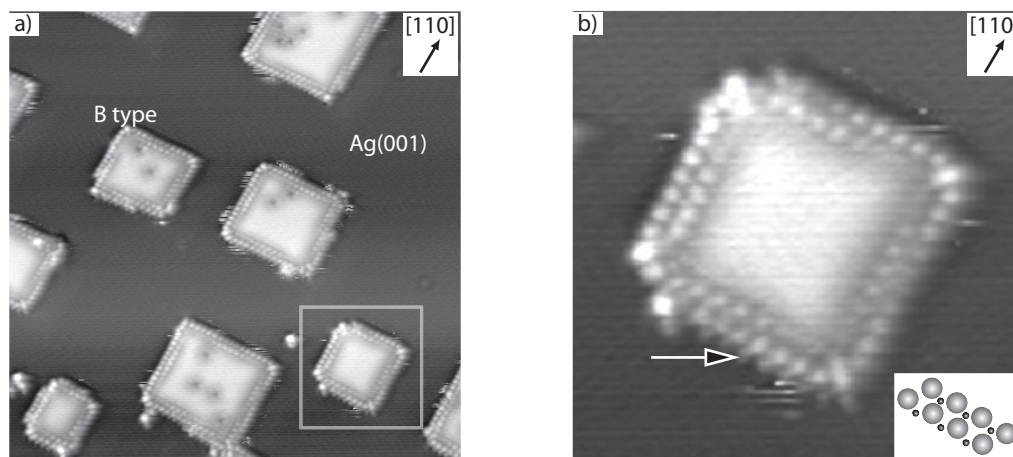
B type precursor and transition to CoO(001)

As already shown in Figure 6.2 and Figure 6.4, the A type precursor islands were always observed together with B type precursors. The ratio between the A and B type islands depends on the substrate temperature. The higher the temperature, the larger the number of B type islands. At a temperature around 430 K, only B type islands remained on the surface. Using this temperature during deposition, also yield exclusively B type islands. This is demonstrated in Figure 6.5 which shows STM images of a surface where 0.2 ML of Co was deposited in 5×10^{-6} mbar of O₂. The step edges of the islands are strictly oriented in [110]-like directions. The inner part of the islands appears to be flat and no atomic structure is observed there. Along the island edges, however, atomic features with a distance of 0.3 nm are resolved. Probably, in this measurement both the O and the Co sublattices were imaged. If one assumes that the small features indicated by the arrow in Figure 6.5b belong to Co, a structural model can be derived (see the inset of Figure 6.5b). According to this model, the island edges display a hexagonal structure where the Co resides in three fold O hollow sites. This is a surprising result for (001)-like islands and corresponds to a one-dimensional reconstruction of the step edge. Annealing the islands above 450 K, however, induces a disappearance of the edge reconstruction. This can be partly seen on the island (1) in the STM image of Figure 6.6a. The corresponding island structure is schematically shown by the hard sphere model (1) in Figure 6.6b. This model, of course, does not completely represent the real structure. Since it does not describe the wave-like modulation seen along the

Figure 6.5 High resolution image of B type precursor (0.2 ML of Co evaporated at 430 K).

a) STM (25×25) nm²,
 $U = -0.25$ V, $I = 0.1$ nA,

b) STM (5×5) nm²,
 $U = -0.25$ V, $I = 0.1$ nA,
 inset: hard sphere model of the step edge.



island step edges. The modulation is probably induced by alternating positions of the precursor atoms on top and hollow sites of the substrate.

During annealing, some other types of islands did appear, i.e., islands (2), (3), and (4) of Figure 6.6a. In contrast to islands (1), atomic resolution was also obtained in the inner part of the island. A (1×1) square symmetry can be identified. The structure corresponds to the (001) type of island. An interatomic distance of 0.3 nm was measured [27]. Islands (2) are of almost octagonal shape whereas islands (3) are of more rounded shape. Islands (3) reveal a pronounced tendency for orienting the step edges along (001) directions. Additionally, it is obvious that islands (3) and (4) appear to be brighter and hence higher in a topographic representation. In comparison to the height of islands (1) (~ 0.1 nm at -1 V 0.1 nA), the measured height of islands (3) is larger by a factor of two and islands (4) are even three times higher. From this observation it was deduced that the islands (1) and (2) have a height of 1 ML, whereas islands (3) and (4) have a height of 2 ML and 3 ML, respectively. From the characteristic features of the islands of type (3), it is obvious that they correspond to bi-layer CoO(001) islands which have been already described in previous studies [26]. The islands of type (4) show similar features. They deviate from islands (3) only by their height. Therefore, it is assumed that islands (4) correspond to a tri-layer CoO(001) island. The corresponding hard sphere models of all island types (top view) are also shown in Figure 6.6b. Since all island types were simultaneously observed, it is suggested that they represent stages of island transformation during annealing. During the transformation, the rectangular B type precursor possessing [110] oriented steps changes to a bi- or tri-layer islands of CoO(001) displaying a [100] step orientation. The octagonal shape of islands (2) can be obtained from island (1) just by removing the corner atoms. At this stage, four sides of the octagon-like islands are still aligned in [110]-like direction whereas another four edges appear and grow in [100]-like direction. In contrast to the [110]-like edges, the [100]-like edges have a non polar nature (Co and O atoms alternate within one atomic row). Islands (3) have round shapes and it was difficult to define their orientation. But they are oriented in such a manner to have as less polar edges as possible [26], [27]. The finally formed islands (4) correspond to CoO(001) and display only non polar step edges which is energetically most favourable

[27]. Obviously, the minimisation of the energy of the step edges is one of the driving forces for the island transformation. This process is completed if 3 ML thick islands are grown.

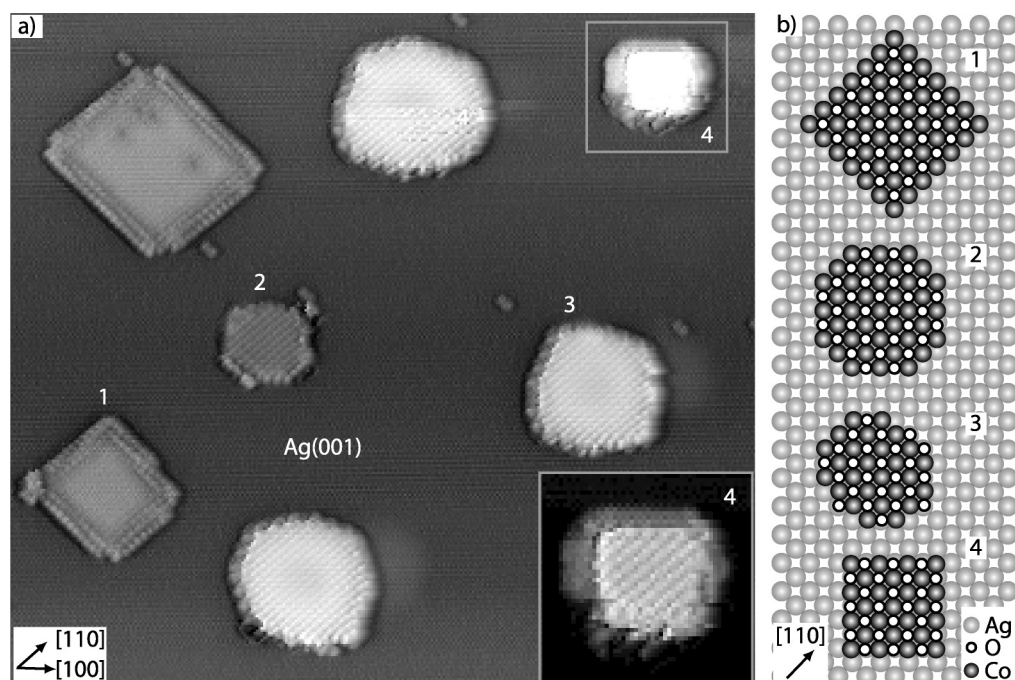
Figure 6.6 Transition from B type precursor (Figure 6.5) to bi- and tri-layer CoO(001)

a) STM (33×33) nm²,

$U = -1$ V, $I = 0.1$ nA,

inset: island 4 zoomed in,

b) hard sphere model represent 4 transition steps visible in Figure 6.6a.



6.3

(111) oriented Co oxide

For specific preparation conditions as will be described below, (111) oriented Co oxide islands were found [27],[29]. Figure 6.7a shows an overview image of a Co oxide film where an (111)-like island is visible. In Figure 6.7b, this island is imaged with atomic resolution. It displays a smooth surface having a three fold hexagonal (1×1) symmetry. An interatomic distance of ~ 0.3 nm was deduced from the measurement. The (111)-like islands were usually found on the Ag(001) surface in a partly embedded form, i.e., surrounded by Ag or by CoO(001) areas (as shown in Figure 6.7a). Small (111) oriented islands usually display a hexagonal shape (Figure 6.7c). Two equivalent types of them were found. In Figure 6.7d they are represented by hard sphere models. One of the three equivalent step edge directions of the hexagonal islands is always aligned parallel to $[110]$ -like directions of the Ag(001) substrate. The coexistence of the two hexagonal domains has already been anticipated by Sebastian [22] who analysed LEED results of a several ML thick CoO film. Smooth (111) oriented Co oxide islands are only found for small island size. Larger islands (> 30 nm) as shown in the image of Figure 6.8a display a pattern of irregularly shaped grooves (depth ~ 0.08 nm). In Figure 6.8b, a part of the island is imaged with atomic resolution. A detailed inspection revealed that the atomic rows run almost unaffected through the grooves. Consequently, the grooves can not be interpreted as domain boundaries formed by islands of different orientations (see Figure 6.7c) joining together. Most probably, they may be induced by misfit related strain effect. The measured height of the (111) oriented Co oxide islands

Figure 6.7 (111) oriented Co oxide islands.

a) overview image,

b) atomic resolution image

STM (12×7) nm²,

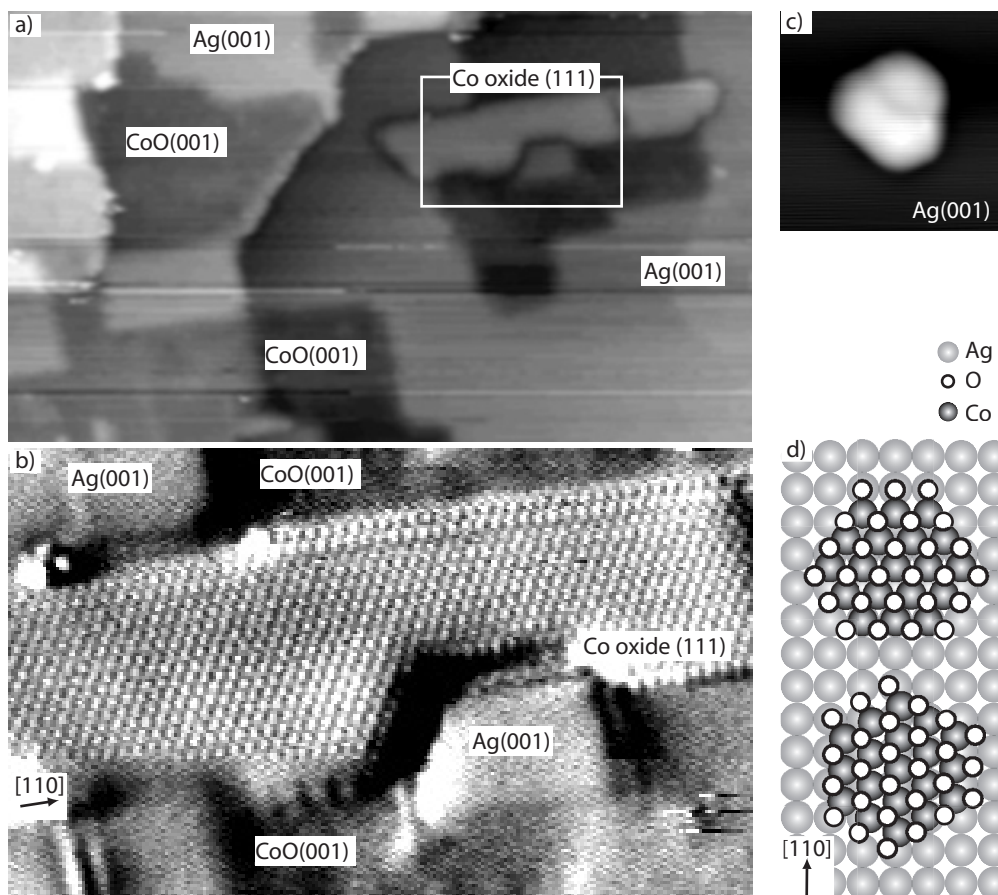
$U = -2$ V, $I = 0.1$ nA,

c) hexagonal Co oxide island

STM (6×6) nm²,

$U = -4$ V, $I = 0.1$ nA,

d) hard sphere model of (111) oriented domains on Ag(001).



(as shown in Figure 6.7a and Figure 6.8) with respect to the Ag substrate was never below 0.15 nm. Therefore, it was assumed that the (111) islands are at least 1 ML thick. However, it can not be excluded that the islands are embedded into the substrate similar to CoO(001) islands. The thickness of the (111) oriented islands may also amount two layers, therefore. On the other hand, the absence of a moiré pattern is explained more convincingly by a one-layer structure.

Figure 6.8 (111) oriented Co oxide islands.

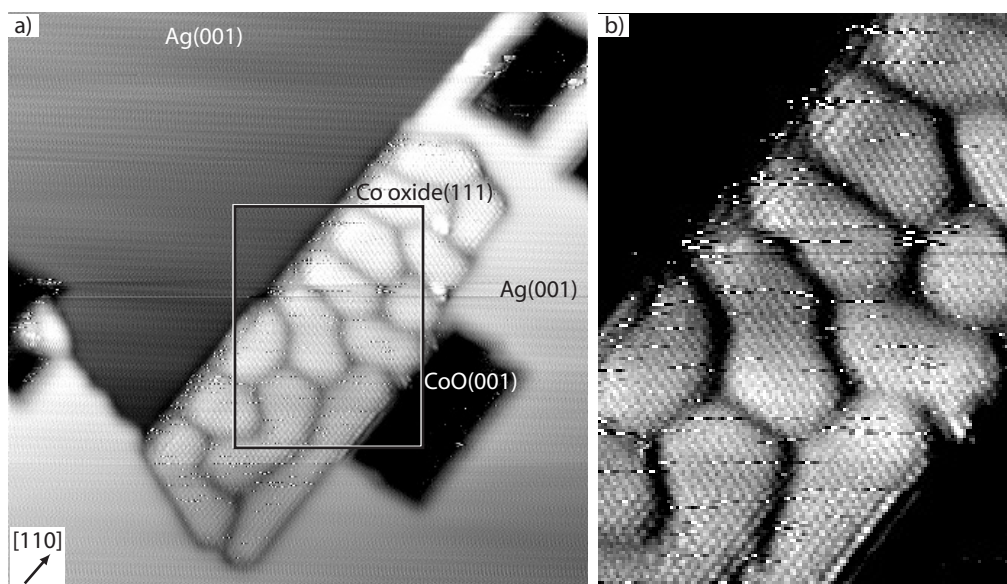
a) STM (28×28) nm²,

$U = -0.1$ V, $I = 0.1$ nA,

b) atomic resolution obtained for the rectangular area marked in Figure 6.8a,

STM (10×14) nm²,

$U = -0.1$ V, $I = 0.1$ nA.



There exist also thicker islands of a hexagonal structure. This is shown in Figure 6.9a. A relatively large island is seen displaying a hexagonal moiré pattern. Obviously, this island has been grown on top of a grooved (111) oriented Co oxide island together with a smaller one (island (i)). The moiré modulation has a periodicity of ~ 2 nm and a corrugation height of 0.07 nm. The height of the moiré island with respect to the grooved base layer is ~ 0.2 nm. In spite of numerous attempts, no atomic resolution on the moiré structure was achieved.

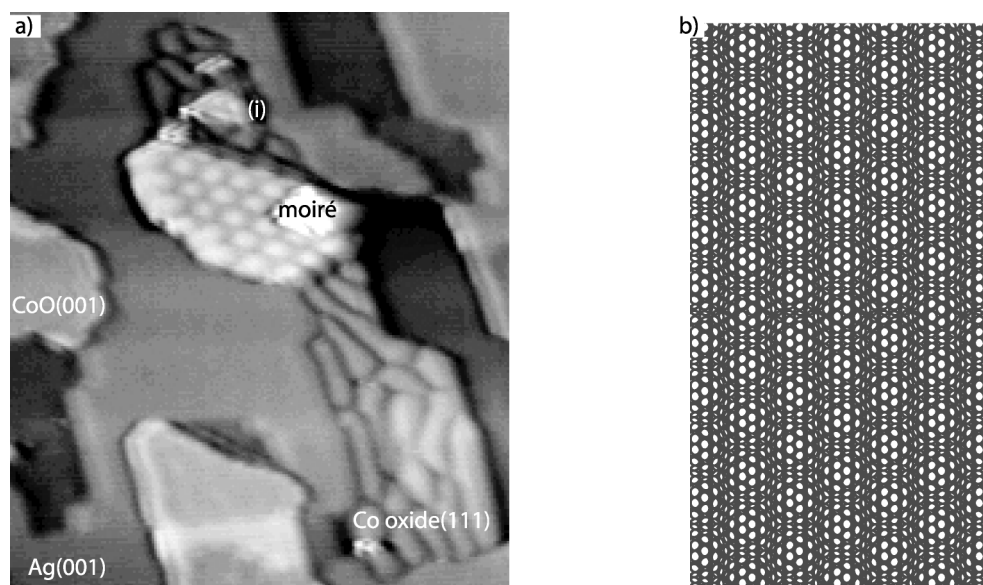
The formation of a hexagonal moiré pattern can be explained by two stacked hexagonal lattices having a slightly differing periodicity [27]. A model of the moiré pattern is presented in Figure 6.8b. Here, two hexagonal lattices with 5% mismatch are placed on top each other. Due to the misfit, the atoms of the upper lattice reside on different positions with regard to the base lattice which modulates the surface in a regular form and does not interrupt the atomic rows. Such moiré pattern has been observed for other systems too, e.g., for thicker Cu films on Ru(0001) [106].

It is noticeable that the (111) oriented oxide islands do not display a stripe structure as observed in other systems where (111) layers reside on top of (001) substrates. An example for that is the known Au(001) reconstruction [107]. There, the reconstructed hexagonal top layer is modulated by the (001) substrate in a stripe-like manner. Obviously, for the CoO/Ag system, the interaction between the oxide layers and the substrate is relatively weak. The latter has already been deduced from the “carpet” mode of growth observed for the CoO(001) layers on Ag(001) [22].

Figure 6.9 Moiré structure of (111) oxide islands.

a) STM (55×55) nm²,
 $U = -3$ V, $I = 0.1$ nA,

b) model of the moiré structure (two hex. lattices with mismatch of 5% are placed on top of each other).



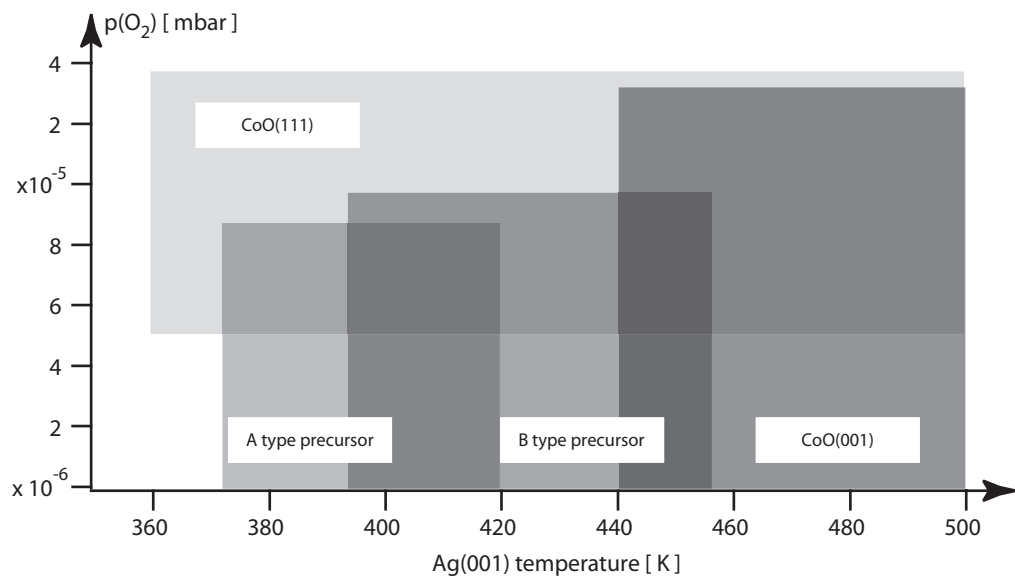
In a series of experiments, the conditions for the formation of the (111) oxide islands were studied. It was found that they can be grown at substrate temperatures around 420-450 K and an O₂ pressure of $\sim 2.0 \times 10^{-5}$ mbar which is distinctly higher than for the growth of (001) oriented CoO or CoO precursor islands. Further annealing in UHV (~ 470 K) led to the formation of moiré structures. At these conditions, they could be reproducibly obtained which allowed systematic STM/STS investigations. It was found that (111) oriented Co oxide

islands can be grown on Ag(001) simultaneously with CoO(001) islands [27]. For O_2 pressures $<5 \times 10^{-6}$ mbar, however, the probability to find (111) oriented islands was very low.

The question about the nature of the (111) oriented islands remains. It is known that a (111) oriented Co_3O_4 spinel-like surface layer can be formed if CoO(001) is exposed to $\sim 10^{-4}$ mbar of O_2 at temperatures around 620 K for several hours [110]. The Co_3O_4 spinel structure was also obtained by annealing a CoO powder under a flow of O_2 at 950 °C [42]. Voogt et al. [111] reported on the preparation of Fe_3O_4 films on a MgO(001) substrate. The oxide films were grown by depositing Fe from an effusion cell with simultaneous oxidation of the deposited Fe by a beam of NO_2 particles. The substrate temperature was set to 525 K. Anderson et al. [112] reported on the same system. They prepared Fe_3O_4 layers by depositing pure metallic Fe from an electron-beam evaporator on a MgO(001) substrate at 570 K. The chamber was filled at the same time with atomic O (pressure 2×10^{-5} mbar). Moreover, Chung et al. [113] have found that already at an O_2 pressure of 10^{-7} mbar hexagonal Fe_3O_4 films can be obtained if stainless steel was oxidized at 450 °C. Finally, Macuta et al. [37] reported that independent on preparation, the polished CoO(111) surface is covered by an epitaxial Co_3O_4 layer. Thus, the formation of the (111) oriented spinel structure is not an exceptional phenomenon and it is quite possible that the (111) oriented Co oxide islands observed in the present study possess a Co_3O_4 spinel structure, at least for the thicker films.

In summary, a phase diagram is finally drawn based on all results of the growth experiments of Co oxide films on Ag(001) (see Figure 6.10). The grey rectangulars represent the regions of preparation conditions where the different oxide species were found depending on O_2 pressure and temperature. An overlap of the squares indicates the range of the coexistence for several oxide phases.

Figure 6.10 Phase diagram of Co oxide formation.



6.4

Bias voltage dependent contrast

Oxide films are known to show a different contrast in STM imaging referred to the metallic substrate and depending on the applied bias voltage [31], [109]. It was shown that oxide islands can appear as a dark depression when the chosen bias voltage still lies inside the band gap of the film. At higher energies, they appear as bright protrusions. The apparent height of the islands may differ by 0.5 nm depending on the bias voltage. The contrast behaviour of Co oxide islands was previously investigated for CoO(001) bi-layers [31]. Due to the instability of RT STM, the measurements were restricted to the energy region between -3 V and 3 V. In the present work, a much higher stability was obtained at 100 K. Therefore, the voltage interval could be extended to ± 5 V. Islands possessing a thickness of 1-5 ML have been studied.

At first, the results of the contrast studies performed for CoO(001) islands are presented. The islands had a thickness of 2, 3, 4, and perhaps even 5 ML. The islands were located on top of the Ag(001) surface. In some cases, the base layer of the islands was embedded in the substrate. In the latter case, the geometric island height was reduced by 1 ML as visualized by the schemes of the islands in Figure 6.11a. For investigating the contrast behaviour of the islands, the apparent island heights (with respect to Ag(001)) were measured from the STM images in dependence on the bias voltage (see Figure 6.11a). The measurements, of course, provide the measured height and not the island thickness. For the measurement, a Pt-Ir tip was used (the same results were obtained with W tips). For all island thicknesses, similar shapes of the curves were found. The curves are only displaced along the height axis corresponding to the island heights. In a hatched form, the curve for completely embedded 2 ML islands was anticipated by displacing the curve found for the partly embedded islands. However, in the STM images never such contrast behaviour was measured. Consequently, it can be concluded, that completely embedded 2 ML CoO(001) islands do not exist.

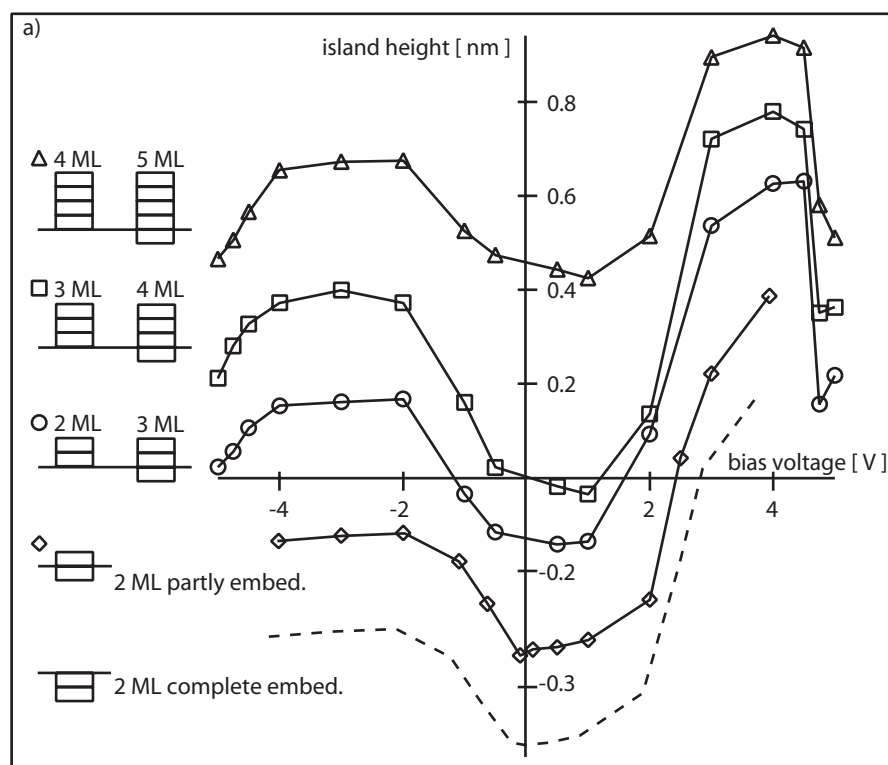
In the case of the bi-layer islands (on top and embedded), the results are in agreement with previous studies. In particular, a characteristic contrast reversal was found where the islands appear as depressions (negative apparent island height) [31]. In the present measurements, not only for 2 ML, but also for 3 ML and 4 ML thick islands a contrast reversal was found at a small bias voltages. At these voltages, the electrons tunnel through the insulator gap of the oxide island. Therefore, the electrons have to tunnel not only through the vacuum gap, but also through the insulator gap. Consequently, the barrier width is increased and the tunneling current is reduced. For keeping the tunneling current constant as required in CCT imaging, the tip moves closer to the surface. If the tip reaches the island edge during scanning, the oxide gap is no longer present and the current drastically increases. Therefore, the tip will be retracted for keeping the current constant which explains the contrast reversal [31]. In the energy region of 3-4 V, the electrons tunnel into the conductance band and the oxide island behave like a metal. Consequently, the apparent island height approximately equals the geometric one. Similar relations are found for negative bias voltages where the electrons tunnel from the oxide valence band into the unoccupied tip states. Beyond -4 V and above 4 V, however, an unexpected drop of the apparent island

heights was observed. In the case of positive voltage, a drastic decrease by ~ 0.5 nm was detected within a bias interval of 0.3-0.4 V. On the negative side, the same effect occurred, but the decrease was not so pronounced.

Figure 6.11

a) apparent islands height vs. tunneling voltage measured with a Pt-Ir tip for 2, 3 and 4 ML thick CoO(001) islands.

b) contrast reversal obtained for CoO(001) 2 ML island.



The reason for that can be attributed to the first field resonance state which was measured by STS for Ag(001) at ~ 4.6 V as already described in Chapter 5.1.2. Due to the field resonance, a strong increase of the tunneling current on Ag takes place when the bias voltage reaches the first resonance energy. For keeping the current constant, the tip is correspondingly retracted by the regulation system. If the tip moves now over an CoO island, no field resonance is present and the current suddenly drops down. As a consequence, the tip is moved again towards the surface for keeping the current constant. Correspondingly, for bias voltages shortly below the energy of the field resonance, the largest apparent island height is measured. A similar situation is found for the negative bias voltages. The field resonances, however, are here not so pronounced (see Chapter 5.1.2). Thus, smaller changes of the apparent height arise in that range of bias voltages.

In the following, the behaviour of the precursor islands is considered. Many attempts to find the best imaging conditions finally resulted in reliable bias voltage dependent data for the A and B type precursors. It was found that the precursors also display a bias dependent contrast reversal. This is illustrated by the STM images in Figure 6.12. An arrow marks the same location on the surface (just for better orientation on the drifting sample). For bias voltages between -3V and 1V, the B type precursors, as marked in Figure 6.12, appear depressed. For bias voltages >1 V, however, they appear as protrusions. For bias voltages between -3 V and 2.8 V, the A type precursor islands appear also depressed. For bias voltages <2.8 V, however, the characteristic stripe-like superstructure of the

A type precursor (see Chapter 6.1) is imaged as a protrusion with respect to Ag(001). Hence, not only the stripe-like superstructure distinguished precursor of A type from B type, but also the different contrast behaviour.

Figure 6.12 Bias voltage dependent measurements of A and B precursors.

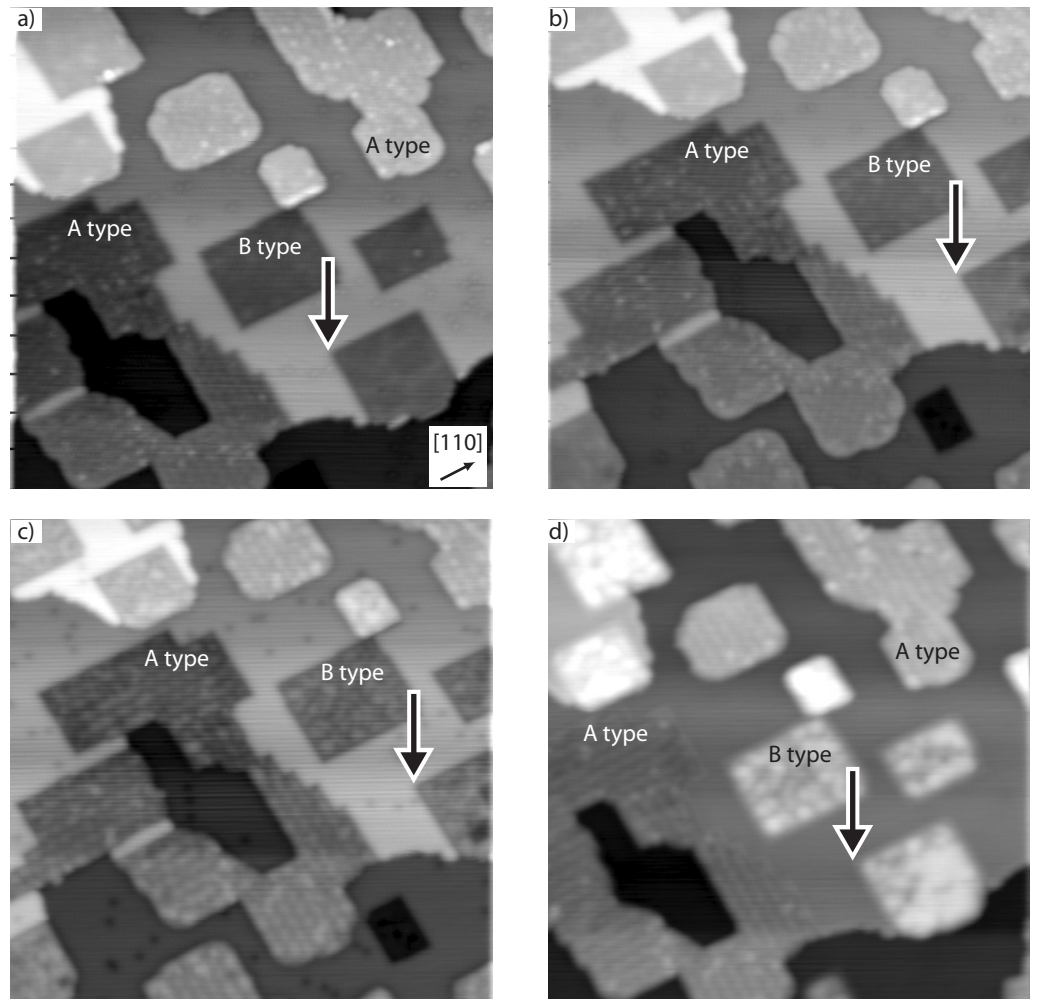
STMs (50×50) nm²,

a) $U = -3$ V, $I = 0.1$ nA,

b) $U = -1$ V, $I = 0.1$ nA,

c) $U = 1$ V, $I = 0.1$ nA,

d) $U = 3$ V, $I = 0.1$ nA.

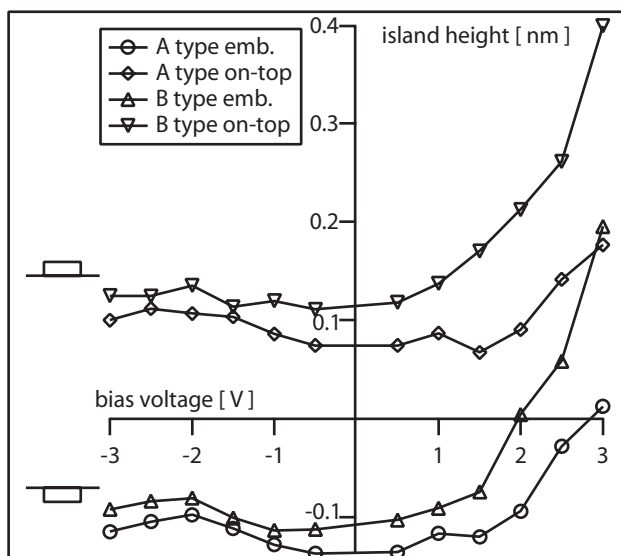


The apparent island heights of the A and B type precursors deduced from the STM images are drawn in Figure 6.13 in dependence on the bias voltage. For each precursor type, two characteristic bias voltage dependencies were found. In one case, negative island heights were partly measured. In the other case, the curves indicate positive values for all bias voltages. As both curve pairs are displaced just by the monolayer height (0.2 nm) it is assumed that the precursors exist on Ag(001) both on top and embedded. Different to the embedded precursors, the on top residing precursor islands do not display a contrast reversal.

Comparing the contrast behaviour of the precursors with that of the CoO(001) islands, the strong differences are striking. This indicates that the electronic structures of the precursors are still different from that of CoO(001). Absence of a distinct minimum in island heights indicates that a band gap has not yet developed clearly and the precursor are not yet fully insulating.

Figure 6.13 Islands height vs. tunneling voltage for A and B precursors.

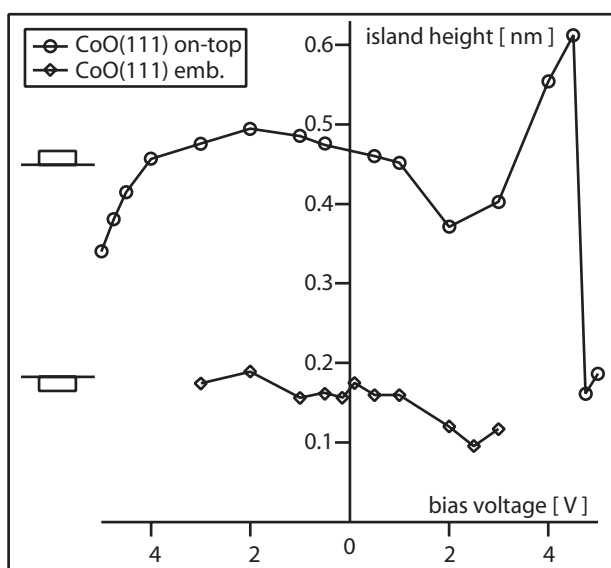
Curves are drawn for embedded and on-top 1ML thick islands.



Finally, the (111) oriented oxide islands are analysed. The investigations were focused on the grooved (111) islands. Figure 6.14 shows the apparent island height vs. the bias voltage. Only positive step heights were measured and no contrast reversal was observed. The grooved islands displayed two different heights differing again by about the monolayer height of Ag. Therefore, it was assumed that the grooved (111) islands exist on Ag(001) similar as (001) islands on top and embedded. In contrast to the CoO(001) islands, there is no

Figure 6.14 Islands height vs. tunneling voltage for CoO(111) islands.

Curves are drawn for embedded and on-top 1ML thick islands.



pronounced height reduction at lower energies. Therefore, one can assume that the (111) islands display a more metal-like behaviour. In addition, some influences of the Ag(001) surface are obvious. Most striking is the strong drop of the apparent island height measured at 4.5 V. It can be explained by the presence of the first FER of Ag(001) similar as in the case of the CoO(001) islands. In addition, there is a characteristic decrease of the step height between 1 V and 2 V. At these voltages, surface and bulk states of

Ag(001) are present (see Chapter 5.1). Therefore, the tunneling current is increased on Ag(001) (as in the case of FER of Ag(001), but not so pronounced) and a corresponding island height reduction is observed.

6.5

Scanning tunneling spectroscopy

The first step towards an investigation of the electronic structure of CoO(001) was already done by analysing the island contrast behaviour. The different contrasts observed should be correlated with the corresponding electronic structure of the different islands. Systematic STS measurements were performed in order to characterise the electronic structures of all Co oxide island types observed.

The electronic structure of CoO has been studied experimentally [41] as well as theoretically [120]. However, such techniques like XPS [117]-[118] provide only an integral information on the surface and are only suited for valence band studies. Some investigations exist where XPS and BIS were combined in order to obtain a full information on the band structure of transition metal oxides like CoO and Co₃O₄ [42], [110], [121].

It is clear that STS is much more sensitive to local variations of the electronic structure. Due to the high lateral resolution, it can be used for a characterisation of the electronic structure of insulating films even in the submonolayer range where other techniques like photoemission spectroscopy are not sensitive enough or are not able to distinguish between the various kinds of islands [113]-[60].

6.5.1 $I(U)$ spectroscopy

CoO(001) and (111) oriented Co oxide

The STS maps were taken according to the procedure described in Chapter 4.4. The surface area where the $I(U)$ characteristics were acquired is presented in Figure 6.15a. Different Co oxide islands are present on the Ag(001) substrate. Islands with more rounded shape correspond to CoO(001) (minimum thickness 2 ML) and islands with a hexagonal shape correspond to (111) oriented Co oxide. The different grey levels indicate different island thicknesses.

The measured $I(U)$ characteristics of Ag(001), CoO(001), and CoO(111) are presented in Figure 6.15b. They were taken by stabilising the tip over the corresponding part of the surface with a bias voltage of -3.5 V and a tunneling current of 0.1 nA. Then, a voltage ramp from -3.5 V to 3.5 V was applied. For negative biases (tunneling from occupied states of the sample into the tip), the general slope of the individual curves is almost the same. Only over the clean Ag surface, the decrease of I with increasing U (towards $U=0$ V) is somewhat more pronounced than that on the oxide species (hardly visible in Figure 6.15b). For positive voltages (corresponding to tunneling from the tip into the empty states of the sample), the differences of the $I(U)$ dependency became more obvious. Particularly striking is the extremely strong increase of the tunneling current above 2.3 V for CoO(001).

For positive stabilization voltage (Figure 6.15c), the $I(U)$ characteristics of the various surface structures are clearly different. For $U=3.5$ V, all curves reach the stabilization current of 0.8 nA. For Ag, I rises already above $U=0$ V toward larger values of U , while for CoO(001) and CoO(111), an essential tunneling current is only observed above $U=2.5$ V. For negative biases, the situation is quantitatively the same. The similarity of the $I(U)$ curves of both CoO(001) and CoO(111) as well as their difference to metallic Ag(001) indicate that also CoO(111) has already developed some oxidic behaviour.

The differences of the $I(U)$ characteristics allow the plot of current images, where the different surface structures could be identified in a unique way (see Figure 6.16b-f).

Figure 6.15 STS experiment.

a) CCT overview

STM (40×40) nm²,
 $U = -3.5$ V, $I = 0.1$ nA,

b) $I(U)$ characteristics

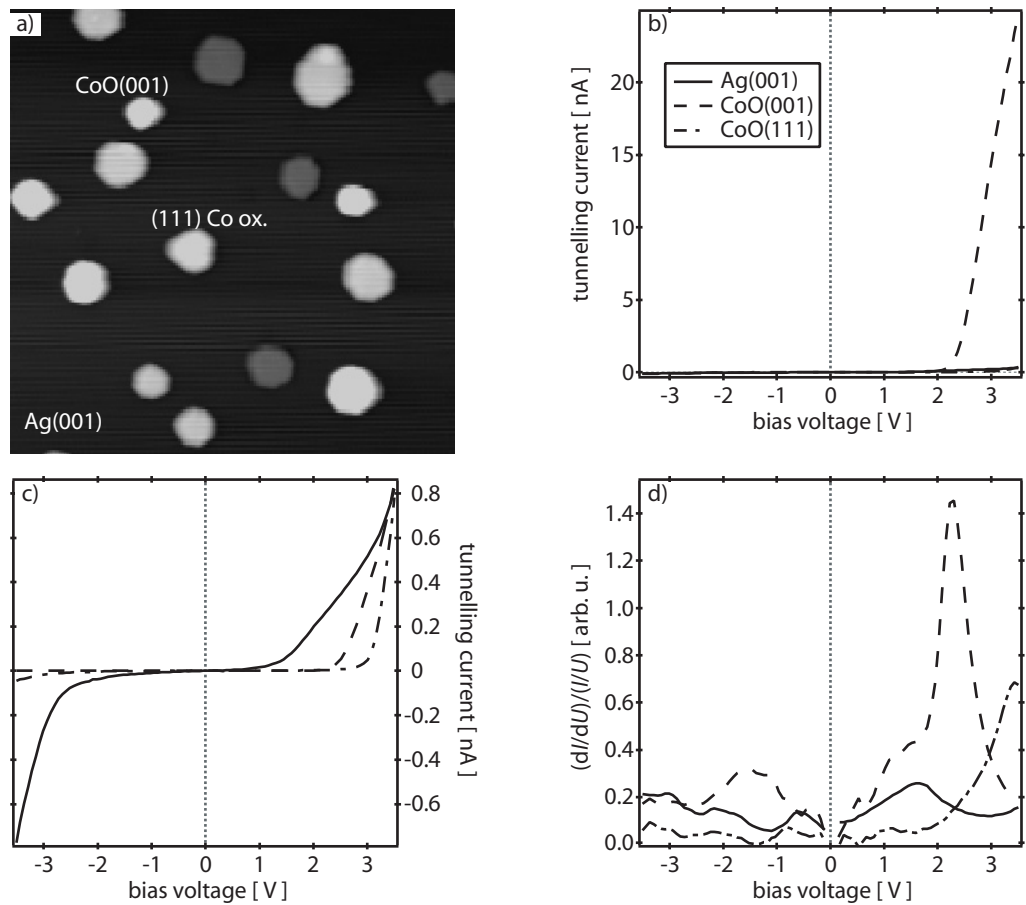
stabil. at $I=0.1$ nA $U = -3.5$ V,

c) $I(U)$ characteristics taken

over surface in a)

stabil. at $I=0.8$ nA $U = 3.5$ V,

d) $(dI/dU)/(I/U)$ data obtained from spectra presented in b).



In Figure 6.15d, the normalized tunneling conductivity $(dI/dU)/(I/U)$ derived from the $I(U)$ data in Figure 6.15b is presented. The measurement with the negative stabilization voltage was considered because of the relatively low noise level. As already shown in [27], an approximate density of states can be derived from the normalized differential conductance. Experiments with other voltage amplitudes (± 2 V up to ± 6 V) qualitatively yield the same structures. Changing the polarity of the stabilization voltage mainly affects the intensity of all features, but not their general shape or their position on the voltage scale.

The Ag(001) related characteristic was already described in Chapter 5.1. It was used as a spectroscopic fingerprint to discriminate Ag islands from oxide islands at higher coverages.

For the CoO(001) islands, a strong maximum at 2.2 V was found which corresponds to the increase of the tunneling current in the $I(U)$ curve of Figure 6.15b. A smaller maximum is visible at -1.6 V and corresponds to the occupied states. The energetic positions of these structures coincide with the voltage dependent contrast reversal in the STM images of CoO(001) (see Figure 6.11). According to Viernow et al. [60], pronounced peaks in the $(dI/dU)/(I/U)$ can be explained by a divergence of $(dI/dU)/(I/U)$ at the band edge. It has been pointed out that the $(dI/dU)/(I/U)$ spectra of bulk semiconductors diverge at the conduction band minimum [124]. The current approaches the zero value faster than the differential conductance (dI/dU) when approaching the conduction band edge from above. Inside the gap, $(dI/dU)/(I/U)$ is undefined because $I=0$. However, for thin insulating films, the tunneling current remains finite inside the band gap due to tunneling through the oxide into the substrate states. Nevertheless, the measured current and consequently the calculated conductance are almost below the noise level. Consequently, their ratio is extremely noisy and undefined. Thus, the two maxima observed in $(dI/dU)/(I/U)$ could approximately be assigned to the band gap edges. The shoulder between 1V and 1.8 V was reproducibly observed. Since the shoulder was also observed for thicker CoO(001) islands and was not observed for precursors, it could be explained by tunneling into the states near the conduction band minimum.

For CoO(111) islands, no distinct maxima were observed in the $(dI/dU)/(I/U)$ spectrum within the investigated voltage range. Only a weak peak at 1 V is visible in Figure 6.15d. It can not be correlated to a spectroscopic feature of the Ag(001) substrate. Also no pronounced changes of the contrast with the bias voltage were detected for (111) oriented islands in the STM images (Figure 6.14). Thus, one can conclude that the (111) oriented oxide does not exhibit an extended band gap in contrast to CoO(001).

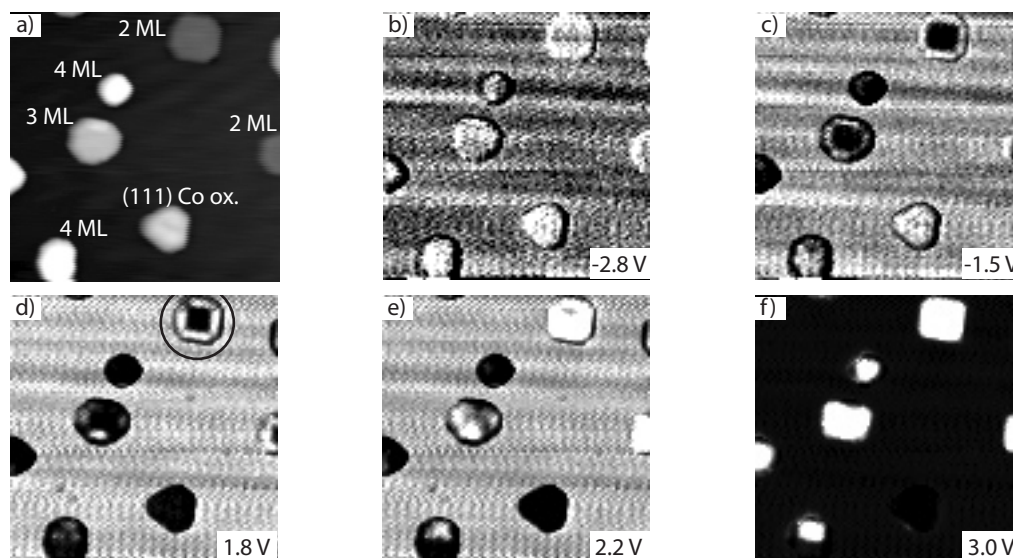
In Figure 6.16, the current images are shown together with the topographic image. The latter (Figure 6.16a) represents the same area as shown in Figure 6.15a. The topographic height of the islands is indicated. 2, 3 and 4 monolayer thick CoO(001) islands are present as well as a hexagonal Co oxide island. The island heights were measured at -3.5 V and conclusions on the layer thickness were made by using the specific contrast dependence of the height shown in Figure 6.11. The current images (Figure 6.16b-f) represent the spatial distribution of the tunneling current for the applied bias voltage. In the current image of Figure 6.16b taken at -2.8 V, the islands appear slightly protruded and both flat and homogeneous as in the topographic image. At -1.5 V and 1.8 V bias voltage, the island appear partly as depressions. For the 2 ML and 3 ML islands, new structures are seen at the edges. At 2.2 V, these islands appear again as protrusion. At higher voltages, the maximum tunneling current is found on the CoO islands which appear bright in comparison to Ag (Figure 6.15f).

An intensity effect is seen at the edges of the islands. Fringe-like structures are found at -1.5 and 1.8 V. In Figure 6.16d, the island marked with a circle has a dark centre and a broad bright rim (corresponding to a higher current).

Figure 6.16 Spatial distribution of tunneling current for area in a).

a) STM (25×25) nm²,
 $U = -3.5$ V, $I = 0.1$ nA

b)-f) current maps taken
with voltages noted in bot-
tom right corner.

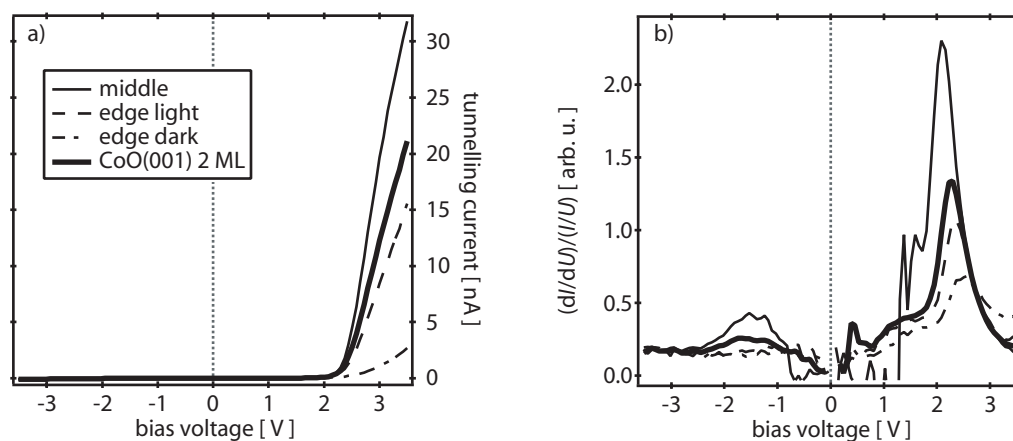


In addition, there is a dark narrow border at the island edge (corresponding to a lower current). These edge effects are characterised in more detail in Figure 6.17a where the corresponding STS data are presented. The $I(U)$ characteristics extracted from the different parts of the islands (middle and both edge areas) are shown. As one can see, the highest current corresponds to the centre of the island and a smaller current was obtained on the narrow dark fringe. The edge irregularities influence the total spectrum. The $I(U)$ spectrum averaged over the entire island (bold curve) has a lower intensity than that obtained from the inner part of the island.

Figure 6.17 STS data of 2 ML CoO(001) island considering the edge effect.

a) $I(U)$ curves,

b) $(dI/dU)/(I/U)$ calculated
from a).



Also in the $(dI/dU)/(I/U)$ curves differences are obvious. The curve measured for the island centre has the strongest peak at ~ 2 V whereas the corresponding peaks of the edges reveal small shifts towards higher energies. Moreover, the peak height is at least by factor of two smaller than for the island centre. This effect, of course, may distort the STS characterisation of the islands. Better results can be obtained by measurement of larger islands where the influence of the edges is reduced. Interesting is the voltage dependence of the noise level of the spectrum taken on the centre of the island. In the gap range of CoO, i.e., at bias voltages

from -0.8 V to 1.8 V, the noise is more intense than the signal. This is a clear indication of the insulating behaviour of the film. However, the electronic structure of the edges can not be determined accurately.

Another interesting aspect is that the most pronounced edge effect was observed for the 2 ML CoO(001) islands. This could be judged from Figure 6.16d where it is obvious that for the 3 ML thick islands the edge effect is much weaker. The general dependence of the STS data on the film thickness should be therefore re-examined. In Figure 6.18a and b, the $I(U)$ characteristics and the corresponding $(dI/dU)/(I/U)$ curves are presented for CoO(001) islands possessing a thickness of 2, 3 and 4 ML. Already in the current curves it is possible to distinguish between those islands. The thicker the islands are, the lower is the tunneling current for positive U . Despite the different slopes of the $I(U)$ characteristics in Figure 6.18a, no pronounced differences are found in the $(dI/dU)/(I/U)$ curves (see Figure 6.18b). Peaks between 2 V and 3 V display only small shifts (of ~ 0.1 V) towards higher energies for thicker islands. This behaviour can be easily explained in a qualitative manner by regarding the schemes shown in Figure 6.18c. There, a metal/vacuum/oxide/metal tunneling junction is drawn for films possessing a thickness of 2, 3 and 4 ML. E_F indicates the position of the Fermi level of tip (T) and sample (S). E_{VBM} and E_{CBM} are the energies of the valence band maxima and the conduction band minima, respectively. z_{tunnel} is the vacuum separation between tip and sample and d_{oxide} is the CoO(001) film thickness. It is assumed that the voltage applied between tip and sample does not drop completely in vacuum. Thus, taking into account the dielectric constant of CoO ($\epsilon = 20$), each additional oxide layer should reduce the applied bias voltage by a certain amount which for the first layer is in the order of $U/20$ V. Increasing the film thickness will for constant tunneling current decrease the sample/tip separation. As a consequence, the potential drop in the sample will increase and each layer would induce a peak shift towards higher energies in the $(dI/dU)/(I/U)$ spectra as observed in Figure 6.18b. In the present experiment, z_{tunnel} is unknown and the model allows only a qualitative discussion.

In Figure 6.18b, a somewhat smaller maximum at -1.5 V also remains constant. Only the noise level between -1 V and 1 V slightly rises with the islands thickness. Therefore, the peak at -1.5 V corresponds to specific properties of CoO(001). At the same time, the shoulder between 1 V and 2 V became weaker with increasing film thickness.

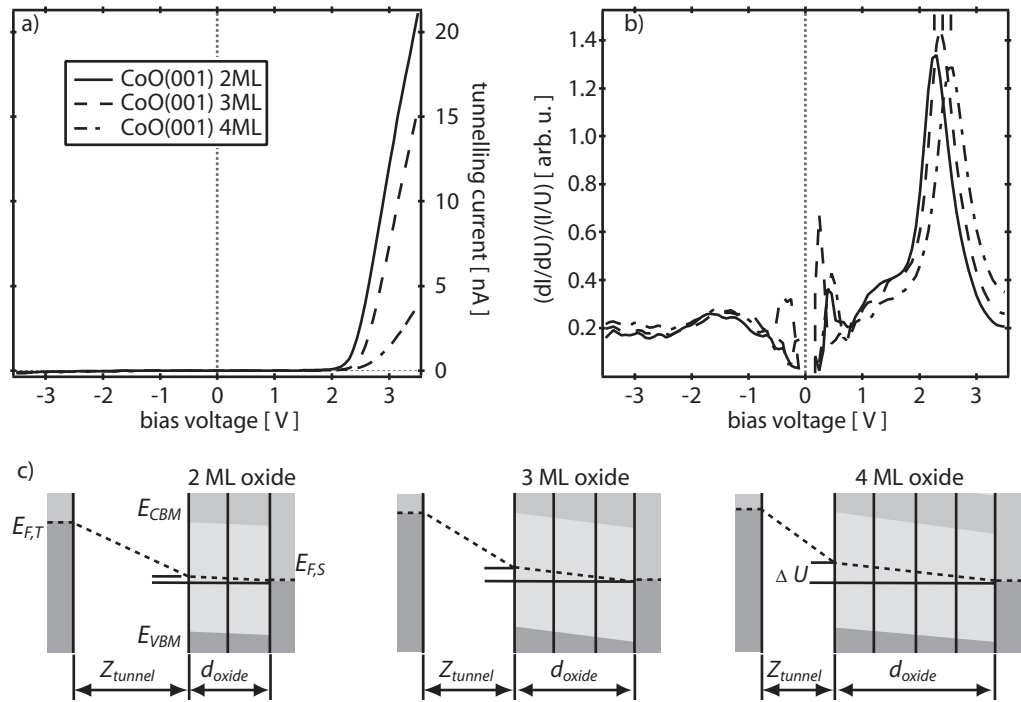
Qualitatively, the shape of $I(U)$ curves in Figure 6.18a can be explained by the model which is sketched in Figure 6.19. A metal/vacuum/oxide/metal tunneling junction is schematically drawn to describe the $I(U)$ spectroscopic experiment. Here, z_{tunnel} is kept constant. The film thickness d_{oxide} is also assumed to be constant. ϕ indicates the work function of the corresponding part of the junction (T - for tip (4.5 eV); S - for substrate (4.6 eV); O - for oxide (3.8 eV)). The key idea is that a tunneling across two barriers occurs. First, the electrons tunnel across the vacuum gap and then through the insulator film as sketched in Figure 6.19a. According to Viernow et al. [60], the transmission probability $T(E, U)$ for tunneling electrons (those with energy E close to the Fermi level) can be described by two terms $T(E, U) = T_{vac}(E, U)T_{ins}(E, U)$, i.e., the transition probabilities for the vacuum barrier $T_{vac}(E, U)$ and for the insulator film $T_{ins}(E, U)$.

Figure 6.18 STS data measured for different CoO(001) thicknesses.

a) $I(U)$ curves, $U_0 = -3.5$ V, $I_0 = 0.1$ nA,

b) $(dI/dU)/(I/U)$ data obtained from a),

c) models of the tunnel contact with the presence of an insulator layer of different thicknesses.



The barrier which the tunneling electrons have to overcome is drawn in Figure 6.19a as crosshatched region including the vacuum separation and the insulating film. The situation is qualitatively changed when the energy of the tunneling electrons equals the conduction band minimum ($E > E_{CBM}$) as depicted in Figure 6.19b). In this case, the oxide film is no longer a barrier in the tunneling process ($T_{ins}(E, U) = 1$) which leads to a drastic enhancement of the transmission probability. Correspondingly, a rapid rise of the current in the $I(U)$ characteristics is measured (see e.g., Figure 6.18a). In other words, the critical voltage at which the drastic changes in the transmission probability occur (conduction band edge) approximately corresponds to the peak at positive voltages of the $(dI/dU)/(I/U)$ spectra (see e.g., Figure 6.18b) [60].

Almost the same should happen if one considers tunneling into the unoccupied tip states. When the bias voltage is slightly lower than valence band maximum, the electrons tunnel from Ag(001) through the band gap of oxide as drawn in Figure 6.19c and have to overcome the tunneling barrier. At this bias voltage the barrier is composed by both the vacuum and the oxide barrier. Consequently, the tunneling current small. At the valence band edge, the situation changes again and, as illustrated in Figure 6.19d, the electrons tunnel from the occupied oxide states into unoccupied tip states. In this case, the tunneling electrons travel only through the vacuum separation and the additional barrier caused by the insulating film is bypassed. The current increase produces a peak at -1.5 V in the $(dI/dU)/(I/U)$ curve (Figure 6.18b) which approximately corresponds to the position of the valence band edge.

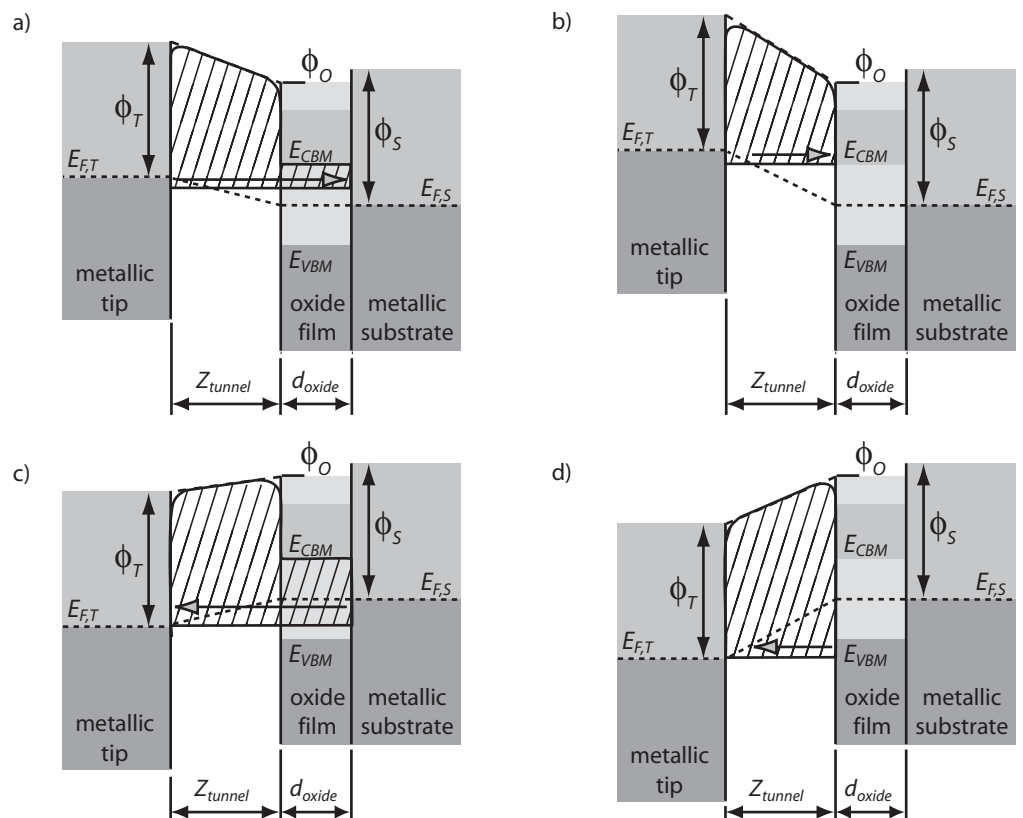
Figure 6.19 Metal/vacuum/oxide/metal tunneling junction.

a) positive bias (tunneling into unoccupied Ag(001) states through oxide),

b) positive bias (tunneling into unoccupied oxide states),

c) negative bias (tunneling from occupied Ag(001) states),

d) negative bias (tunneling from occupied oxide states).



One problem is the strong difference of both peak intensities in the $(dI/dU)/(I/U)$ curves. This problem can be solved by comparing Figure 6.19b and d. In both cases, tunneling only occurs through the vacuum barrier. Thus, only the vacuum barrier should be taken into account. In $I(U)$ STS, the barrier width remains constant. However, the effective barrier height is different. For positive bias voltages (tunneling from tip into oxide), the average barrier height appears to be lower in comparison to negative bias (tunneling from oxide). This can easily be seen by comparing Figure 6.19b and d. Thus, the transmission probability which in this case consists only of the $T_{vac}(E,U)$ term, will depend in a specific way on the barrier parameters (i.e., barrier height) [57], [65]. Detailed theoretical calculations and simulations are certainly needed to understand the behaviour of the tunneling current as function of the bias more quantitatively. It is, for example, very difficult to separate the DOS effects from the effect induced by the strongly varying transmission probability in the analysis of the $(dI/dU)/(I/U)$ spectra.

In addition, one has to consider possible effects by resonant tunneling (within the oxide layer) and FER (in the vacuum gap). Resonances within the oxide film can be neglected due to the small film thickness [78]. The FER, on the other hand, appear at higher energies and can therefore be separated from those related to the DOS. This will be shown below when the results on Mn oxide are described (Chapter 7.2.3).

In Figure 6.20a, a series of $(dI/dU)/(I/U)$ spectra is presented for CoO(001) islands of different thickness as well as for grooved (111) oriented Co oxide islands. For each island type, several islands were analysed (see individual curves).

Almost all spectra were taken within a voltage range of ± 5 V. The spectra demonstrate the independence from the stabilization conditions (different stabilization voltages correspond to different vacuum separations). All characteristic peaks of CoO(001) have the same positions.

There are several other important details which are seen here. A second peak was observed in the $(dI/dU)/(I/U)$ spectra noted as (2) in Figure 6.20a. It was detected for all kind of islands and thought to be related to the first resonance state as shown in Figure 6.20b. There, the first peak is already explained by electron tunneling from the tip into the conduction band minimum. The second peak is possibly related to an electron standing wave formed between the oxide surface and the tip. This is, however, not the only possible explanation. It could also be some kind of oxide surface interband transitions as discussed in [123]. This would be in line with the intensity of the second peak which is lower in comparison to the first peak (see peak (1) in Figure 6.20a).

The noise in all spectra was not smoothed out in order to demonstrate the difference between CoO(001) and (111) oriented islands. It is obvious that the noise level at low bias voltages (i.e., within the gap region) is much lower for the (111) Co oxide and is restricted to the range between -0.5 V and 0.5 V. For CoO(001), the noise region extends from -1 V to 1 V. These results suggest that the band gap is much smaller for (111) Co oxide in comparison to CoO(001) islands. Thus, one can conclude that there is no extended band gap for (111) oriented islands. This is also in a good agreement with [42] where CoO and Co₃O₄ were studied by means of XPS and BIS yielding a band gap of less than 1 eV for spinel Co₃O₄. Similar results were also obtained for FeO, Fe₂O₃ and Fe₃O₄ by means of STS [113], [122]. Thus, for FeO, a band gap of 2.4 eV was found and one of 2 eV for Fe₂O₃. In contrast, the spinel Fe₃O₄ displayed a metallic behaviour corresponding to a vanishing band gap. Hence, the assumption made above that the (111) oriented Co oxide islands are related to spinel Co₃O₄ is corroborated by the STS results. As consequence, one has to attribute the peaks at 3.8 V and at 4.5 V to field emission resonances and not to the band structure.

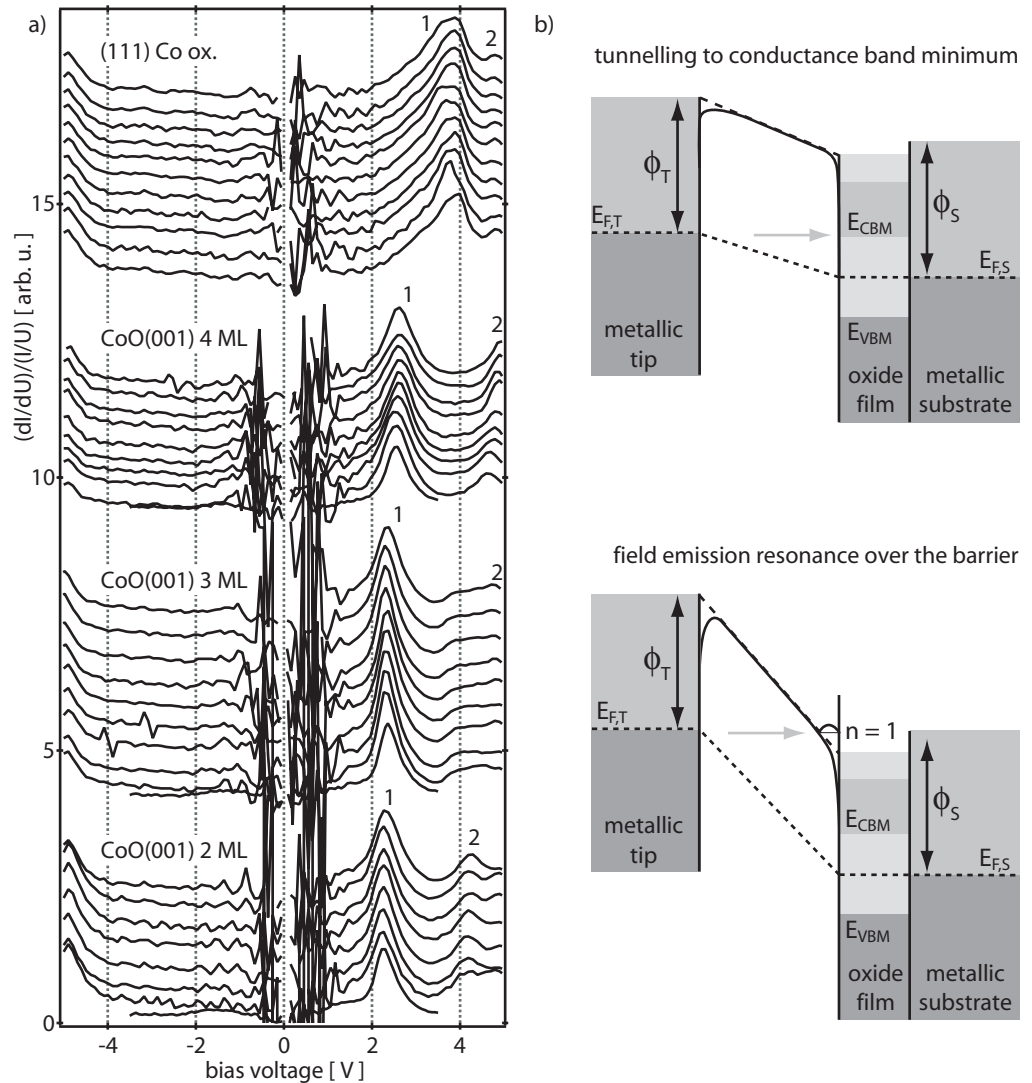
In Figure 6.21a a sample is imaged where the CoO(001) islands as well as the grooved and the moiré (111) Co oxide islands are present together with clean Ag(001). In addition, there exists a small Co oxide island (i) on top of the grooved one. Figure 6.21b represents the tunneling current map taken at 3 V for the area marked in Figure 6.21a. The corresponding $I(U)$ spectra and the $(dI/dU)/(I/U)$ data for the Ag(001) and the (111) oriented Co oxide islands are shown in Figure 6.21c and d, respectively. Results from CoO(001) islands are not included since they are already described above. Due to the high stability, STS were performed with high reproducibility.

In the current map, one is able to see small dark points (arrow) which correspond to O atoms on Ag(001) as was described previously (Chapter 5.2). All types of (111) oriented islands display a contrast reversal in the current map (3 V) and remain dark (i.e., they are areas of low tunneling current).

Figure 6.20

a) normalized tunneling conductance spectra for CoO(001) islands of different thickness and for grooved Co oxide (111) islands,

b) sketch of a metal/vacuum/oxide/metal tunneling junction explaining the $(dI/dU)/(I/U)$ data.



In Figure 6.21c, the $I(U)$ characteristics for the (111) Co oxide islands are drawn together with that of Ag(001). There is a clear difference between the oxide curves and that of Ag. But there are also differences between the curves of the grooved islands and the moiré. These differences become more visible in the $(dI/dU)/(I/U)$ curves as illustrated in Figure 6.21d. The sharp resonance peak of Ag(001) at 4.5 V is resolved and also sharp peaks for the grooved (111) Co oxide island (peak at 3.9 V) and for the moiré (111) island (peak at 3 V). For the small island (i) developed on the grooved island, it becomes obvious that it displays the same features as that of the moiré island. Obviously, island (i) is also a moiré-like island, but it is too small for displaying the hexagonal moiré pattern. All peaks of the oxide islands have the same shape and almost the same intensity compare to Ag(001). This suggest that they have a resonance origin, too. Only a small maximum at 1 V may be related to DOS effects. From the similarities in the $(dI/dU)/(I/U)$ spectra one can conclude that the (111) islands display a more metallic behaviour despite their assumed relation to the spinel structure of Co_3O_4 .

Figure 6.21 (111) oriented islands on Ag(001).

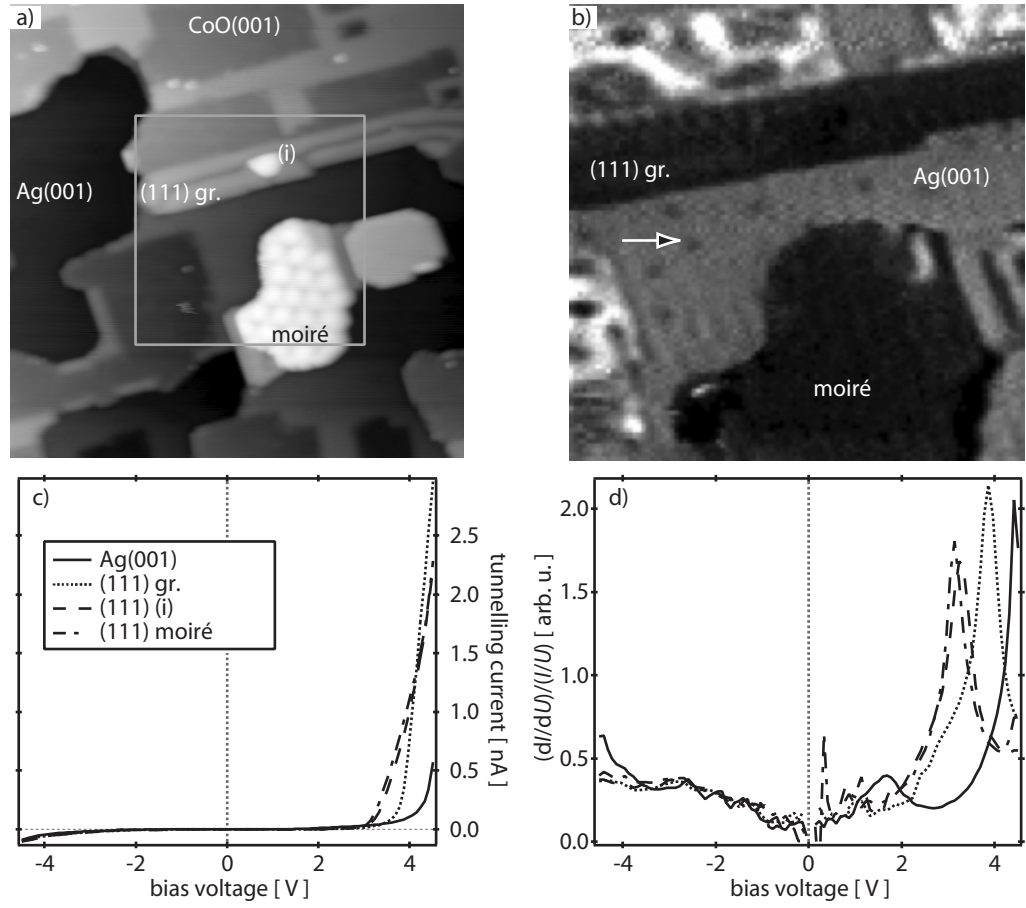
a) grooved ((111) gr.) and moiré islands:

STM (50×50) nm²,
 $U = -3$ V, $I = 0.1$ nA

b) tunneling current map at bias voltage of 3 V, corresponds to the area marked in a),

c) $I(U)$ curves, $U_0 = -4.5$ V, $I_0 = 0.1$ nA,

d) $(dI/dU)/(I/U)$ spectra calculated from c).



6.5.2 $I(z)$ spectroscopy of CoO(001), (111) Co oxide and Ag(001)

The logarithmic dependence of the tunneling current with respect to the sample distance can be used to determine the work function or the tunneling barrier height [65]. Experimentally, this quantity can be measured by varying the tip/sample distance by the z piezo settings. The measured value often varies with the distance and is defined as the apparent barrier height. Thus, one can use the $I(z)$ spectroscopy as described in chapter 3.3 to determine these values and characterise the sample.

In Figure 6.22, the results of two experiments are shown. The STM image in Figure 6.22a represents the surface where the $I(z)$ characteristics were acquired. (001) and (111) oriented islands are present on the surface. The STM images were taken at $U = -3$ V (Figure 6.22a) and $U = 3$ V (Figure 6.22c). They demonstrate again the contrast reversal of CoO(001) with respect to the surrounding Ag(001) and to the (111) oriented Co oxide. After the tunneling tip was stabilized at -3 V or at 3 V, the feedback was switched off and a z ramp of 0.2 nm towards the surface was made. Simultaneously, the tunneling current was recorded. The spatial distribution of the tunneling current at 0.2 nm away from the stabilization point towards the surface is presented for stabilization voltages of -3 V (Figure 6.22b) and 3 V (Figure 6.22d). The $I(z)$ characteristics are also included for stabilization at -3 V (Figure 6.22e) and for stabilization at 3 V (Figure 6.22f). Comparing the STM and current images (Figure 6.22a and

b), one can conclude that at -3 V CoO(001) islands appear in the STM image as a dark depression whereas in the current image they look like protrusions with respect to Ag(001). The reverse situation was observed for 3 V stabilisation. Here, the bright protrusions of CoO(001) imaged in STM (Figure 6.22c) appear as depressions in the current map (Figure 6.22d). The $I(z)$ spectra of (e) and (f) once again demonstrate the difference between CoO(001) and Ag(001). The (111) oriented island provides the highest current independent from the stabilization voltage. The apparent barrier heights were numerically calculated from the $I(z)$ spectra according to equation (3.16).

Figure 6.22 STM/ STS measurements of CoO(001) and (111) islands on Ag(001).

a) STM (50×50) nm²,
 $U = -3$ V, $I = 0.1$ nA,

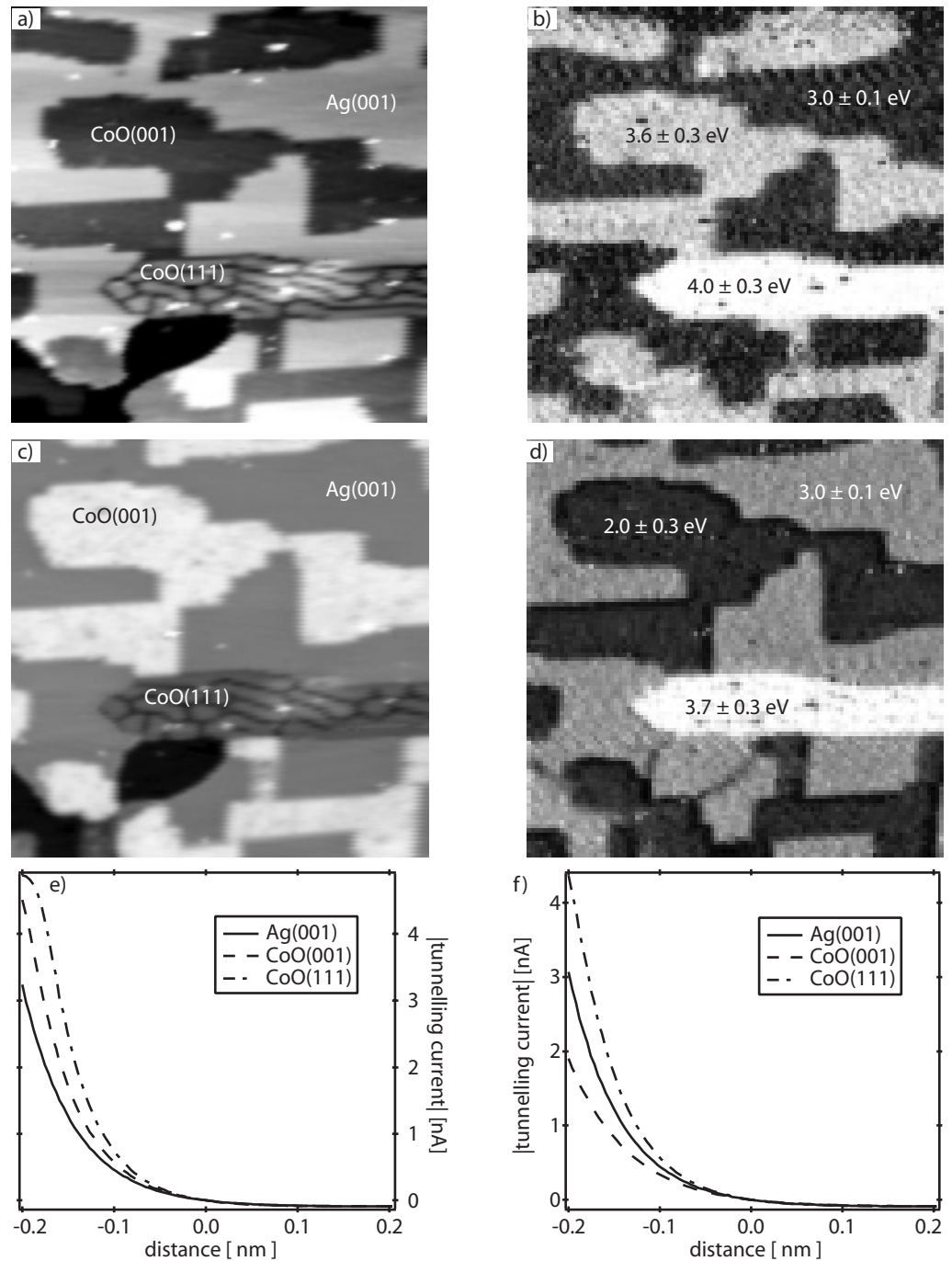
b) tunneling current map at
 $\Delta z = 0.2$ nm,

c) STM (50×50) nm²,
 $U = 3$ V, $I = 0.1$ nA,

d) tunneling current map at
 $\Delta z = 0.2$ nm,

e) $I(U)$ curves (tip stabil. at -3
V, 0.1 nA)

f) $I(U)$ curves (tip stabil. at 3
V, 0.1 nA).



They are given on the corresponding areas in the current maps for both stabilization voltages. As expected, there were no difference between the apparent barrier heights for Ag(001). This is in agreement with the standard theory of planar tunneling [57], [65] where the barrier usually represents the averaged work function of tip and sample. Therefore, it should not strongly depend on the bias polarity. For the barrier over the (111) oriented Co oxide islands, a difference of about 0.3 eV was found. One has to stress that the smaller barrier was measured at positive polarity.

On CoO(001) the apparent barrier height is lower by 1.6 eV if one stabilizes at positive bias voltage.

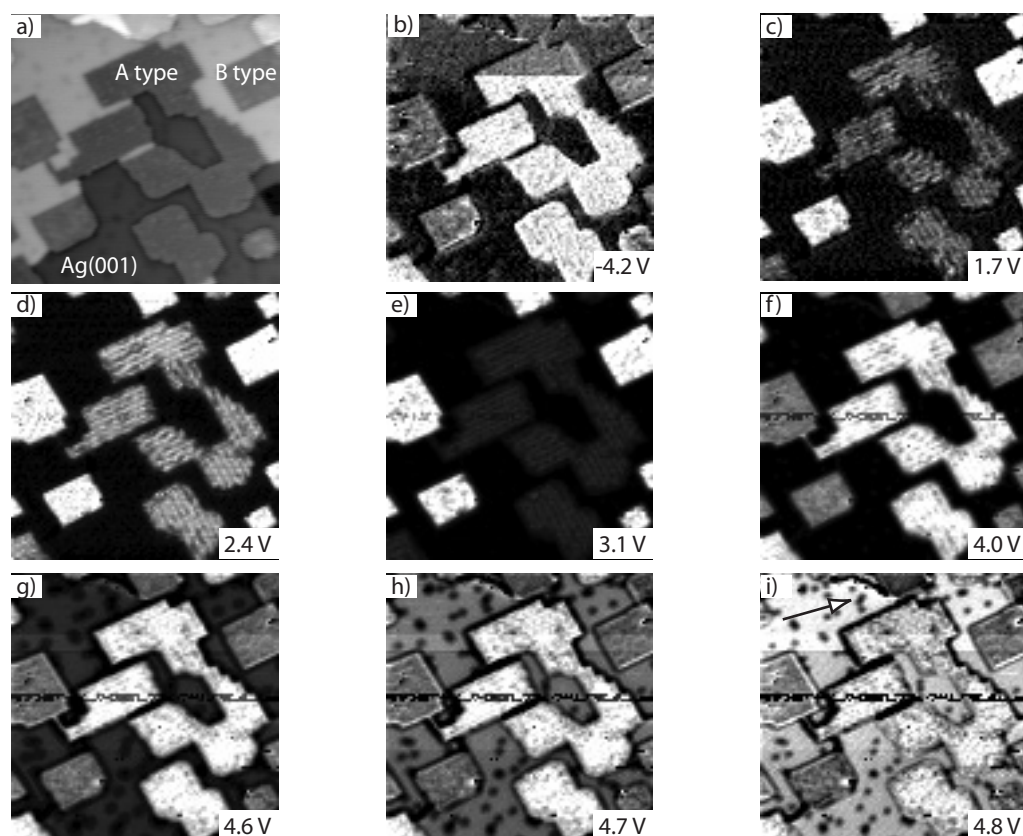
6.5.3 $I(U)$ spectroscopy of A and B precursors

In Figure 6.23, an example of an STM/STS characterisation of precursor islands is presented. A sample area is analysed where A and B type precursors are present on the Ag(001) substrate. The topography image (Figure 6.23a) is shown together with current maps (Figure 6.23b-i). In the topography image, no stripes can be recognised for the A type precursor whereas in some of the current images they are clearly visible (Figure 6.23c-f). The O induced effects (Chapter 5.2) are also revealed in a much better contrast in some of the maps (Figure 6.23g-i, see arrow). Thus, even small details can be identified in a very striking way by means of STS mapping.

Figure 6.23 STM/STS of A and B type precursors.

a) STM (50×50) nm²,
 $U = -5$ V, $I = 0.1$ nA,

b) - i) tunneling current maps,
corresponding voltages are
indicated in the right down
corner.



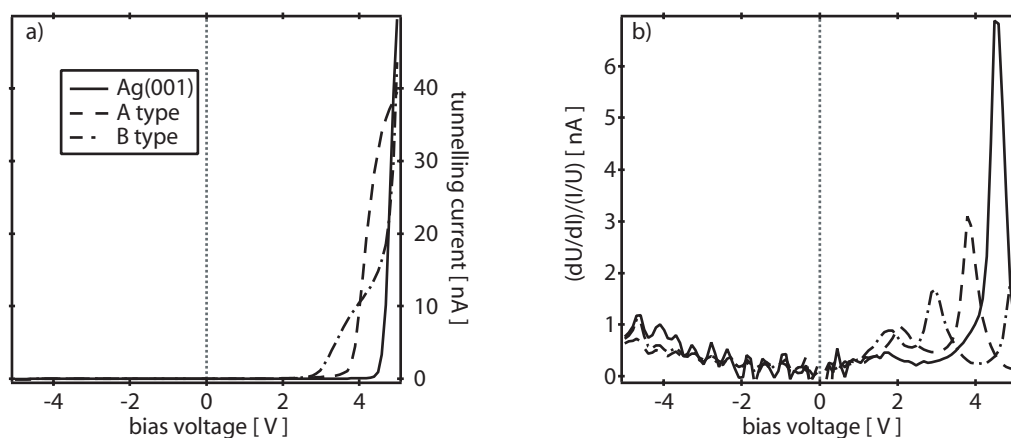
In Figure 6.24a, the corresponding $I(U)$ curves are shown together with the $(dI/dU)/(I/U)$ spectra. One can recognise clear differences for the three surface species. In the $(dI/dU)/(I/U)$ spectra, again the small peak at 1.6 V

and the strong maximum at 4.5 V make the Ag substrate different from oxides (Figure 6.24b). For the A and B type precursors, two characteristic peaks were detected. For the A type precursor, a peak at 2 V and a more pronounced peak at 3.9 V were observed. For the B type, a peak at 1.7 V and at 2.9 V were registered. It is reasonable to assume that the first peaks for both precursors (at 2 V and at 1.7 V) are related to the DOS. It is also possible that these peaks are induced by states of the precursor/metal interface. The second peaks, however, are relatively sharp and their positions on the voltage scale are close to the Ag resonant peak (at least for the A type). Therefore, they may be induced by the FER. The oscillations at the negative side are induced by mechanical vibrations.

Figure 6.24 STS data from experiment of Figure 6.23.

a) $I(U)$ curves, $U_0 = -5$ V, $I_0 = 0.1$ nA,

b) $(dI/dU)/(I/U)$ spectra.



Particular attention should be paid to the correlation of the peak positions with the contrast in the current maps (see e.g., Figure 6.23c-i). Thus, at 1.7 V where the first peak for the B type precursor was observed, the B type islands appear as the brightest features on the surface (see Figure 6.23c). Going further towards higher energy (2.4 V), no maxima were observed either for A nor for B type precursors. Correspondingly, both precursors display only slight contrast differences as can be seen in Figure 6.23d. At 3 V, the second peak of the B type precursor comes into play. Here, only the B type islands can be well recognised (Figure 6.23e). The reverse situation is given in Figure 6.23f. Here, the second peak at 3.9 V of the A type precursor determines the contrast and makes the A type islands brighter than the surroundings (see Figure 6.23f). The map serie (g-i) show how the resonant tunneling of Ag(001) can influence the contrast.

Reviewing this chapter, one has to add that the origin of the peak at 2.9 V of the B type precursor is not really clear. It looks very similar to the maximum at 2.2 V in $(dI/dU)/(I/U)$ spectra of CoO(001), but its position is slightly shifted upwards on the energy scale.

6.6**Interaction of CoO(001) with O₂**

Chung et al. [113] have reported that the band gap becomes smaller with rising O content in case of Fe oxides films. Hence, for Co oxides a similar O concentration dependence has to be expected. Therefore, the interaction of CoO(001) with O₂ and its influence on the electronic structure of insulating layers was additionally investigated.

In these experiments, CoO(001) islands were prepared at an O₂ pressure of 10⁻⁶ mbar and a substrate temperature of 420 K. Then, the film was annealed in UHV for 15 min at 500 K. This surface is imaged in Figure 6.25a. Rounded islands of double layer CoO(001) are visible. The increased number of embedded islands is in agreement with the chosen preparation conditions (Chapter 6.2). Then, this surface was again annealed for 75 min at 500 K and in O₂ atmosphere (pressure 10⁻⁶ mbar). The corresponding STM image is presented in Figure 6.25b. The effects of the interaction with O₂ are obvious. The whole Ag(001) surface is covered with dark spots similar as shown in Figure 5.16a and the appearance of the oxide islands is changed. The CoO(001) islands display a more regular shape and their surfaces show an inhomogeneous contrast. Most interesting, some of the islands display a hexagonal shape. Unfortunately, no high resolution imaging was possible on this surface due to a blunt tip. However, a series of STS experiments were conducted before and after annealing of the sample in O₂. The $(dI/dU)/(I/U)$ spectra are summarised for both CoO(001) and Ag(001) and drawn in Figure 6.25c and d.

Considering Ag first, one can notice a small shift of ~0.2 V which is in good agreement with data in Figure 5.16c, where the results of annealing experiments of Ag in O₂ are presented. In the case of the CoO(001) islands, a pronounced difference in the spectra taken before and after annealing is obvious. The maximum at 2.2 V detected for CoO(001) before the annealing disappeared after annealing and a degraded peak could be seen at 3.1 V. Also, the noise level between -1 V and 1 V was slightly reduced for the annealed film. In general, the spectra obtained after annealing look very similar to those of Figure 6.20a related to (111) Co oxide islands. This tendency of structural reordering is obvious from the spectra of Figure 6.25d.

What actually happened during the experiment? Well ordered CoO(001) islands were annealed in O₂ atmosphere. Due to interaction with O₂, the chemical composition of the CoO(001) islands may be changed towards a higher O content. Since Co₂O₃ is unstable, the next candidate with a higher oxidation state is Co₃O₄. Assuming that indeed a transformation to spinel-like structures takes place, an explanation for the formation of the hexagonal islands observed after annealing (see Figure 6.25c) is obtained. This is also in a good agreement with the results of Chung et al. [113] who performed spectroscopic investigations on a closely related system, i.e., the spinel-like Fe₃O₄.

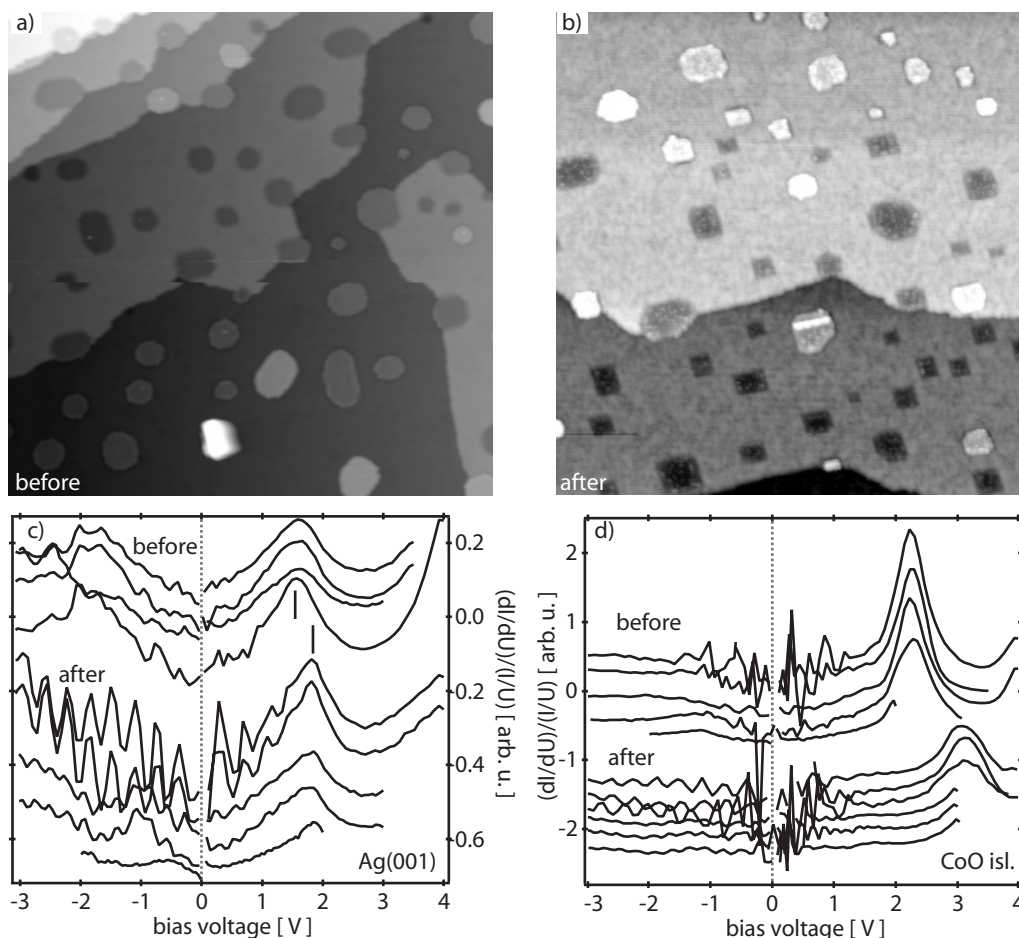
Figure 6.25 Annealing of CoO(001) in O₂ atmosphere.

a) STM (110×110) nm²,
U = -3 V, I = 0.1 nA,

b) STM (110×110) nm²,
U = -3 V, I = 0.1 nA,

c) (dI/dU)/(I/U) spectra of Ag(001) before and after annealing,

d) (dI/dU)/(I/U) spectra of CoO(001) before and after annealing.



6.7

Co clusters on CoO(001)

Nanometer scale structures as metal clusters on an insulating metal oxide support exhibit fascinating properties as, e.g., Coulomb blockade and Coulomb staircase effects. They belong to the frontiers of modern electronic technology and are candidates to replace conventional transistors [126]. Metal clusters on insulating surfaces are, therefore, one of the main systems investigated in nanoscience. They attract many theoretical and experimental groups [127], [128]. Recently, it was also shown that metal clusters supported on metal oxides are particularly suited for catalysing the oxidation of CO [129]. A deeper understanding of structure/activity relations in surface catalysed reactions is therefore one of the most important goals of surface science studies related to heterogeneous catalysis.

Since metallic Co was evaporated for CoO(001) epitaxy, it was no problem to produce metallic clusters after the growth of an oxide film by postdeposition of Co in UHV. In Figure 6.26a, 0.3 ML of Co was deposited at RT onto B type precursor islands (1 ML thick CoO). A large number of Co clusters are formed. On both Ag and precursor surfaces, Co grows in a three-dimensional manner as

actually expected according to [96] or [130]. Most of the clusters nucleated on the uncovered Ag(001) areas. Obviously, Co does not like to nucleate on the precursor if areas of uncovered Ag(001) are present. Nucleation along island step edges was also observed (arrow). Increasing the Co coverage by an additional deposition of Co yield an increase of the Co cluster density not only on Ag(001) but also on the precursor islands (see Figure 6.26b).

At this point, one needs to mention that even at low temperatures it was quite difficult to obtain stable imaging conditions and a good resolution. Actually, there are only few examples in the literature where atomic resolution was obtained for facets of flat clusters several nm in size as in [131]. Moreover, the convolution with the tip shape can lead to an inflation of the lateral cluster size. Those cluster appear then in the STM images bigger then they really are.

Figure 6.26 Co clusters on CoO(001)/Ag(001) surface

a) 0.3 ML of Co
STM (40×40) nm²,
 $U = -3$ V, $I = 0.1$ nA,

b) additional 0.2 ML of Co
STM (40×40) nm²,
 $U = -3$ V, $I = 0.1$ nA.

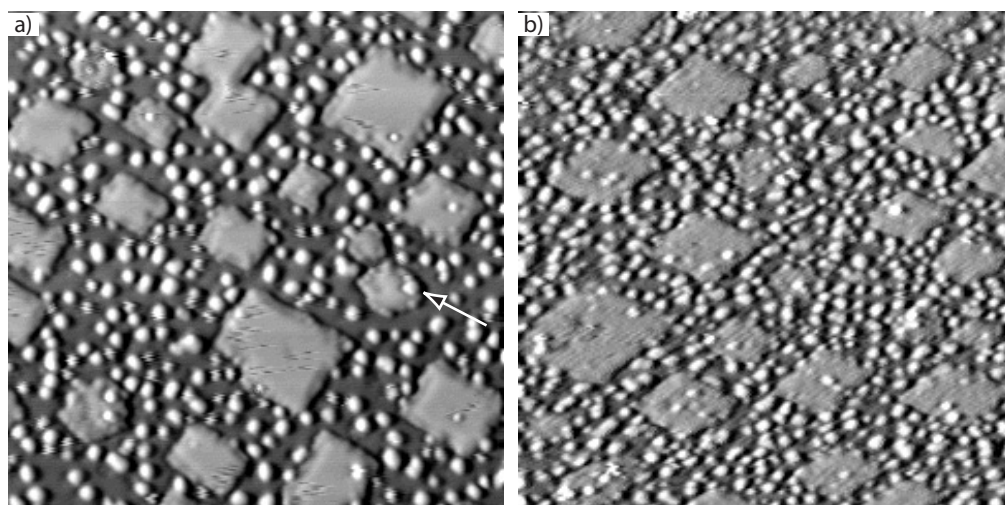


Figure 6.27a shows a surface of a 4-5 ML thick CoO(001) film which completely covers the Ag substrate. The film is relatively smooth and displays two-dimensional CoO islands due to the multi layer morphology of the film as described in detail by Sebastian [22]. Onto this film, ~ 0.5 ML of Co was deposited at 77 K which yields the surface imaged in Figure 6.27b. A large number of Co clusters is observed on the terraces. At a first glance, there are no clear preferential nucleation sites. Even at the steps, the cluster density does not seem to be not essentially increased. This is quite different from the results of a RT deposition of Co. As demonstrated in Figure 6.27c, taken from [22] (note the different image size), the Co clusters decorate the step edges and the nucleation density on the terraces is by an order of magnitude smaller than for 77 K Co deposition. Obviously, at RT, most of the Co atoms migrate to the edges which act as nucleation sites inducing the formation of large clusters (size 2-5 nm). For the clusters prepared at 77 K, however, the heights and widths amount to 0.2 - 0.6 nm and 0.5 - 2 nm, respectively. In Figure 6.28a, $I(U)$ curves taken on different clusters are presented. Different curves for each cluster were obtained. Due to the different cluster size, a precise cluster characterisation by STS was difficult. Nevertheless, it is possible to conclude from the curves that the supported clusters have a band gap. Whether the band gap is resulting from the CoO(001) support alone or also from contributions of the Co clusters, can not be decided yet. In principle, the results are in agreement with STS data obtained on Pd and Au clusters on TiO₂(110) [132],[133], respectively. There, it was

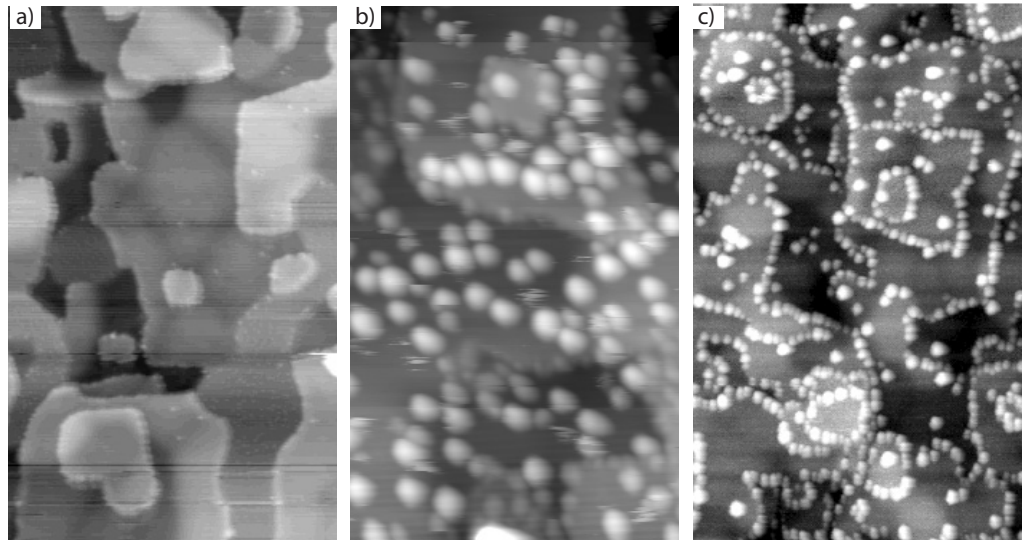
found that the cluster size and the cluster distribution strongly depend on the metal coverage, the evaporation rate, and the substrate temperature. Higher rates and lower temperatures led to smaller clusters and to a narrower cluster size distribution, apparently due to the competing processes of nucleation and growth. Smaller clusters reveal significantly larger band gaps whereas bigger ones exhibit a metallic behaviour, indicating the transition to a bulk-like electronic structure. Also smaller clusters are more reactive towards CO and O₂.

Figure 6.27 Co clusters on a CoO(001) film.

a) clean CoO(001) surface:
STM (50×84) nm²,
 $U = -3$ V, $I = 0.1$ nA,

b) Co clusters at 77 K:
STM (25×40) nm²,
 $U = -3$ V, $I = 0.1$ nA,

c) Co clusters at RT:
STM (90×150) nm²,
 $U = -1,9$ V, $I = 0.1$ nA, taken
from [22].

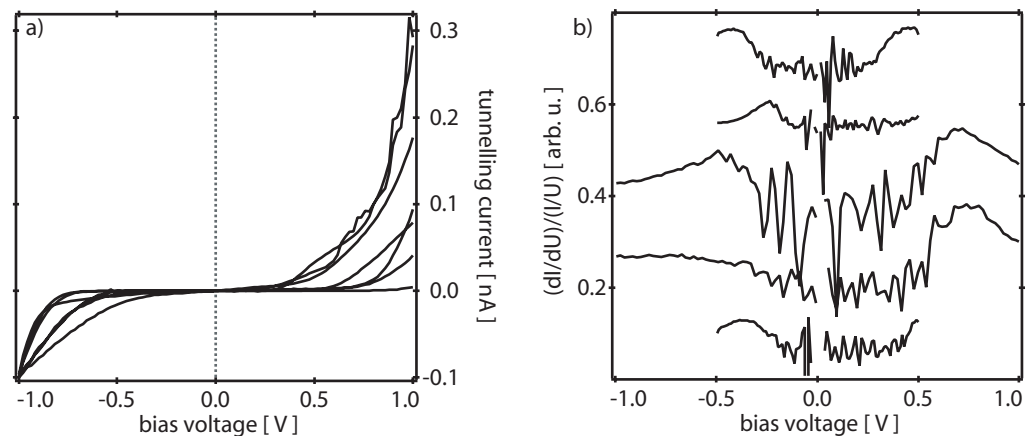


In Figure 6.28b, $(dI/dU)/(I/U)$ spectra of several Co clusters are shown which were deduced from Figure 6.28a. As can be seen, all spectra have indications of a band gap, but it could not be well reproduced. A more reliable measurement would be possible by using the lock-in technique for characterising the clusters as reported by Bettac et al. [134].

Figure 6.28 STS data of Co clusters on CoO(001).

a) $I(U)$ curves, $U_0 = -1$ V, $I_0 = 0.1$ nA,

b) $(dI/dU)/(I/U)$ calculated
form a).



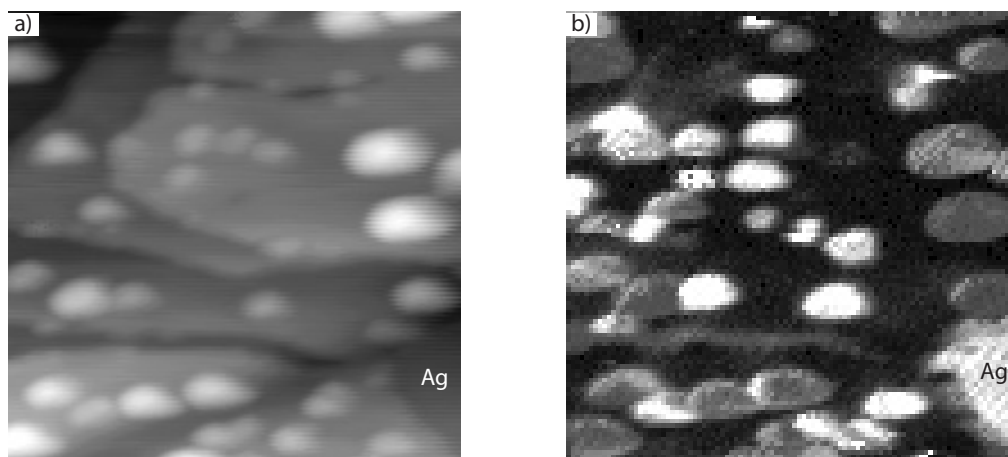
A further UHV annealing at ~ 450 K of the sample shown in Figure 6.27b led to a rearrangement of the surface (see Figure 6.29a). The cluster number decreased and their mean diameter became larger by surface diffusion. In addition to that, the Ag(001) substrate became partly visible. At temperatures around 600 K, almost all clusters disappeared from the surface indicating a diffusion of Co through the oxide into the substrate. A similar volume diffusion process was observed for Co clusters on top of alumina for temperatures > 700 K.

In Figure 6.29b, a current map taken at $U = 2$ V of the topography shown in Figure 6.29a is presented. In the current image, the Co clusters seem to be larger than their topographic size. This is probably caused by a blunt tip.

Figure 6.29 Co clusters on CoO(001) annealed at ~ 450 K.

a) STM (20×20) nm²,
 $U = -2$ V, $I = 0.1$ nA,

b) current map at $U = 2$ V.



All in all, the Co/CoO/Ag system has been revealed as a quite complicated one. Due to the size dependent properties of the Co clusters, a general characterisation was difficult. Moreover, the tip shape played a crucial role in the imaging process of the clusters. Nevertheless, the presence of a band gap could be recognised already in the $I(U)$ curves. This electronic behaviour together with the observed growth mode made the Co/CoO system suitable for adsorption and reaction experiments already at this stage. And it would be interesting to know how reactive the Co clusters are in dependence on their size. For alumina supports, e.g., Pd and Pt clusters display different activities in chemical reactions as was shown by Bäumer et al. [138]. Thus, this system (or any other metal clusters on CoO/Ag) remains of great interest for future studies.

Growth of Mn and Mn oxides on Ag(001)

Among the 3d TMOs, most attention was paid to the epitaxial growth of NiO and CoO on Ag(001) surfaces [26]-[29] due to the small lattice mismatch (2-4%). For the MnO/Ag(001) system, however, the mismatch is much larger (~9%). Nevertheless, Müller et al. [30] were able to prepare epitaxially grown MnO films of good structural quality for performing EELS and AREELS studies. This chapter describes first attempts for characterising Mn and different Mn oxides grown on Ag(001) by means of STM/STS.

7.1

Initial stages of Mn film growth on Ag(001)

Mn thin films on various noble metal substrates have attracted great attention because of their magnetic properties. The system Mn/Ag(001) has been of particular interest [139]-[144]. It was found that ultrathin Mn films have a quadratic unit mesh of 0.29 nm in size which is equal to that of Ag(001). In addition, satellite structures of a well defined Mn-Ag superlattice were found in XRD [139]. Kim et al. [140] reported on LEED investigations of the Mn/Ag(001) system revealing for 0.5 to 1.5 ML thick Mn films a bright $c(2\times 2)$ pattern. This pattern originated from a 2 ML thick surface alloy. The formation of this epitaxial Ag-Mn alloy was systematically studied by Schieffer et al. [141]-[144] by means of ion scattering spectroscopy, ARUPS, and LEED. The $c(2\times 2)$ LEED superstructure was observed up to 3 ML Mn (with a maximum intensity of the fractional order beams at ~1.5 ML).

In spite of the large number of publications dealing with the Mn/Ag(001) system, STM investigations are missing up to now. In the following, results on the growth of Mn on Ag(001) by STM/STS will be described.

In order to reproduce the results of [140]-[143], Mn was deposited onto Ag(001) surface at RT. In Figure 7.1a-d, LEED patterns and the corresponding STM images obtained after depositing 0.15 ML, 1.4 ML, and 2.4 ML of Mn are shown. The surface is covered exclusively by two-dimensional islands not only in the submonolayer range (Figure 7.1c), but also at higher coverages (Figure 7.1d,e). The steps of the Mn islands are mainly oriented in along [110]-like directions. Obviously, the Mn grows in a perfect layer by layer mode via nucleation, two-dimensional growth, and coalescence of the islands. During the film growth, a $c(2\times 2)$ structure appears in the LEED pattern (Figure 7.1b, see arrow). Unfortunately, this (2×2) structure could not being yet resolved in the STM measurements.

In Figure 7.1e, the STS data obtained for the 2.5 ML thick Mn film are displayed which were measured on the terraces and the islands. In the (dI/dU) curves, two characteristic peaks were found at 0.3 V and 0.7 V. For the Mn/Fe(001) system [145], [146], in STS studies similar characteristic peaks were detected at 0.28 V and 0.8 V. They have been assigned as Mn induced. This system is also characterised by a $c(2\times 2)$ structure. Thus, one can conclude that both peaks at 0.3 V and 0.7 V are signatures for Mn. They were not observed on the clean Ag(001) surface.

Figure 7.1 Initial stages of the epitaxial growth of Mn on Ag(001) at RT.

a) LEED pattern of ~ 0.15 ML Mn on Ag(001), $E_{\text{kin}} = 156$ eV,

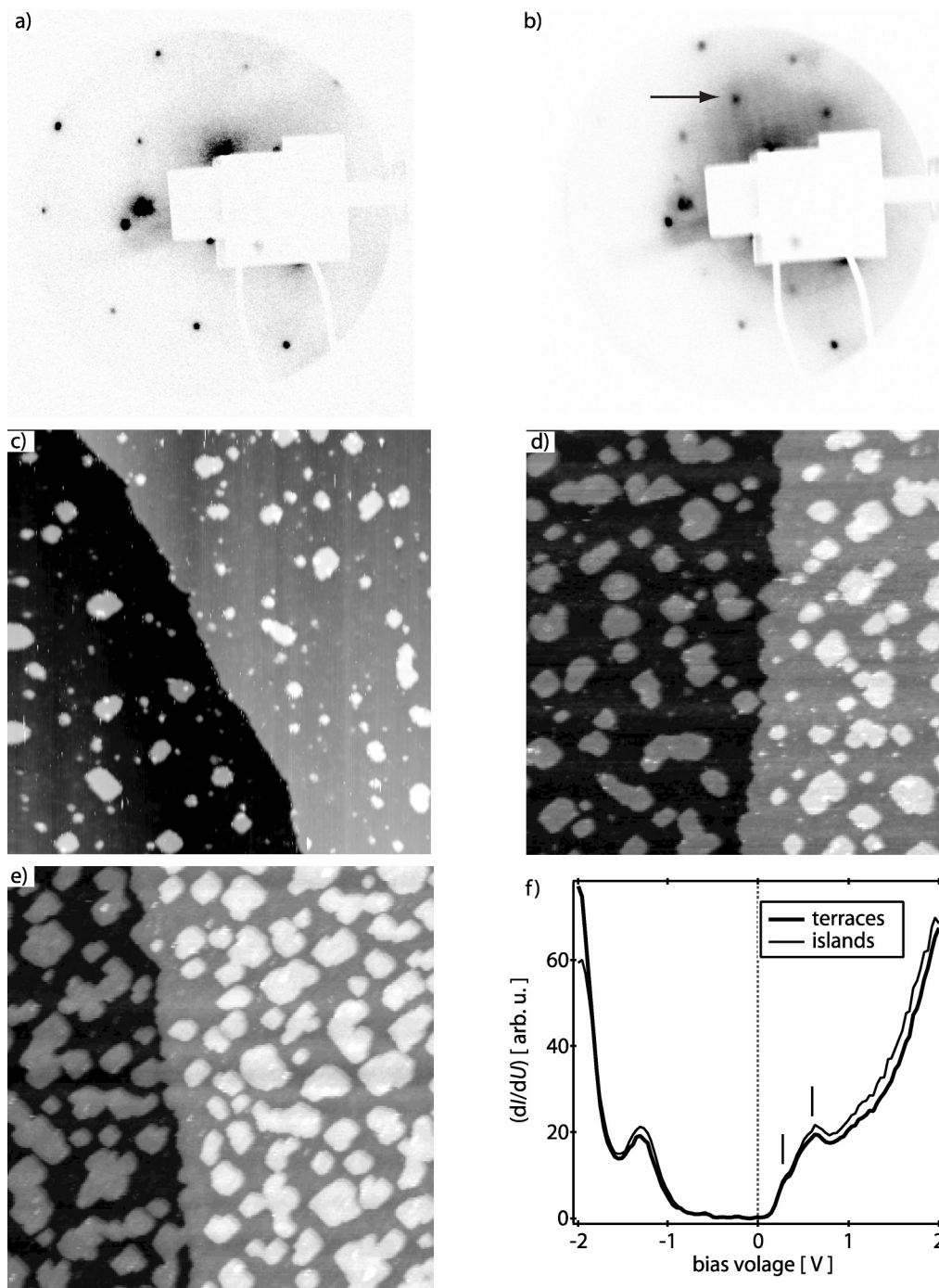
b) LEED pattern of ~ 1.4 ML Mn on Ag(001), $E_{\text{kin}} = 156$ eV,

c) ~ 0.2 ML Mn on Ag(001), STM (50×50) nm², $U = -3$ V, $I = 0.1$ nA,

d) ~ 1.4 ML Mn on Ag(001), STM (50×50) nm², $U = -3$ V, $I = 0.1$ nA,

e) ~ 2.4 ML Mn on Ag(001), STM (50×50) nm², $U = -3$ V, $I = 0.1$ nA,

f) (dI/dU) spectra taken on islands and terraces imaged in (d).

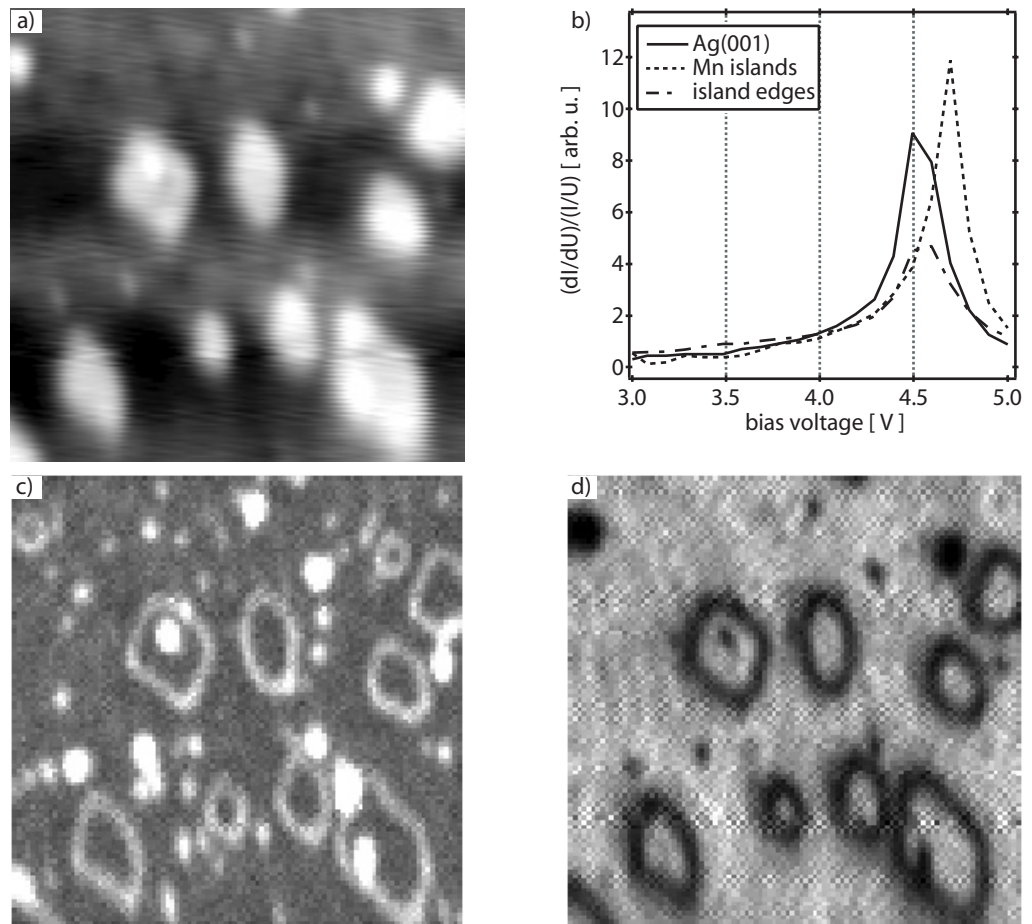


For getting more insight into the alloy formation occurring in the very beginning of the film growth [140]-[144], the submonolayer stage was analysed in more detail. Using the STM/STS technique, different chemical compositions can be identified locally. This is demonstrated by the results shown in Figure 7.2. In Figure 7.2a, a topography image of submonolayer islands taken at -5 V is depicted. In Figure 7.2b, the $(dI/dU)/(I/U)$ curves obtained on the Ag substrate, the centre of the islands, and the edges of the islands are displayed. The current maps of Figure 7.2c,d taken at 4 V and 4.9 V, respectively, show the same image area as in Figure 7.2a. Surprisingly, in the current maps, only the fringes of the island edges are visible. At 4 V the fringes appear bright and at 4.9 V they are

dark. This indicates that the edges have their own specific electronic structure and chemical composition, respectively. This distinction can also be confirmed spectroscopically. Three different peaks were found in the $(dI/dU)/(I/U)$ curves in Figure 7.2b. For Ag(001), Mn islands, and island step edges, the peak positions are located at 4.5 V, 4.55 V, and 4.7 V, respectively. This means that the peak position is characteristic for the material. The fact that the peak of the island edges is lying between the peaks of Ag and Mn can be interpreted as an indication that the edges have a higher Ag content than the centre parts of the islands.

Figure 7.2 STS experiment on Mn/Ag(001) system.

- a) ~ 0.4 ML Mn
STM (30×30) nm²,
 $U = -5$ V, $I = 0.1$ nA,
- b) corresponding $(dI/dU)/(I/U)$ spectra,
- c) current map taken at $U = 4$ V,
- d) current map taken at $U = 4.9$ V.



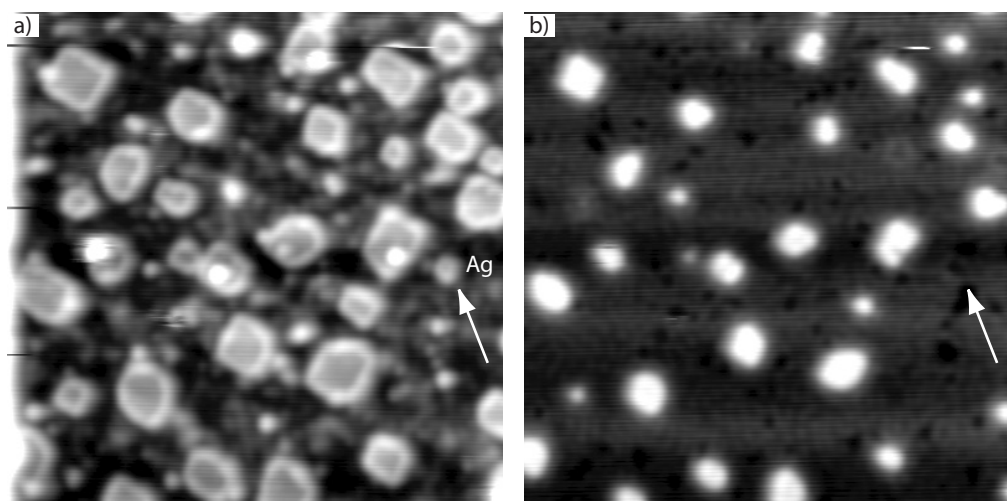
Using the clear differences between the peak positions in the $(dI/dU)/(I/U)$ spectra, other submonolayer islands were deliberately imaged at the corresponding peak voltages in order to get a chemically selective imaging contrast. In Figure 7.3a, an STM image of the islands is shown which was taken at a bias voltage of 4.5 V (characteristic for Ag). In Figure 7.3b, the same area was imaged at 4.8 V (more characteristic for Mn). Clear differences become obvious. At 4.5 V, the islands appear much larger and display a bright fringe. In addition, there are more islands visible at 4.5 V than at 4.8 V (see e.g., arrow). Moreover, the terraces between the islands appear blurred. These different features can be interpreted by assuming that the centre parts of the islands are composed of Mn (imaged at 4.8 V) and the edges of the islands of Ag. In addition, there exist Ag islands formed during the Mn deposition (similar as during the Co growth on Ag(001) [22]) which are not visible at 4.8 V. Moreover, the terraces below the islands most probably are partly formed by Mn-Ag compounds which explains their blurred appearance.

The chemical contrast can be attributed to the local work function of different materials. By operating the STM at higher bias voltages where the transition between tunneling and field emission occurs, a series of sharp resonances are available for enhanced tunneling. The peaks in the STS curves of Figure 7.2b obviously correspond to the field emission resonances of the different materials. In the $I(U)$ STS studies of Ag(001), at least the first Ag resonance state could be clearly identified (Chapter 5.1). By switching the bias between the resonances of the different materials, one is able to obtain a chemical contrast [147] and to distinguish between the elements.

Figure 7.3 STM images of ~ 0.4 ML of Mn deposited at RT.

a) STM (50×50) nm²,
 $U = 4.5$ V, $I = 0.1$ nA,

b) STM (50×50) nm²,
 $U = 4.8$ V, $I = 0.1$ nA.



7.2

Initial stages of Mn oxide film growth on Ag(001)

The studies of Mn oxide film formation by using reactive deposition of Mn onto Ag(001) are thought to provide a first overview on the general growth mode of Mn oxides. A reference point for the preparation was given in the work of Müller et al. [30] where for $p(\text{O}_2) \sim 10^{-8}$ to 5×10^{-7} mbar well ordered MnO films on Ag(001) were obtained even at RT. It was also found that a further increase of the O_2 pressure leads to the formation of Mn oxides with Mn in higher ionisation states such as Mn_2O_3 or Mn_3O_4 . In the present work, both O_2 pressure and substrate temperature dependent investigations were made for the Mn/O/Ag(001) system.

7.2.1 O_2 pressure of 10^{-7} mbar

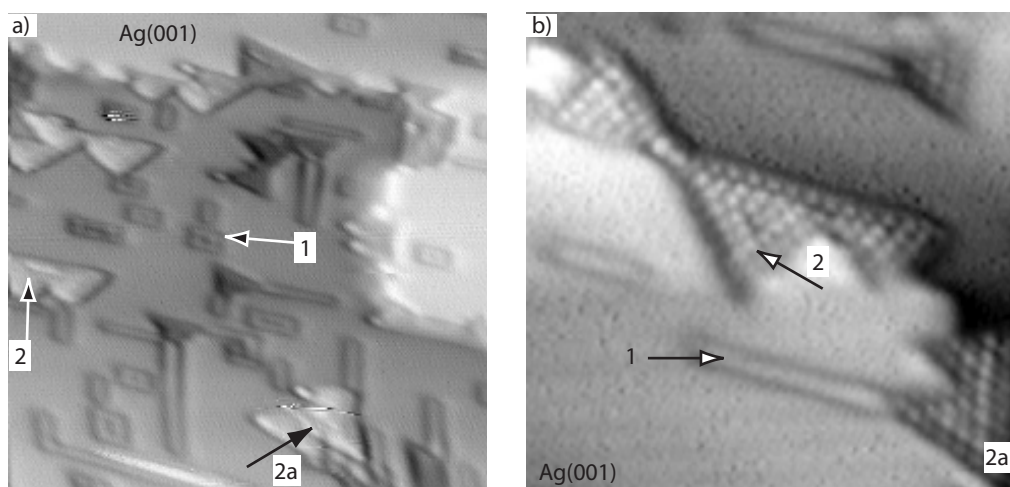
Figure 7.4 shows an STM image taken on a surface after RT deposition of ~ 0.2 ML Mn in O_2 atmosphere and subsequent UHV annealing at 500 K. An island growth of MnO(001) was expected for this preparation conditions according to [30]. However, two different island types (marked as (1) and (2) in Figure 7.4a) were observed. On Figure 7.4b, one can clearly recognise that the islands (1) have a rectangular shape and are, therefore, assigned to be MnO(001). Islands (2), however, reveal a three fold symmetry which indicates a (111) orientation. Similar as in the case of (111) Co oxide islands, two different domains (islands 2

and 2a in Figure 7.4) were found according to the model of Figure 6.7. Atomic resolution was achieved for the (111) oriented islands in contrast to those of (001) orientation (see Figure 7.4b).

Figure 7.4 ~0.2 ML Mn deposited in 10^{-7} mbar O_2 at RT and post annealed in UHV at 500 K.

a) STM (30×30) nm²,
 $U = -2$ V, $I = 0.1$ nA,

b) STM (5×5) nm²,
 $U = -0.08$ V, $I = 0.3$ nA.

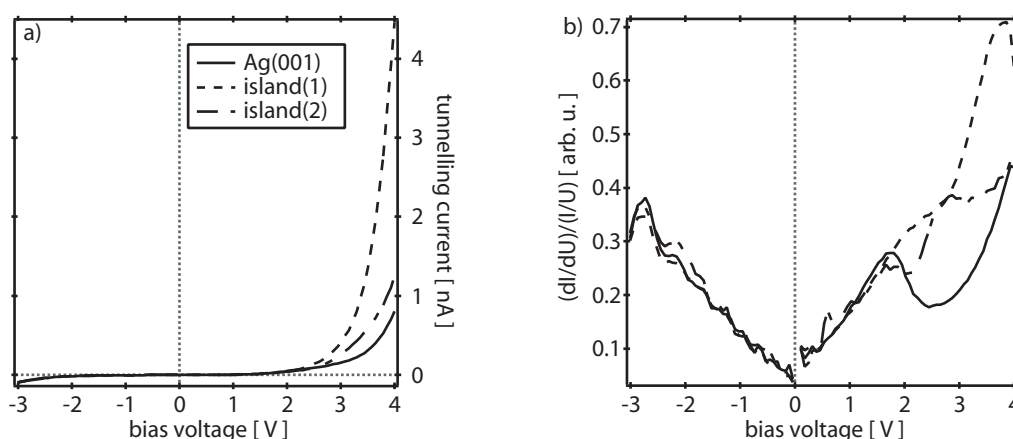


Both kind of islands were found on top and embedded into Ag(001). This can be understood by assuming intermixing during the Mn oxide film formation. In Figure 7.5a, the $I(U)$ curves taken on Ag(001) and on the (001) and (111) oriented islands are shown. A similar spectroscopic behaviour was found as in the case of Co oxide islands (Chapter 6.5.1). Consequently, both types of Mn oxide islands reveal a bias voltage dependent contrast in the STM images (not shown here). In Figure 7.5b, the $(dI/dU)/(I/U)$ spectra are displayed. Two characteristic peaks at 1.8 V and 3.8 V are found for the (001) Mn oxide islands. No pronounced features are observed for (111) Mn oxide islands. For voltages > 1.5 V, both characteristics are different from the Ag spectrum. In spite of the obvious spectroscopic distinction between all investigated species, no clear conclusions on the electronic structure of the Mn oxide islands could be made. Also the chemical composition of the islands remains an open question for further investigations.

Figure 7.5 STS experiment on islands present in Figure 7.4.

a) $I(U)$ curves stabil. at $U = -3$ V $I = 0.1$ nA,

b) corresponding $(dI/dU)/(I/U)$ spectra.



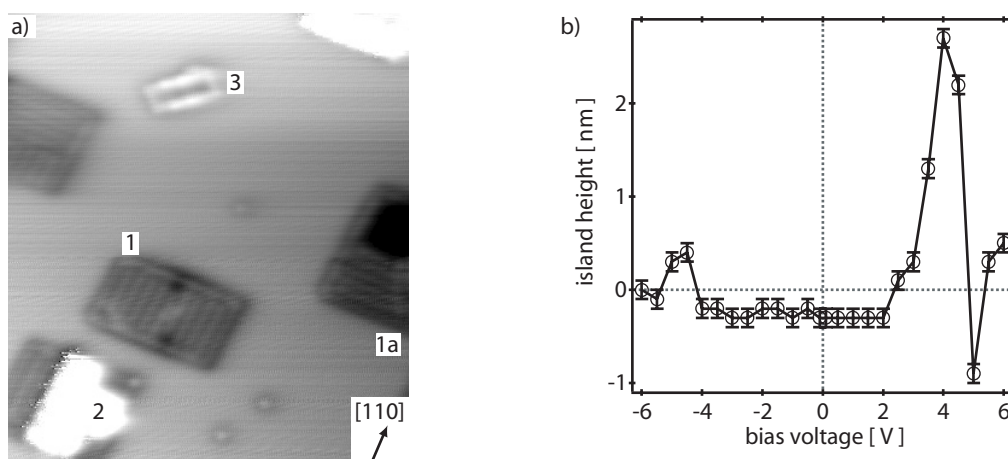
The situation is slightly different when the Mn deposition occurs at elevated temperatures. This is demonstrated by Figure 7.6a which shows several Mn oxide islands grown at 450 K. Three new types of islands were observed numbered as (1), (2) and (3). Islands (1) are embedded into Ag(001) and oriented in [110]-like directions relative to the substrate. A kind of a (2×1) reconstruction was

found on those islands in two perpendicular orientations according to the main substrate directions (compare islands (1) and (1a) in Figure 7.6a). Bias voltage dependent measurements were performed for this island. The measured apparent step height is drawn in Figure 7.6b vs. bias voltage. The presence of a band gap between -4 V and 2 V could be derived from this graph. Spectroscopic experiments did not yield reliable results and are omitted here. On top of islands (1), occasional islands of type (2) are found. They do not display a pronounced bias voltage dependent contrast behaviour and have a tendency of step orientation in [100]-like direction. Finally, there are islands of type (3). In contrast to islands (1), they are oriented parallel to [100]-like substrate directions. Characteristically, they reveal pronounced edge effects which may indicate that the edges have a different composition in comparison to the centers.

Figure 7.6 ~0.2 ML Mn deposited in 10^{-7} mbar O_2 at 450 K.

a) STM (17×19) nm²,
 $U = -0.09$ V, $I = 0.41$ nA,

b) apparent step height vs. bias voltage measured for island (1) with respect to Ag(001).



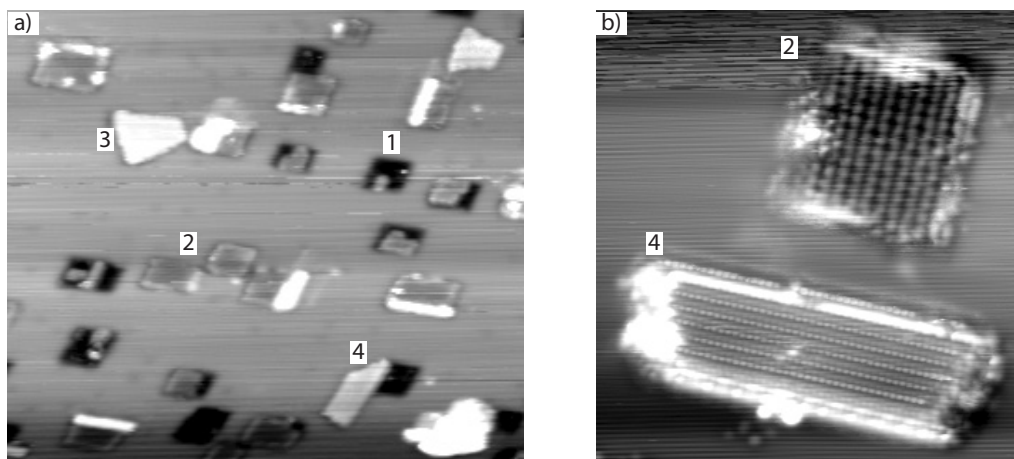
7.2.2 O_2 pressure of 10^{-6} mbar

Figure 7.7a shows the surface after deposition of ~ 0.3 ML Mn in an O_2 atmosphere at a substrate temperature of 450 K. Again different types of islands were observed for the chosen preparation conditions. Islands (1) were observed as dark depressions, they displayed a rectangular shape. Their step edges are oriented along the [110]-like substrate directions. Islands (2) grow on top of islands (1) and reveal a (2×2) surface reconstruction as revealed in the high resolution image of Figure 7.7b. It may correspond to MnO since Langell et al. [148] observed for MnO(001) single crystals annealed in UHV a (2×2) surface reconstruction. Islands (3) probably correspond to an island type found already at lower O_2 pressure (see island (3) of Figure 7.6a). Finally, islands (4) grow on top of islands (1) and show a (2×1) reconstruction as atomically resolved in Figure 7.7b.

Figure 7.7 ~0.3 ML Mn deposited in 10^{-6} mbar O_2 at 450 K.

a) STM (60×68) nm²,
 $U = -3$ V, $I = 0.41$ nA,

b) STM (16×15) nm²,
 $U = -0.2$ V, $I = 0.7$ nA.

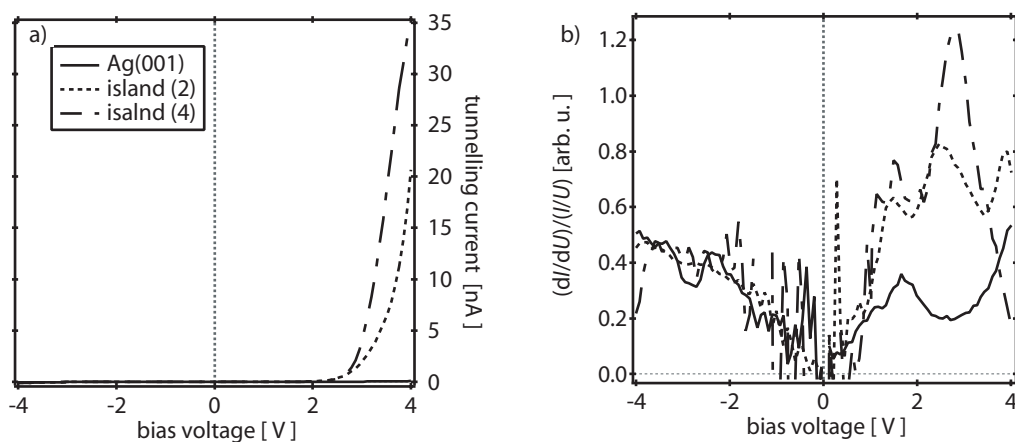


The results of the STS investigations are shown in Figure 7.8. Besides Ag(001) only the islands (2) and (4) were analysed. The corresponding $I(U)$ curves are presented in Figure 7.8a. It can be seen that both island types have a pronounced oxidic behaviour and several characteristic peaks were found for them in the $(dI/dU)/(I/U)$ spectra (Figure 7.8b). The spectra presented here are clearly different from those in Figure 7.5b at voltages > 1 V. This indicates different electronic structures. Three characteristic peaks were found for islands (2) at 1.6 V, 2.2 V, and 3.9 V, respectively. Islands (4) display only two peaks at 1.7 V and 3 V. At the negative side, no reliable information is available.

Figure 7.8 STS experiment on islands presented in Figure 7.7.

a) $I(U)$ curves stabil. at $U = -4$ V, $I = 0.1$ nA,

b) corresponding $(dI/dU)/(I/U)$ spectra.



Actually, at elevated temperatures (~ 450 K) and high O_2 pressures (10^{-6} mbar) a growth of Mn_2O_3 together with Mn_3O_4 was expected [23] and it is possible that those structures were really grown. Systematic studies at these conditions are therefore required in the future.

It was shown, that at all O_2 pressures the growth of Mn related oxides is strongly dependent on the substrate temperature and therefore it is necessary to systematically investigate the temperature region from RT up to 600-700 K. On the other hand, it was confirmed that already at an O_2 pressure of $\sim 10^{-7}$ mbar structures with oxidic behaviour can be grown.

7.2.3 Comparison of $I(U)$ and $z(U)$ STS data

For characterising Mn oxide films by STM/STS in a first step, $z(U)$ STS experiments were performed and compared with the $I(U)$ data obtained on the same area. The (dz/dU) spectra for both the Ag(001) substrate and the island marked in Figure 7.7b as (4) are reproduced in Figure 7.9. First of all, the three peaks at 1.6 V, 2.2 V, and 3.9 V are still nicely seen (only the peak at 3.9 V is much weaker in comparison to that of the $(dI/dU)/(I/U)$ spectrum of island (2) in Figure 7.8b. Field emission related resonances are found to be at 5-6 V (for the first peak). They are not as pronounced as for Ag(001), but, nevertheless, they could clearly be distinguished. The next interesting feature is connected to the appearance of a peak at -1.8 V for the oxide island and which is not seen in the Ag spectrum. Since the peak is oxide related, it seems to be reasonable to refer it to the valence band maximum. This assumption is based on the $(dI/dU)/(I/U)$ spectra of CoO(001) where also a small peak at -1.5 V was found. Since no peak was observed in the $(dI/dU)/(I/U)$ spectrum of Mn oxide (see Figure 7.8b), one can conclude that $z(U)$ spectroscopy is more sensitive and could therefore be used for a characterisation of the oxide films similar as $I(U)$ STS.

Figure 7.9 (dz/dU) STS data for Ag(001) and island (1) of Figure 7.7b.

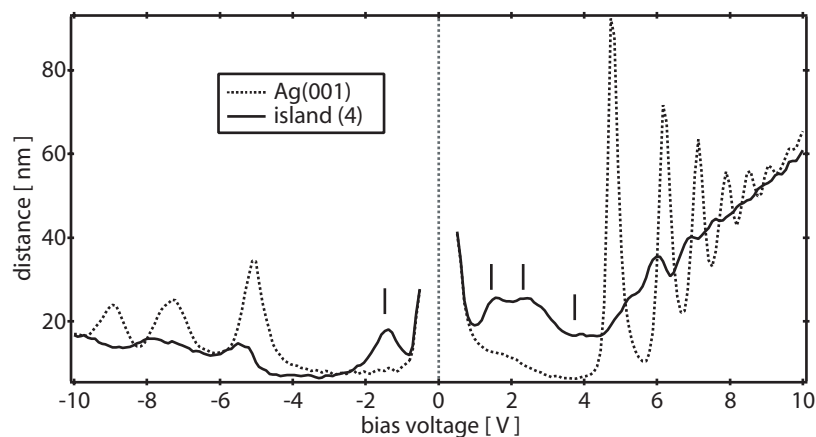
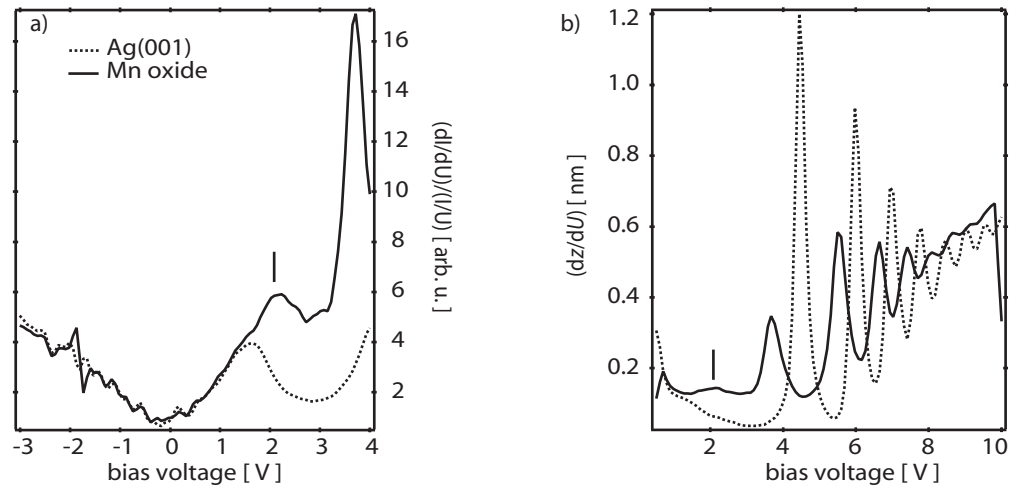


Figure 7.10 is an illustrative example of the close relationship between both spectroscopic techniques. A very high sensitivity could be assigned to the $z(U)$ method. The STS data were acquired on one of the Mn oxide islands. Special attention should be paid to the reproducibility of all spectroscopic features observed in Figure 7.10a. Thus, even the small peak at 2.2 V appear exactly at the same position in Figure 7.10b. The same happens for the peak at 3.8 V in Figure 7.10a. Again, field emission related resonances of the Mn oxide islands could be clearly distinguished from those caused by the local electronic structure of the oxide surface. This is in a good agreement with the data evaluation already applied in this work for Co oxides.

Figure 7.10 Comparison of $(dI/dU)/(I/U)$ data with (dz/dU) measurement.

a) $(dI/dU)/(I/U)$ spectra,

b) (dz/dU) data for the same island.



It has been demonstrated that field emission resonances can nicely be observed on well-defined Mn oxide surfaces. Thus, the $z(U)$ STS can yield an additional information on the electronic structure of the oxide surface. Therefore, this technique has to be applied for the future investigations (which has not been attempted for the Co oxide surfaces).

Summary and outlook

The main task of present work was to investigate the growth, the atomic and the electronic structures of Co oxide as well as Mn oxide films on Ag(001) by means of STM/STS at LT (100 K). The films were prepared by means of a reactive deposition of the metals in an O₂ atmosphere. The investigations were focused on the initial stage of the oxide film growth where a fascinating variety of different island types was found.

In the first step, the Ag(001) substrate was investigated. The good quality of the used Ag(001) surface was confirmed by STM and LEED. Moreover, the electronic structure of the Ag(001) surface was determined by means of STS. A characteristic DOS peak was found in the $(dI/dU)/(U/I)$ curves at an energy of ~ 1.6 eV above the Fermi level. In addition, a pronounced peak at 4.5 ± 0.1 V was observed in the $(dI/dU)/(U/I)$ spectra when the applied bias voltage ramp was extended to ± 5 V. This peak was assigned to the first FER peak. A systematic study of the field resonance states was performed by means of $z(U)$ STS. The dependence of the number of the observed resonances on the applied bias voltage and on the tip displacement was studied. In addition, the tip/sample distance was estimated from $I(z)$ spectroscopic measurements at bias voltages < 1 V.

The interaction of O₂ with Ag(001) was investigated at different substrate temperatures and different exposures. It was found that at 77 K O₂ is mainly molecularly adsorbed. At temperatures above 450 K, the formation of “black dots” related to O was observed. In addition, a shift of the Ag surface state peak in the $(dI/dU)/(I/U)$ spectra was found. The presence of characteristic defects observed after several film growth experiments on Ag(001) surface was assigned to an O accumulation in the bulk followed by O segregation towards the surface.

Co oxides on Ag(001)

The deposition experiments were conducted at temperatures between 380 K and 500 K. The O₂ pressure was varied in the range between 10^{-6} mbar and 10^{-5} mbar. In the initial stage of growth, two types of Co oxide precursor develop (thickness 1 ML). In addition, 2-4 ML thick CoO(001) islands were found at an O₂ pressure of 10^{-6} mbar. The transition process from the precursor state to the double layer CoO(001) islands was characterised by STM studies. Increasing the O₂ pressure to 10^{-5} mbar led to the formation of (111) oriented Co oxide islands with a thickness of 1 ML and 2 ML. The latter islands showed a moiré pattern due to the formation of two (111) layers of CoO with slightly different lattice parameter. Finally, a phase diagram was drawn which displays the development of the different Co oxide species depending on the substrate temperature and the O₂ pressure.

Using LT STM, the stability of the tunneling process was increased. This enabled high resolution STM imaging of the Co oxide islands and the Ag(001) surface. Atomic resolution was obtained for all oxide species allowing a structural characterisation of the islands.

Due to the high stability at LT, additional knowledge was gained concerning the voltage dependent contrast behaviour of all Co oxide island types. The measured apparent island height was drawn vs. the applied bias voltage. Different behaviour were observed for both precursor islands, the CoO(001) islands, and the (111) oriented Co oxide islands revealing their different electronic natures. In the bias voltage range of ± 5 V the 2 ML, 3 ML, and 4 ML thick CoO(001) islands did not show differences in their electronic behaviour. However, a contrast reversal (negative apparent island height) was only observed for 2 ML and 3 ML thick islands. A band gap of 2.5-3 eV was estimated from the measurements. In addition, the influence of the first FER state on the apparent island height was studied. The data were found to be in agreement with STS investigations performed on the Ag(001) surface.

STS investigations were successfully performed on all types of Co oxide islands. Spectroscopic fingerprints were obtained for each oxide species observed. A qualitative interpretation of the STS data was attempted and several models were developed in order to explain the peaks in the $(dI/dU)/(I/U)$ curves. DOS effects as well as effects induced by resonant tunneling were assumed. The $I(U)$ spectra as well as the $(dI/dU)/(I/U)$ curves of the CoO(001) islands were analysed in more detail. The dependence of those spectra on the CoO island thickness was studied and no pronounced changes were found between 2 ML, 3 ML, and 4 ML thick islands. Additionally, a specific edge effect which influences the $I(U)$ and $(dI/dU)/(I/U)$ spectra was observed. This edge effect can be neglected if the spectra were taken only from the central part of the islands.

The interaction of CoO(001)/Ag(001) with O₂ was studied. After annealing the sample in an O₂ atmosphere, a structural reordering of the islands was found. Characteristic shifts of the peaks in the $(dI/dU)/(I/U)$ spectra towards higher energies were measured for both CoO islands and Ag(001). These shifts were observed for both W and Pt-Ir tips and were attributed by O.

In addition, Co clusters were deposited onto CoO(001) films and studied by means of STM/STS. It was found that at RT Co mainly nucleates on uncovered Ag(001) areas and barely on the Co oxide islands. Depositing Co onto continuous and completely covering CoO(001) films, a large density of Co clusters is observed on the film terraces if the sample was cooled down to 77 K. This was different to RT deposition where step decoration occurs. The supported clusters showed an insulating behaviour as well as the tendency to form a band gap. However, the contribution of insulation support (CoO(001)) could not be clearly separated from those of the clusters.

Mn oxides on Ag(001)

First STM/STS investigations were performed on Mn film growth on Ag(001). The RT formation of a Mn-Ag surface alloy was analysed. A $c(2 \times 2)$ reconstruction was found in the LEED pattern for 1-2 ML thick Mn films on Ag(001). Surface alloying was also confirmed by STS since different peaks were found in the $(dI/dU)/(I/U)$ spectra for Mn islands, mixed Mn-Ag areas, and Ag(001). Chemically selective STM imaging based on the locally varying work function was applied. A pronounced contrast difference was found in the STM images taken at 4.5 V and 4.8 V. Thus, it was possible to conclude that Mn islands

are surrounded by a Ag fringe whereas the underlying substrate contains inter-mixed Mn-Ag areas. In addition, small Ag islands were found which probably appeared due to the exchange of Mn and Ag atoms in the initial growth stage.

Depositing Mn in an O₂ atmosphere, at least six different island types were found strongly depending on the preparation conditions (O₂ pressure, substrate temperature). The STS data revealed clear differences between all islands. Some similarities to the CoO(001) islands were recognised. However, in this beginning stage of investigations, no clear conclusions on the geometric and electronic structures of the Mn oxide islands could be derived.

Outlook

To extend the knowledge of the electronic structure of the CoO(001) films, it is necessary to perform a series of $z(U)$ experiments in order to study the FER formation in front of the CoO surface. This should help to separate the resonance effects from those caused by the DOS. An application of lock-in technique is also valuable for increasing the quality of the spectra.

As a further step in the STS study, a spin polarised (SP) STS is of great interest. Thus, using SP STM, the antiferromagnetic nature of the TMO layers can be investigated.

Abbreviations

AED	Auger Electron Diffraction
AES	Auger Electron Spectroscopy
AREELS	Angle-Resolved EELS
ARUPS	Angle-Resolved UPS
BIS	Bremsstrahlungisochromat Spectroscopy
DFT	Density Functional Theory
DOS	Density Of States
DRAM	Dynamic Random Access Memory
EELS	Electron Energy Loss Spectroscopy
et al.	et alii (and others)
etc.	etcetera (and so on)
e.g.	exempli gratia (for example)
i.e.	id est (that is, in other words)
IPE	Inverse Photoemission
ISS	Ion Scattering Spectroscopy
fcc	face centred cubic
L	Langmuir
LEED	Low Energy Electron Diffraction
LSDA	Local Spin Density Approximation
ML	Monolayer
MRAM	Magnetic Random Access Memory
SIC	Self-Interaction-Correlation
STM	Scanning Tunneling Microscopy
STS, $I/U/z$	Scanning Tunneling Spectroscopy Current/Voltage/distance
UPS	Ultraviolet Photoelectron/Photoemission Spectroscopy
UHV	Ultra High Vacuum
XPS	X-ray Photoelectron Spectroscopy
XRD	X-Ray Diffraction

Literature

- [1] P.A. Cox „*Transition metal oxides. An introduction to their electronic structure and properties*“
Oxford, Clarendon press (1995)
- [2] S. Yoshida, S. Sakaki, H. Kobayashi „*Electronic processes in catalysis. A quantum chemical approach to catalysis*“
Weinheim: VCH Verlagsgesellschaft (1994)
- [3] J.M. McKey, V.E. Henrich „*Surface electronic structure of NiO: Defect states, O₂ and H₂O interactions*“
Phys. Rev. B **32**, 6764-6772 (1985)
- [4] R.J. Lad, V.E. Henrich „*Surface electronic structure and chemisorption properties of MnO(100)*“
J. Vac. Sci. Technol. A **6**, 781-782 (1988)
- [5] S.-P. Jeng, Zh. Zhang, V.E. Henrich „*O₂ chemisorption on CoO(100): A resonant-photoemission study*“
Phys. Rev. B **44**, 3266-3271 (1991)
- [6] D. Cappus, C. Xu, D. Ehrlich, B. Dillman, C.A. Ventrice, J. Libuda, S. Wohlrab, F. Winkelmann, H. Kuhlenbeck, H.-J. Freund „*Electronic and geometric structure of adsorbates on oxide surfaces*“
J. Electron. Spectros. Relat. Phenom. **68**, 347-355 (1994)
- [7] J.L. Mackay, V.E. Henrich „*Electronic properties of CoO(100): defects and chemisorption*“
Phys. Rev. B **39**, 6156-6168 (1989)
- [8] H. Schwarz, D. Schröder „*Oxygenation of hydrocarbons by “bare” transition-metal oxides*“
38th on Chemical Research, Huston, U.S.A. 287-302 (1995)
- [9] S. Helfensteyn, H. Tollet, J. Degreve, C. Creemers „*LEIS-surface analysis of commercial sulphide oxide catalysts*“
Appl. Catalysis A: General **239**, 221-228 (2003)
- [10] M. Haruta „*Size- and support-dependency in the catalysis of gold*“
Catalysis Today **36**, 153-166 (1997)
- [11] H.-J. Freund, B. Dillman, D. Ehrlich, M. Hassel, R.M. Jaeger, H. Kuhlenbeck, C.A. Ventrice, F. Winkelmann, S. Wohlrab, C. Xu, T. Bertrams, A. Brodde, H. Neddermeyer „*Adsorption and reaction of molecules on surfaces of metal-metal oxide system*“
J. Molecular Catalysis **82**, 143-169 (1993)
- [12] P.J.M. van Bentum, R.T.M. Smokers, H. van Kempen „*Incremental charging of single small particle*“

- Phys. Rev. Lett. **60**, 2543-2546 (1998)
- [13] M.E. Lin, R.P. Andres, R. Reifenberger „*Observation of the discrete electron energy states of an individual nanometer-size supported gold clusters*“
Phys. Rev. Lett. **67**, 477-480 (1991)
- [14] J. Nogues, I.K. Schuller „*Exchange bias*“
J. Magn. Magn. Matter **192**, 203-232 (1999)
- [15] K.-H. Meiwes-Broer „*Metal clusters at surfaces. Structure, quantum properties, physical chemistry*“
Springer-Verlag Berlin Heidelberg (2000)
- [16] M.N. Baibich, J.M. Broto, A. Fert, F. Nguen Van Dau, F. Petroff, P. Eitenne, G. Creuzet, A. Friedrich, J. Chazelas „*Giant magnetoresistance of (001)Fe/(001)Cr magnetic superlattices*“
Phys. Rev. Lett. **61**, 2472-2475 (1988)
- [17] B. Doudin, G. Redmond, S.E. Gilbert, J.-Ph. Ansermet „*Magnetoresistance governed by fluctuations in ultrasmall Ni/NiO/Co junctions*“
Phys. Rev. Lett. **74**, 933-936 (1995)
- [18] J.S. Moodera, L.R. Kinder, T.W. Wong, R. Meservey „*Large magnetoresistance at room temperature in ferromagnetic thin film junctions*“
Phys. Rev. Lett. **74**, 3273-3276 (1995)
- [19] C.L. Platt, B. Deny, A.E. Berkowitz „*Spin polarized tunneling in reactively sputtered tunnel junctions*“
J. Appl. Phys. **81**, 5523-5525 (1997)
- [20] M. Bowen, M. Bibes, A. Barthelemy, J.P. Contour, A. Anane, Y. Lemaitre, A. Fert „*Nearly total spin polarization in $La_{2/3}Sr_{1/3}MnO_3$ from tunneling experiments*“
J. Appl. Phys. **81**, 5523-5525 (1997)
- [21] R. Gunnarsson, Z.G. Ivanov, Doubordiev, H. Roussel „*Low field magnetoresistance in perovskite manganites: magnetic field, temperature and current dependence*“
Phys. Rev. B **69**, 0544131-0544136 (2004)
- [22] I. Sebastian „*Rastertunnelmikroskopie zur Keimbildung and zum Wachstum dünner CoO-Schichten auf Ag(100) and Au(111)*“
PhD thesis, Martin-Luther-Universität Halle-Wittengerg(2000)
- [23] F. Müller, R. de Masi, P. Steiner, D. Reinicke, M. Stadtfeld, S. Hüfner „*EELS investigation of thin epitaxial NiO-Ag(001) films: surface states in the multilayer, monolayer and submonolayer range*“
Surf. Sci. **459**, 161-172 (2000)

- [24] M.R. Castel, S.L. Dudarev, G.A.D. Briggs, A.P. Sutton „*Unexpected differences in the surface electronic structure of NiO and CoO observed by STM and explained by first principle theory*“
Phys. Rev. B. **59**, 7859-7863 (1997)
- [25] K. Marre, H. Neddermeyer „*Growth of ordered thin films of NiO on Ag(100) and Au(111)*“
Surf. Sci. **287-288**, 995-999 (1993)
- [26] I. Sebastian, Th. Bertrams, K. Meinel, H. Neddermeyer „*Scanning tunneling microscopy on growth and structure of NiO(100) and CoO(100) thin films*“
Faraday Discuss. **114**, 129-140 (1999)
- [27] Ch. Hagendorf, R. Shantyr, K. Meinel, K.-M. Schindler, H. Neddermeyer „*Scanning tunneling microscopy investigation of the atomic and electronic structure of CoO(100) islands on Ag(001)*“
Surf. Sci. **532-535**, 346-350 (2003)
- [28] R. Shantyr, Ch. Hagendorf, H. Neddermeyer „*Scanning tunneling microscopy and spectroscopy of CoO precursor and oxide layers on Ag(001)*“
Surf. Sci. in press (2004)
- [29] R. Shantyr, Ch. Hagendorf, H. Neddermeyer „*Electronic properties of thin films of Co oxides and oxide precursor states on Ag(001) using scanning tunneling microscopy and spectroscopy*“
Solid State Films (submitted) (2004)
- [30] F. Müller, R. de Masi, D. Reinicke, P. Steiner, S. Hufner, K. Söwe „*Epitaxial growth of MnO/Ag(001)*“
Surf. Sci. **520**, 158-172 (2002)
- [31] I. Sebastian, H. Neddermeyer „*Scanning tunneling microscopy on the atomic and electronic structure of CoO thin films on Ag(001)*“
Surf. Sci. **454-456**, 771-777 (2000)
- [32] H.N. Ok, J. G. Mullen „*Evidence of two forms of cobaltus oxide*“
Phys. Rev. **168**, 550-562 (1968)
- [33] H. Landoldt, R. Börnstein „*Numerical data and functional relationships in science and technology*“
New serie: group IV, vol. 5, subvol. C, 333 Berlin, Springer (1997)
- [34] Ch. Kittel „*Einführung in die Festkörperphysik*“
München, Oldenburg (1993)
- [35] C.R. Brundle, T.J. Chuang, D.W. Rice „*X-ray photoemission study of the interaction of oxygen and air with clean cobalt surface*“
Surf. Sci. **60**, 286-300 (1976)
- [36] D. Wolf „*Reconstruction of NaCl surface from a dipolar solution to the Madelung problem*“

- Phys. Rev. Lett. **68**, 3315-3318 (1992)
- [37] C. Mocuta, A. Barbier, G. Renaud „*CoO(111) surface study by surface X-ray diffraction*“
Surf. Sci. **433-435**, 761-764 (1999)
- [38] A. Barbier, G. Renaud, C. Mocuta, A. Stierle „*Structural investigation of the dynamics of the NiO(111) surface by GIXS*“
Appl. Surf. Sci. **162-163**, 56-61 (2000)
- [39] C.A. Ventrice, Th. Bertrams, H. Hannemann, A. Brodde, H. Neddermeyer „*Stable reconstruction of the polar (111) surface of NiO on Au(111)*“
Phys. Rev. Lett. **49**, 5773-5776 (1994)
- [40] H. Landoldt, R. Börnstein „*Numerical data and functional relationships in science and technology*“
New serie: group IV, vol. 5, subvol. H, 127 Berlin, Springer (1997)
- [41] K. Terakura, A.R. Williams, T. Oguchi, J. Kubler „*Transition metal monoxides: Band or Mott insulators*“
Phys. Rev. Lett. **52**, 1830-1833 (1984)
- [42] J. van Elp, J.L. Wieland, H. Eskes, P. Kuiper, G. A. Sawatzky, F.M.F. de Groot, T.S. Turner „*Electronic structure of CoO, Li-doped CoO, and LiCoO₂*“
Phys. Rev. B **44**, 6090-6103 (1991)
- [43] Z.X. Shen, J.W. Allen, P.A.P. Lindberg, P. Dessau, B.O. Wells, A. Borg, W. Ellis, J.S. Kang, S.J. Oh, I. Lindau, W.E. Spicer „*Photoemission study of CoO*“
Phys. Rev. Lett. **42**, 1817-1828 (1990)
- [44] J. Zaanen, G.A. Sawatzky, J.W. Allen „*Band gaps and electronic structure of transition metal compounds*“
Phys. Rev. Lett. **55**, 418-421 (1985)
- [45] D. Ködderitzsch. „*Elektronische Struktur von Übergangsmetalloxidoberflächen.*“
Diplomawork, Martin-Luther-University Halle-Wittenberg (1999)
- [46] Z. Szotek, W.M. Temmerman „*Application of self-interaction to transition metal oxides*“
Phys. Rev. B **47**, 4029-4032 (1993)
- [47] V.I. Anisimov, F. Aryasetiawan, A.I. Lichtenstein „*First-principles calculations of the electronic structure and spectra of strongly correlated systems: the LDA+U method*“
J. Phys.: Condens. Matter **9**, 767-808 (1997)
- [48] M. Heiler, A. Chassé, K.-M. Schindler, M. Hollering, H. Neddermeyer „*Electronic and geometric structure of thin CoO(100) films studied by angle-resolved photoemission spectroscopy and Auger electron diffraction*“
Surf. Sci. **454-456**, 36-40 (2000)

-
- [49] A. Gorschlüter, H. Merz „*Localized d-d excitations in NiO(100) and CoO(100)*“
Phys. Rev. B **49**, 17293-17302 (1994)
- [50] J.E. Pask, D.J. Singh, I.I. Mazin, C.S. Hellberg „*Structural, electronic, and magnetic properties of MnO*“
Phys. Rev. B **64**, 0244031-0244037 (2001)
- [51] Z. Fang, I.V. Solovyev, H. Sawada „*First-principle study on electronic structures and phase stability of MnO and FeO under high pressure*“
Phys. Rev. B **59**, 762-774 (1999)
- [52] J. van Elp, R.H. Potze, H. Eskes, R. Berger, G.A. Sawatzky „*Electronic structure of MnO*“
Phys. Rev. B **44**, 1530-1537 (1991)
- [53] A. Fujimori, F. Minami, K. Siratori, M. Taniguchi, S. Ogawa, S. Suga „*Electronic structure of MnO*“
Phys. Rev. B **42**, 7580-7586 (1990)
- [54] G. Binnig, H. Rohrer, Ch. Gerber, E. Weibel „*Surface Studies by Scanning Tunneling Microscopy*“
Phys. Rev. Lett. **49**, 57-61 (1982)
- [55] G. Doyen, D. Drakova, M. Scheffler „*Green-function theory of scanning tunneling microscopy: tunnel current and current density of clean metal surfaces*“
Phys. Rev. B. **47**, 9778-9790 (1993)
- [56] J. Bardeen „*Tunneling from a many-particle point of view*“
Phys. Rev. Lett. **6**, 57-59 (1961)
- [57] J. Tersoff, D.R. Hamann „*Theory of the scanning tunneling microscope*“
Phys. Rev. B **31**, 805-813 (1985)
- [58] R.M. Feenstra, J.A. Stroscio, A.P. Fein „*Tunneling spectroscopy of the Si(111)2×1 surface*“
Surf. Sci. **181**, 295-306 (1987)
- [59] N.D. Lang „*Spectroscopy of single atoms in scanning tunneling microscope*“
Phys. Rev. B **34**, 5947-5950 (1986)
- [60] J. Viernow, D.Y. Petrovykh, A. Kirakosian, J.-L. Lin, F.K. Men, M. Henzler, F.I. Himpel „*Chemical imaging of insulators by STM*“
Phys. Rev. B **59**, 10356-10361 (1999)
- [61] R. Shuster, J.V. Barth, J. Winterlin, R.J. Behm, G. Ertl „*Distance dependence and corrugation in barrier-height measurements on metal surface*“
Ultramicroscopy **42-44**, 533-540 (1992)

- [62] L. Olesen, M. Brandbyge, M.R. Sorensen, K.W. Jacobsen, E. Laegaard, I. Stensgaard, F. Besenbacher „*Apparent barrier height in scanning tunneling microscopy revisited*“
Phys.Rev. Lett. **76**, 1485-1488 (1996)
- [63] K.H. Gundlach „*Zur Berechnung des Tunnelstroms durch eine trapezförmige Potentialstufe*“
Solid State Electronics **9**, 949-957 (1966)
- [64] J.H. Coombs, J.K. Gimzewski „*Fine structure in field emission resonances at surface*“
Journal of Microscopy **152**, 841-851 (1988)
- [65] N. Garcia „*Theory of scanning tunneling microscopy and spectroscopy: resolution, image and field states, and thin oxide layers*“
IBM J. Res. Develop. **30**, 533-542 (1986)
- [66] K. Bobrow, A. J. Mayne, G. Dujardin „*Atomic-scale imaging of insulating diamond through resonant electron injection*“
Letters to Nature **413**, 616-619 (2001)
- [67] R. Garcia, J.J. Saenz, J.M. Moler, N. Garcia „*Distance-voltage characteristics in scanning tunneling microscopy*“
J. Phys. C **19**, L131-L134 (1986)
- [68] M. Mitte „*Rastertunnelmikroskopie zum Wachstum und zur Struktur dünner Cu-Schichten auf Ru(0001) im Temperaturbereich von 100 K bis Raumtemperatur*“
PhD thesis, Martin-Luther-Universität Halle-Wittenberg (2001)
- [69] Ch. Hagendorf. Privat communication
- [70] A. Kraus. Privat communication
- [71] A. Goldmann, V. Dose, G. Borstel „*Empty electronic states at the (100), (110), and (111) surfaces of nickel, copper, and silver*“
Phys. Rev. B **32**, 1971-1980 (1985)
- [72] F.J. Himpsel, J.E. Ortega „*Electronic structure of Cu(100), Ag(100), Au(100), and Cu₃Au(100) from inverse photoemission*“
Phys. Rev. B **46**, 9719-9723 (1992)
- [73] U. König, P. Weinberger, J. Redinger, H. Erschbaumer, A.J. Freeman „*Angle-resolved photoemission and inverse photoemission from Ag(100)*“
Phys. Rev. B **39**, 7492-7499 (1989)
- [74] Y. Suganuma, M. Tomitori „*Evaluation of an electric field over the sample surfaces by electron standing wave in a vacuum gap of scanning tunneling microscopy*“
Jpn. J. Appl. Phys. **39**, 3758-3760 (2000)

- [75] Y. Sugauma, M. Tomitori „*Tunneling condition dependence of electron standing waves in vacuum gaps on Au(111) and Si(001) observed by scanning tunneling microscopy*“
Surf. Sci. **438**, 311-318 (1999)
- [76] R.S. Becker, J.A. Golovchenko, D.R. Hamann, B.S. Swartyentruber „*Real-space observation of surface states on Si(111) 7×7 with the tunneling microscope*“
Phys. Rev. Lett. **55**, 2032-2034 (1985)
- [77] J.A Kubby, Y.R. Wang, W.J. Greene „*Imaging defect formation in the template growth of NiSi₂/Si(111): an application of quantum size microscopy*“
Phys. Rev. B **48**, 4473-4480 (1993)
- [78] J.A Kubby, Y.R. Wang, W.J. Greene „*Electron interferometry at heterojunction interface*“
Phys. Rev. Lett. **65**, 2165-2168 (1990)
- [79] J.W. Gadzuk „*Single-atom point source for electrons: Field-emission resonance tunneling in scanning tunneling microscopy*“
Phys. Rev. B **47**, 12832-12839 (1993)
- [80] L. Scandella, H.-J. Güntherodt „*Field emission resonances studied with $dI/ds(V)$ and $dI/dV(V)$ curves*“
Ultramicroscopy **42-44**, 546-552 (1992)
- [81] M. Nagai, M. Tomitori, O. Nishikawa „*Sharpening processes of scanning tunneling microscopy / scanning tunneling spectroscopy tips by thermal field treatment*“
Jpm. J. Appl. Phys. Part 1 **36**, 3844-3849 (1997)
- [82] J.M. Pitarke, F. Flores, P.M. Echenique „*Tunneling spectroscopy: surface geometry and interface potential effects*“
Surf. Sci. **234**, 1-16 (1990)
- [83] Y. Sugauma, M. Tomitori „*Analysis of electron standing waves in a vacuum gap of scanning tunneling microscopy: Measurement of band bending through energy shifts of electron standing wave*“
J. Vac. Sci. Technol. B **39**(1), 48-54 (2000)
- [84] J.A Kubby, Y.R. Wang, W.J. Greene „*Fabry-Pérot transmission tunneling microscopy*“
Phys. Rev. B **43**, 9346-9349 (1991)
- [85] M. Hansmann „*Elektronische Struktur niederdimensionaler Systeme an Oberflächen*“
PhD thesis, Freie Universität Berlin (2003)
- [86] O.Yu. Kolesnychenko, Yu.A. Kolesnychenko, O.I. Shklyarevskii, H. van Kempen „*Field-emission resonance measurements with mechanically controlled break junction*“

- Physica B **291**, 246-255 (2000)
- [87] G. Binnig, H. Rohrer, Ch. Gerber, E. Weibel „*Tunneling through a controllable vacuum gap*“
Appl. Phys. Lett. **40**, 178-180 (1982)
- [88] U.Dürig, O. Züger, D.W. Pohl „*Observation of metallic adhesion using the scanning tunneling microscopy*“
Phys.Rev. Lett. **65**, 349-352 (1990)
- [89] G. Seine, R. Coratger, A. Carladous, A. Ajustron, R. Pchou, J. Beauvillain „*Imaging using tip-surface distance variation vs. voltage in scanning tunneling microscopy*“
Surf. Sci. **465**, 219-226 (2000)
- [90] L. Olesen, E. Laægaard, I. Stensgaard, F. Besenbacher „*Comparative study of methods for measuring the apparent barrier height on an atomic scale*“
Appl. Phys. A **66**, S152-S160 (1998)
- [91] Tien T. Tsong „*Effect of an electric field in an atomic manipulations*“
Phys. Rev. B **44**, 13703-13710 (1991)
- [92] J.K Gimzewski, R. Möller „*Transition from the tunneling regime to point contact studied using scanning tunneling microscopy*“
Phys. Rev. B **44**, 1284-1287 (1987)
- [93] A. Kraus „*Präparation und Charakterisierung von Nanostrukturen mittels Rastertunnelmikroskopie auf Si(111)*“
PhD these, Martin-Luther-Universität Halle-Wittenberg (2002)
- [94] D. Sarid „*Exploring scanning probe microscopy with Mathematica*“
John Wiley & Sons, Inc., New York (1997)
- [95] S. Ciraci „*Atomic-scale tip-sample interactions and contact phenomena*“
Ultramicroscopy **42-44**, 16-21 (1992)
- [96] B. Degroote, J. Dekoster, G. Langouche „*Step decoration and surface alloying: growth of cobalt on Ag(100) as a function of deposition temperature*“
Surf. Sci. **452**, 172-178 (2000)
- [97] S. Schnitke, S. Messereli, K. Morgenstern, J. Nieminen, W.-D. Schneider „*Far-ranged transient motion of “hot” oxygen atoms upon dissociation*“
Jour. Chem. Phys. **114**, 4206-4209 (2001)
- [98] M. Rocca, L. Savio, L. Vattuone, U. Burghaus, V. Palomba, N. Noveli, F. Bautier de Mangeot, U. Valbusa, R. Gunella, G. Comelli, A. Baraldi, S. Lizzit, G. Paolucci „*Phase transition of dissociatively adsorbed oxygen on Ag(001)*“
Phys. Rev. B **61**, 213-227 (2000)
- [99] J.P. Crocombette, H. de Monestrol, F. Willaime „*Oxygen and vacancies in silver: A density-functional study in the local density and generalized gradient approximation*“

- Phys. Rev. B **66**, 0241141-0241145 (2002)
- [100] M. Rocca, L. Vattuone, L. Savio, F. Bautier de Mangeot, U. Valbusa, G. Comelli, S. Lizzit, A. Baraldi, G. Paolucci, J.A. Groeneveld, E.J. Baerdence „*Transient CO adsorption and the catalytic properties of surfaces*“
Phys. Rev. B **63**, 0814041-0814044 (2001)
- [101] C. Backx, C.P.M. De Groot, P. Biloen, W.M.H. Sachtler „*Interaction of O₂, CO₂, CO, C₂H₄ and C₂H₄O with Ag(110)*“
Surf. Sci. **128**, 81-103 (1983)
- [102] S. Messerli, S. Schnitke, K. Morgenstern, J. Nieminen, W.-D. Schneider „*Oxygen molecules on Ag(001): superstructure, binding site and molecular orientation*“
Chem. Phys. Lett. **328**, 330-336 (2000)
- [103] E.L. Garfunkel, X. Ding, G. Dong, S. Yang, X. Hou, X. Wang „*The coadsorption of sodium and oxygen on Ag(100): an XPS, UPS and HREELS study*“
Surf. Sci. **164**, 511-525 (1985)
- [104] F. Buatier de Mongeot, M. Rocca and U. Valbusa „*Energy and angle dependence of the initial sticking coefficient of O₂ on Ag(001)*“
Surf. Sci. **363**, 68-72 (1996)
- [105] T. Zambelli, J. V. Barth, J. Wintterlin „*Thermal dissociation of chemisorbed oxygen molecules on Ag(110): an investigation by scanning tunneling microscopy*“
J. Phys.: Condens. Matter **14**, 4241-4250 (2002)
- [106] K. Meinel, H. Wolter, Ch. Ammer, H. Neddermeyer „*Metastable misfit-induced relaxation structures of close-packed heteroepitaxial films*“
Surf. Sci. **401**, 434-444 (1998)
- [107] D. Kolb „*An atomistic view of electrochemistry*“
Surf. Sci. **500**, 722-740 (2002)
- [108] L. Savio, L. Vattuone, M. Rocca „*Effect of surface interband transitions on surface plasmon dispersion: O/Ag(001)*“
Phys. Rev. B **61**, 7324-7327 (2000)
- [109] Th. Bertrams, H. Neddermeyer „*Growth of NiO(100) on Ag(100): Characterization by scanning tunneling microscopy*“
J. Vac. Sci. Technol. B **14**(2), 1141-1144 (1996)
- [110] M. A. Langell, M. D. Anderson, G. A. Carson, L. Peng, S. Smith „*Valence-band electronic structure of Co₃O₄ epitaxy on CoO(100)*“
Phys. Rev. B **59**, 4791-4798 (1999)
- [111] F.C. Voogt, T. Fujii, P.J.M. Smulders, L. Niesen, M.A. James, T. Hibma „*NO₂-assisted molecular beam epitaxy of Fe₃O₄, Fe_{3-δ}O₄, and γ-Fe₂O₃ thin films on MgO(100)*“
Phys. Rev. B **60**, 11193-11206 (1999)

- [112] J.F. Anderson, M. Kuhn, U. Diebold, K. Shaw, P. Stoyanov, D. Lind „*Surface structure and morphology of Mg-segregated epitaxial Fe₃O₄(001) thin films on MgO(001)*“
Phys. Rev. B **56**, 9902-9909 (1997)
- [113] O.N. Chung, S. Chung „*Scanning tunneling microscopy and spectroscopy studies of the oxide nanofilms of the stainless steel surface*“
J. Vac. Sci. Technol. B **21**(4), 1297-1300 (2003)
- [114] S. A. Chambers „*Epitaxial growth and properties of thin film oxides*“
Surf. Sci. Reports **39**, 105-180 (2000)
- [115] M.C. Gallagher, M.S. Fyfield, L.A. Bumm, J.P. Cowin, S.A. Joyce „*Structure of ultrathin MgO films on Mo(001)*“
Thin Solid Films **445**(1), 90-95 (2003)
- [116] S. Valeri, S. Alteri, U. del Pennino, A. di Bona, P. Luches, A. Rota „*Scanning tunneling microscopy of MgO ultrathin films on Ag(001)*“
Phys. Rev. B **65**, 2454101-2454105 (2002)
- [117] M. Heiler, A. Chassé, K.-M. Schindler, M. Hollering, H. Neddermeyer „*Electronic and geometric structure of thin CoO(100) films studied by angle-resolved photoemission spectroscopy and Auger electron diffraction*“
Surf. Sci. **454-456**, 36-40 (2000)
- [118] Z.-X. Shen, J.W. Allen, W. Ellis, J.S. Kang, S.-J. Oh, I. Lindau, W.E. Spicer „*Photoemission study of CoO*“
Phys. Rev. B **42**, 1817-1828 (1990)
- [119] Z.-X. Shen, C.K. Shih, O. Jepsen, W.E. Spicer, Lindau, J.W. Allen „*Aspects of the correlation effects, Antiferromagnetic order and translational symmetry of the electronic structure of NiO and CoO*“
Phys. Rev. Lett. **64**, 2442-2445 (1990)
- [120] M. Takanashi, J. Igarashi „*Local approach to electronic excitation in MnO, FeO, CoO, and NiO*“
Phys. Rev. B **54**, 13566-13574 (1996)
- [121] S. Hüfner and T. Tiesterer „*Electronic structure of NiO*“
Phys. Rev. B **33**, 7267-7269 (1986)
- [122] Ch. Dietrich, H.G. Boyen, B. Koslowski „*Characterisation of ultrathin insulating Al₂O₃ films grown on Nb(110)/sapphire (0001) by tunneling spectroscopy and microscopy*“
J. Appl. Phys. **94**, 1478-1484 (2003)
- [123] S. Schnittke, S. Messerli, M. Pivetta, F. Patthey, L. Liboulle, M. Stengel, A. De Vita, W.-D. Schneider „*Insulator at the ultrathin limit: MgO on Ag(001)*“
Phys. Rev. Lett. **87**, 2768011-2768014 (2001)

- [124] R.M. Feenstra „*Tunneling spectroscopy of the (110) surface of the direct-gap III-V semiconductors*“
Phys. Rev. B **50**, 4561-4570 (1994)
- [125] S. Alteri, L.H. Tjeng, G.A. Sawazky „*Electronic structure and chemical reactivity of oxide-metal interfaces: MgO(100)/Ag(100)*“
Phys. Rev. B **61**, 16948-16955 (2000)
- [126] A.E. Hanna, M. Tinkham „*Variation of the Coulomb staircase in a two-junction system by fractional electron charge*“
Phys. Rev. B **44**, 5919-5922 (1991)
- [127] M. Amman, R. Wilkins, E. Ben-Jacob, P. D. Maker, R.C. Jaklevic „*Analytic solution for the current-voltage characteristic of two mesoscopic tunnel junctions coupled in series*“
Phys. Rev. B **43**, 1146-1149 (1991)
- [128] R. Wilkins, E. Ben-Jacob, R.C. Jaklevic „*Scanning tunneling observations of Coulombs blockade and oxide polarisation in small metal droplets*“
Phys. Rev. Lett. **63**, 801-804 (1989)
- [129] H.G. Boyen, G. Kastle, F. Weigl, B. Koslowski, C. Dietrich, P. Ziemann, J.P. Spatz, C. Hartman, M. Moller, G. Schmidt, M. G. Garnier, P. Oelhafen „*Oxidation-resistant gold-55 clusters*“
Science **297**, 1533-1536 (2002)
- [130] V. Podgursky, I. Costina, R. Franchy „*Co on thin Al₂O₃ films grown on Ni₃Al (100)*“
Surf. Sci. **529(3)**, 419-427 (2003)
- [131] K. H. Hansen, T. Worren, S. Stempel, E. Laegsgaard, M. Bäumer, H.-J. Freund, F. Besenbacher, I. Stensgaard „*Palladium nanocrystals on Al₂O₃: structure and adhesion energy*“
Phys. Rev. Lett. **83**, 4120-4123 (2000)
- [132] C. Xu, X. Lai, G.W. Zajac, D.W. Goodman „*Scanning tunneling microscopy studies of the TiO₂(110) surface: structure and nucleation growth of Pd*“
Phys. Rev. B **56**, 13464-13482 (1997)
- [133] M. Valden, X. Lai, D.W. Goodman „*Onset of catalytic activity of gold clusters on titania with the appearance of nonmetallic properties*“
Science **281**, 1647-1650 (1998)
- [134] A. Bettac, L. Köller, V. Rank, K.H. Meiwes-Broer „*Scanning tunneling spectroscopy on deposited platinum clusters*“
Surf. Sci. **402-404**, 475-479 (1998)
- [135] H. Hövel, B. Grimm, M. Bödecker, K. Fieger, B. Reihl „*Tunneling spectroscopy on silver clusters at T=5 K: size dependence and spatial energy shifts*“
Surf. Sci. **463**, L603-L608 (2000)

- [136] H. Hövel „*Cluster on surface: high-resolution spectroscopy at low temperatures*“
Appl. Phys. A **72**, 295-302 (2001)
- [137] X. Chen, J. Zhao, G. Wang „*Conductance resonance of metal-insulator-metal junction with embedded metal cluster*“
Appl. Phys. Lett. **65**(19), 2419-2421 (1994)
- [138] M. Bäumer, J. Libuda, A. Sandell, H.-J. Freund, G. Graw, Th. Bertrams, H. Neddermeyer „*The growth and properties of Pd and Pt on Al₂O₃/NiAl(110)*“
Phys. Chem. **99**, 1381-1386 (1995)
- [139] B.T. Jonker, J.J. Krebs, G.A. Prinz „*Growth and magnetic characterisation of Mn films and superlattices on Ag(001)*“
Phys. Rev. B **39**, 1399-1402 (1989)
- [140] W. Kim, S.-J. Oh, J. Seo, J.-S. Kim, H.-G. Min, S.-C. Hong „*Formation of bilayer ordered surface alloy Mn/Ag(001)*“
Phys. Rev. B **57**, 8823-8826 (1998)
- [141] P. Schieffer, C. Krembel, M.C. Hanf, G. Gewinner „*Room-temperature instability of the Mn/Ag(100) interface in the monolayer range*“
Phys. Rev. B **55**, 13884-13893 (1997)
- [142] P. Schieffer, C. Krembel, M.C. Hanf, G. Gewinner „*Room-temperature instability of the Mn/Ag(100) interface in the monolayer range*“
Phys. Rev. B **55**, 13884-13893 (1997)
- [143] P. Schieffer, M.-H. Tuilier, C. Krembel, M.C. Hanf, G. Gewinner, D. Chandris, H. Magnan „*Atomic structure of the surface alloy formed by a room-temperature-deposited Mn monolayer on Ag(001)*“
Phys. Rev. B **57**, 15507-15512 (1998)
- [144] P. Schieffer, C. Krembel, M.C. Hanf, G. Gewinner „*Atomic structure of the Ag(001) c(2x2) Mn surface alloy*“
Phys. Rev. B **65**, 2354271-2354276 (2002)
- [145] M.M.J. Bischoff, T. Yamada, A.J. Quinn, H. van Kempen „*Scanning tunneling microscopy and spectroscopy study on the submonolayer growth of Mn on Fe(001)*“
Surf. Sci. **501**, 155-167 (2002)
- [146] T. Yamada, M.M.J. Bischoff, T. Mizoguchi, H. van Kempen „*STM and STS study of ultrathin Mn layers on Fe(001)*“
Surf. Sci. **516**, 179-190 (2002)
- [147] T. Jungm Y.W. Mo, F.J. Himpsel „*Identification of metals in scanning tunneling microscopy via image states*“
Phys. Rev. Lett. **74**, 1641-1644 (1995)
- [148] M.A. Langell, N.R. Cameron „*Thermally induced surface reconstruction of MnO(100)*“

Surf. Sci. **185**, 105-119 (1987)

Danksagung

An dieser Stelle möchte ich allen Danken, die zum Gelingen dieser Arbeit beigetragen haben:

Herrn Prof. Dr. H. Neddermeyer für die Überlassung der äußerst interessanten Thematik sowie für die Unterstützung bei der Bearbeitung derselben;

Herrn Prof. Dr. W. Widdra für die fruchtbare Fragestellungen und freundliche Unterstützung, insbesondere in der Abschlußphase der Arbeit;

Herrn Dr. K. Meinel für die Mühe bei der Durchsicht des Manuskripts sowie für zahlreiche wertvolle Hinweise und Diskussionen;

Herrn R. Kulla für die gute Zusammenarbeit bei der Entwicklung neuer Komponenten für STM sowie die Hilfe bei der Lösung der technischen Probleme beim Umbau des STM;

Herrn T. Doege für seine Hinweise, die Technische unterstützung und anregende Diskussionen;

Herrn H. Benkwitz und Herrn L. Büttner sowie allen anderen Mitarbeitern der mechanischen Werkstatt für die produktive Zusammenarbeit bei der Verbesserung alter und der Entwicklung neuer Komponenten;

Herrn D. Schmetzdorf und Herrn A. Müller für die Reparatur und Wartung ältere und die Entwicklung neuer elektonischen Komponenten;

Herrn H. Mehl für die Unterstützung bei rasterelektronmikroskopischen Untersuchungen;

der gesamten Arbeitsgruppe Oberflächen und Grenzflächenphysik, die einen nicht zu unterschätzenden Faktor beim Erfolg experimenteller Arbeit darstellt, für die Hilfsbereitschaft und angenehme Atmosphäre;

der Deutschen Forschungsgemeinschaft für die Finanzierung des Projektes.

Für die Hilfsbereitschaft, viele Anregungen und zahlreiche Diskussionen sowie viel Geduld in der Anfangsphase der Arbeit bin ich Dr. Ch. Hagendorf zu großem Dank verpflichtet.

Ganz besonders danke ich meiner Frau Oksana, meinen Eltern und meiner Schwester für ihre Geduld, Aufmunterungen und Unterstützung in allen Phasen dieser Arbeit.

Lebenslauf

Name: Roman Shantyr
Geburtsdatum: 07.02.1978
Geburtsort: Sumy, Ukraine
Familienstand: verheiratet

1985–95 Schule in Sumy
1995 Beginn des Physik-Studiums an der Staatlichen Universität Sumy
1999 Abschluß des Physik-Studiums als Bachelor of Science
2000 Abschluß des Physik-Studiums als Master of Science
2000-01 wissenschaftlicher Mitarbeiter am Sumy Institute for Surface Modification
(Prof. Dr. A. Pogrebnjak)
seit 2001 wissenschaftlicher Mitarbeiter am Fachbereich Physik der Martin-Luther-
Universität Halle–Wittenberg in der Arbeitsgruppe Oberflächen- und
Grenzflächenphysik (Prof. Dr. H. Neddermeyer/Prof. Dr. W. Widdra)

Halle (Saale), 06.04.2004

Erklärung

Hiermit erkläre ich, dass ich gemäß dem § 5, Absatz 2b der Promotionsordnung der Mathematisch-Naturwissenschaftlich-Technischen Fakultät der Martin-Luther-Universität Halle-Wittenberg vom 8.4.1197, die vorliegende Arbeit selbstständig und ohne fremde Hilfe verfaßt, andere als die von mir angegebenen Quellen und Hilfsmittel nicht benutzt und die den benutzten Werken wörtlich oder inhaltlich entnommenen Stellen als solche kenntlich gemacht habe.

Halle (Saale), 06.04.2004

Roman Shantyr